Design and Implementation of DSP-Based Magnetic Control System for Capsule Endoscope

Ibrahim Al-Lehaby

Newcastle University

Newcastle upon Tyne, UK.

A thesis submitted for the degree of

Doctor of Philosophy

September 2012

Declaration

I declare that this thesis is my own work and it has not been previously submitted, either by me or by anyone else, for a degree or diploma at any educational institute, school or university. To the best of my knowledge, this thesis does not contain any previously published work, except where another person's work used has been cited and included in the list of references.

Ibrahim Khalaf Mohammed Al-Lehaby

I dedicate this thesis to my precious wife, Shemma, and children, Abdalmalek, Othman and Rahaf, who have supported me throughout the years of my study and efforted my stress during implementation of the Phd project. To my loving mother and soul of my dear father who died in the third year of my study, to loving brother Ramadan, Mohammed, Ahmed, Mahmoud, and to soul of my loving brother Jasim, to my loving sisters Maryym, fatemh, eman, amel, basimh, Manal, and soul of my sister Munna, to my nice Mahdy, to the families of my brothers and sisters, to my cousin, to my secondary and underguraduate study friends, to Electronics Engineering college/ Mosul University. Finally, to Iraq from Zako to Basra.

With all my love

Acknowledgements

The journey which took four years to complete this research project was marvellous. It would be selfish not to acknowledge the people who have helped me in numerous ways. First of all my supervisor Dr. Bayan Sharif who accepted me as his PhD student. Without his constant encouragement, I would not have been able to complete this project. I would like to thank my second supervisor, Mr. Jeffrey Neasham, for sharing his great knowledge about practical implementation of the projects beside his gone through the pain of answering many of my stupid questions!. I thank him also for being helpful during writing the thesis. I would like to thank my third supervisor Dr. D. Giaouris who supervised me during the second year of my study.

I would also like to thank my friends Sabah, Ahmed, Tahani, Adbalrahman, Mohammed, Salah, Sedki, Mahar, Saad, Hussien, Muayad, Ammar, Emad, Singar, Waleed, Monar, Alaa, Omar Buzaid, Dr. Rajish, Nike, and Ebukun. Their friendship and company made life enjoyable at the university. I will always miss this part of my life. I also thank school's reception staff and electrical and mechaniocal workshop staff, Mr. Jack, Alin, Stuart, Chris, Jeffrey, Graham for thier help during period of my project implementation.

I would like to thank my parents, who have supported me throughout my life. I thank them from the bottom of my heart for proving me with the best up-bringing. Every time I born, I want to be their son. I thank the God, for all the positive things that have happened to me in my life.

Lastly, I would like to express my sincere gratitude to my sponsor the Ministry of Higher Education in Iraq who have given me the opportunity of an education at the best universities in the UK.

Abstract

Early detection methods are key to reducing morbidity rates from digestive tract cancer which is currently one of the fastest growing cancers in the World. Capsule endoscopes (CEs) are a new technology that can be used to improve early detection of the gastrointestinal (GI) tract disorder. The device integrates the technologies such as image processing, optoelectronic engineering, information communication, and biomedical engineering. The capsule is the size and shape of a pill and contains an optoelectronic camera, antenna, transmitter, battery and optoelectronic illuminating light emitting diodes (LEDs).

The small size of these devices enables them to offer many advantages over conventional endoscopes such as accessibility to the entire intestine and minimising the risk of perforation, particularly for patients with difficult anatomy (e.g. post-operative scar tissue). Currently used devices are passive and can only follow the natural transit of the intestines, and hence there is considerable interest in methods of controlled actuation for these devices.

In this thesis, a novel actuation system based on magnetic levitation is designed, developed and implemented, utilizing a small permanent magnet embedded within the capsule and an arrangement of digitally controlled electromagnets outside the body. The proposed approach is that the magnet can be moved and oriented by DC magnetic force and torque produced by coils placed outside of the human body, with a suitable position feedback sensor enabling closed-loop control. Theoretical analyses of the proposed actuation system are presented which model the magnetic field, force and torque exerted by electromagnetic coil on the embedded magnet. Based on the distribution of the magnetic field, an optimal geometry for the coils is proposed in order to achieve a levitation distance which is realistic for the inspection of the GI tract.

Two types of systems are investigated in the thesis, namely single-input single-output (SISO) and multi-input multi-output (MIMO), and the dynamics of these systems are modelled in state space form and hence linear controllers are designed for capsule actuation. The controllers are simulated using Matlab/ Simulink tools to realize the mathematical analysis of the system, and then implemented digitally in real-time using Texas Instruments (TI) TMS320F2812 Digital Signal Processor (DSP) to validate the proposed actuation system.

In the SISO system, a linear one degree of freedom (1DOF) proportional-integral-derivative (PID) controller is designed to move the inserted magnet in the vertical dimension within an area around the operating point and to maintain it at a desired position. A realistic simulation model is designed and implemented to evaluate the proposed controller. Simulation results have shown that the controller is able to successfully hold the embedded magnet in the desired position. For practical validation, the PID controller is implemented in real-time on the DSP system, where pulse width modulation (PWM) is generated to control the coil current, and Hall effect sensors are used for position feedback. Experimental results are obtained under step and square wave input demand.

In the proposed system, high frequency noise on the position sensor is initially rejected by hardware implementation of resistor capacitor-low pass filter (RC-LPF) circuit. The accuracy of the position feedback is increased by calibrating the DSP's on-chip analogue-digital converter (ADC) in order to reduce conversion error due to inherent gain and offset errors. To further reduce the influence of the position feedback noise, an average of ten repeated samples based on mean filter is implemented by the DSP in order to reduce the influctuation of the sensor reading. The tracking performance of the actuation system based on two Hall effect sensors on the opposite coil's poles is investigated under step trajectory input. In an improved actuation system, position feedback is provided by using an AC magnetic field to obtain the capsule position information, decoupling this from the DC actuation field. The noise of the position feedback in the improved system is reduced by replacing the PWM current drive with a linear power amplifier driven from a digital to analogue

converter (DAC), hence reducing AC interference. Positioning sensor noise was found to be further reduced by implementing digital filtering based on a coherent detector using the DSP, without increasing response time. The performance of the actuation system using these position sensors is compared based on settling time, overshoot, steady-state error, and control input parameters in order to validate the proposed improvement in the position feedback. The experimental results have shown that the controller based on both sensing strategies satisfactory control of the magnet's position. However, the response of the system based on AC position sensing has the shortest settling time, smallest overshoot value and steady-state error.

In the MIMO system, several linear controllers such as pole placement (PP), Entire Eigenstructure Assignment (EEA), and linear Quadratic regulator (LQR) techniques are designed and their tracking performances are compared. Simulation results have shown that, based on acceptable control inputs, the LQR controller has the fastest response with minimal overshoot value and steady state error. However, the LQR controller based on 2DOF is unable to maintain stable control of the magnet due to the insufficient position feedback from the two coil sensors.

Specifically, it is not possible to achieve a stable 2D system since the orientation angle of the magnet is not resolvable. Therefore, the position feedback is improved by obtaining the device position and orientation information from a pair of 3-axis orthogonal coils. A realistic simulation model for the 3DOF LQR controller is designed and implemented to evaluate the developed system. Simulation results have shown that this controller is can achieve the necessary stability.

In conclusion, based on the results from the 1D control system, the thesis shows that the DC magnetic field, which is used for capsule movement, can be also used to provide the controller acceptable position feedback. However, the use of AC magnetic field for positioning purpose provides more accurate position information. In order to implement 2DOF control system successfully, two 3-axis orthogonal coil sensors are considered which are used to provide the actuation algorithm with more accurate feedback of position and orientation information.

Contents

List of Figures

List of Tables

Nomenclature

Acronyms

ADC	Analogue-Digital Converter
AMR	Anisotropic Magnetoresistive
$ASIC$	Application-Specific Integrated Circuit
AWG	American Wire Gauge
BPF	Band Pass Filter
CE	Capsule Endoscope
$CMOS$	Complementary Metal Oxide Semiconductor
CRT	Cathode Ray Tube
D	Dimension
DAC	Digital-Analogue Converter
DFT	Digital Fourier Transform
DOF	One Degree Of Freedom
DSP	Digital Signal Processor
EEA	Entire Eigenstructure Assignement
EVA	Even-Manager A
EVB	Even-Manager B
FDA	Food and Drug Administration
FEM	Finite Element Method

GI	Gastrointestinal
GMA	Giant Magnetostrictive Alloy
GMR	Giant Magnetoresistive
GP	General Purpose
HMI	Human Machine Interface
HPF	High Pass Filter
I/O	Input/Output
IC	Integrated Circuit
LC	Inductor Capacitor
LED	Light Emitting Diode
LQR	Linear Quadratic Regulator
LTI	Linear-Time-Invariant
MFN	Magnetic Field Navigator
$MIMO$	Multi-Input and Multi-Output
$MOSFET$	Metal-Oxide-Semiconductor Field-Effect Transistor
$MPOS$	Maximum Percent Overshoot
MRI	Magnetic Resonance Imaging
$NdFeB$	Neodymium Iron, and Boron
PCB	Printed Circuit Board
PH	Power of hydrogen
PID	Proportional-Integral-Derviative
PP	Pole Placement
PWM	Puls Width Modulation
QEP	Quadrature-Encoder Pulse

$RAPID$	Reporting and Processing of Images and Data
$RC - LPF$	Resistor Capacitor - Low Pass Filter
RF	Redio Frequency
$SISO$	Single-Input and Single-Output
SMA	Shape Memory Alloy
$SQUID$	Superconducting Quantum Interference Devices
TI	Texas Instruments
WCE	Wirelwss Capsule Endoscope

List of Symbols

$(x, y, z)^T$	3D spatial coordinates
$(a, b, c)^T$	Coil's position vector
L_c	Length of the coil
W_c	Width of the coil
H_c	Height of the coil
D_w	Diameter of winding wire
$+M$	Magnetism on the surface of coil's north pole
$-M$	Magnetism on the surface of coil's south pole
i, j, k	Index numbers
$\vec{r}$	Vector defining a spatial position with respect to the coil's center
$(x_p, y_p, z_p)^T$	Spatial position vector
$\vec{\mu_c}$	Magnetic coil moment
μ_c	Magnitude of the magnetic coil moment
$\hat{\mu_c}$	Direction of the magnetic coil moment
N	Coil's number of turns
I	Coil's current
A_c	Coil's cross-section area
D_f	coil dimensions factor
θ	Coil's inclination angle
ϕ	Coil's azimuth angle
$(m, n, p)^T$	Orientation vector of coil defined by three projections
μ_0	Air magnetic permeability
μ_r	Relative magnetic permeability of the coil's iron core material
$\vec{B}$	Magnetic field density Vector
r	Magnitude of the position vector $\vec{r}$
B_T	A constant related to magnetic field density

B_x, B_y, B_z	Three projection components of magnetic intensity $\vec{B}$ in the $(x_p, y_p, z_p)^T$ spatial position
X, Y, Z	Constants related to magnetic intensity projection components
B_{xy}	Transverse component of magnetic intensity $\vec{B}$
B	Magnitude of magnetic field density Vector $\vec{B}$
D, E	Constants related to magnetic intensity projection components at spatial position closed to the coil
$F(\vec{p})$	Magnetic force vector at spatial position p
$B(\vec{p})$	Magnetic field density at spatial position p
$T(\vec{p})$	Magnetic torque at spatial position p
$\vec{\mu_m}$	Magnetic moment of permanent magnet
μ_m	Amplitude of magnetic dipole moment vector $\vec{\mu_m}$
$\hat{\mu_m}$	Direction of magnetic dipole moment $\vec{\mu_m}$
μ_x, μ_y, μ_z	Three projection components of magnetic dipole moment $\vec{\mu_m}$
F_x, F_y, F_z	Three projection components of magnetic Force
$(s, t, u)^T$	Orientation vector of capsule
β	Capsule's inclination angle
α	Capsule's azimuth angle
η	An angle between the coil moment axis and the position vector $\vec{r}$
F_r	Magnetic force component in position vector $\vec{r}$ direction
F_ψ	Magnetic force component in in radial direction of F_r
ψ	An angle between coil's reference and position vector direction $\vec{r}$
γ	An angle between coil's reference and capsule direction $\vec{r}$
ρ	Magnetic force's inclination angle
τ	Magnetic torque amplitude
R_T	Response time of the coil

Chapter 1

Introduction

1.1 Introduction

Digestive tract disorders, such as ulcerative colitis and colon cancer, are considered one of the most common fatal human diseases. However, early detection of gastrointestinal (GI) cancer can contribute to its cure. There are several medical procedures, which can be adopted to diagnose the pathologies of the GI tract without the application of intrusive medical devices, such as the endoscope, double-contrast barium enema and stool test. GI endoscopes in particular are considered worthy and irreplaceable medical tools as they enable the surgeon to evaluate the digestive tract of the patient based on real images.

1.2 Endoscopes

Many important diseases of the GI tract are currently diagnosed by using minimally invasive methods, which allow an endoscopist to enter a medical device through oral or rectal orifices, or small incisions made by surgeon in suitable places near the investigated organ, not only to evaluate visually the interior surfaces or tissue of a tested organ, but also to enable the taking of biopsy samples of foreign objects. This medical procedure is called endoscopy [1]. A common application of endoscopy is the examination of the GI tract of the human body Fig. 1.1. Current digestive tract endoscopes can be categorized into two types: wired active endoscopes and wireless passive endoscopes.

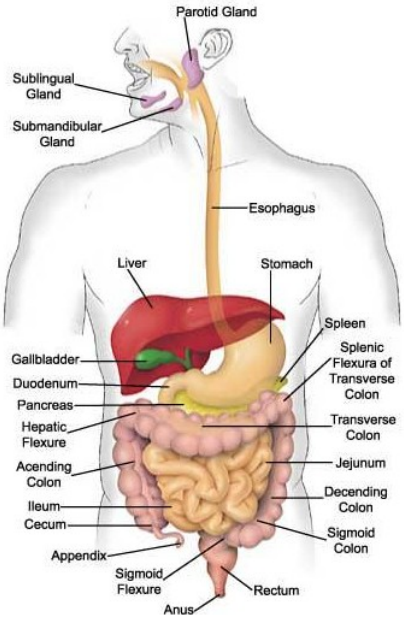

Figure 1.1: GI tract of the human body.

1.2.1 Wired Active Endoscopes

Cabled endoscopes are conventional endoscopic technologies which are used for the reliable and detailed analysis of the digestive organs, oesophagus, stomach and bowel. Unlike most other medical devices, they are directly inserted into the tested digestive organ. Typically, there are three kinds of traditional endoscopes to evaluate specific organs [1][2],

- **Gastroscope**. This is passed through the oral orifice and used to examine the upper digestive tract, the oesophagus, the stomach, and the duodenum
- **Push enteroscope**. This is entered via the anal orifice and is used to evaluate the upper small intestine.
- **Colonoscope**. This is also passed through the anal orifice and exploited to test the colon and rectum.

The endoscope, which is basically a long, thin and rigid or flexible fibre optic tube, includes the following schemes [1][3][4]:

- **Imaging system**. This is based on a miniaturized colour camera fixed on the end of the tube and used to visually inspect the organ. The scheme is provided by an optical fibre unit, which is used to coherently transmit an image and to direct the light generated from the source outside the patient's body to the tested organ.

- **Mechanical system**. This is used to tract the imaging device tip.
- **Controllable system**. This is composed of water/air and biopsy/suction control units. The insufflation of air by the water/air unit is used to distend the walls of the examined organ in order to enable the passage of the endoscope. The aspiration of the contents from the digestive tract is examined by the suction capabilities of the biopsy/suction unit. Otherwise, the view of the evaluated organ is obscured by its fluid.

After passing this imaging scope through the GI tract, the endoscopist can directly see the inside lining of the digestive organ under investigation with a cathode ray tube (CRT) monitor or any other video display unit.
However, the application of this type of wired examination procedure has many drawbacks. First, the manual insertion of the imaging tube is a tedious and cumbersome process for the endoscopist [5]. Additionally, it causes discomfort to the patients as it needs flexible, relatively wide cables to be pushed into the digestive organ which are used to carry power, light, and video signals [6][7]. Furthermore, the examination of the GI tract is limited since most of the small bowel cannot be visualized without an incision, due to the difficulty of passing the cabled camera through the small bowel with its tortuous nature [8]. Moreover, examination of the upper small intestine based on the push endoscope is not successful because of the difficulty of its manipulation by the surgeon. The reason for this is that the bending capability of commercial endoscopes at their tip is limited and the shape along the rest of their length is not controlled. Lastly, conducting the examination requires sedation or anaesthesia or air insufflation of the intestine [9][10]. Finally, it needs to be performed by a skilled physician [11]. For these reasons, therefore, there is an urgent clinical need for improved techniques of evaluating the small intestine without any inconvenience for the patient.

1.2.2 Wireless Capsule Endoscope

A Wireless Capsule Endoscope (WCE) is a healthy monitoring device provided by a digital camera, and is used to examine the entire GI tract, without discomfort or the need for sedation, as it transmits pictures wirelessly from inside the human body. The idea of a radio transmitting capsule was first presented in 1957 by the Rockefeller Institute of New York [12]. The proposed pill-shaped device was 1.125

inches long and 0.4 inch in diameter with a plastic body resistant to the action of digestive juices. It contained a small 1MHz transistor oscillator and a replaceable battery which was placed in one end of the medical device and which supplied electric power for 15 hours. The other end of the device was sealed by a rubber membrane which was used to transmit the variation in human body pressure to the coil armature, thus varying the radio signal frequency.

Once the ingestible capsule was swallowed by the patient and its navigation tracked through the digestive tract, it transmitted varying frequency signals based on changing GI tract pressure. These transmitted information signals were picked up by a receiver circuit with an antenna fixed near the human body. The received signals were then processed and finally displayed on a CRT monitor.

At almost the same time, the University of California developed another radio transmitting capsule 28 mm long and 9 mm in diameter for monitoring environmental blood pressure, temperature, and power of hydrogen (PH) value [13] [14]. In spite of the limited clinical applications of these disposable pills, they contributed to the development of the invention of the video capsule endoscope.

In May 2000, Given Imaging Ltd released the first wireless capsule endoscope called the M2A Diagnostic Imaging System, which was small enough to be swallowed (11 mm diameter and 26 mm in length) [3]. Its internal composition is illustrated in Fig. 1.2, and mainly includes a camera, an advanced application-specific integrated circuit (ASIC) video transmitter, lights and a battery. The video camera was comprised of a complementary metal oxide semiconductor (CMOS) imager designed especially for direct imaging within the digestive tract, a short focal length lens, a lens holder, and an optical dome. The illumination system was based on four optoelectronic light emitting diodes (LEDs) to ensure proper lighting for capturing pictures. Two silver oxide batteries were used to supply the medical device functions with electrical power for eight hours. Finally, an radio frequency (RF) transmitter and antenna were taped to the capsule body which was used to transmit the video images.

It is worth considering that the use of the CMOS imager, which requires much less current than a charge-coupled device for comparable image quality, and the ASIC transmitter, contributed to the reduction of the power consumption and, consequently, saved the available energy of the battery for the imaging trip of the capsule through the digestive tract [15].

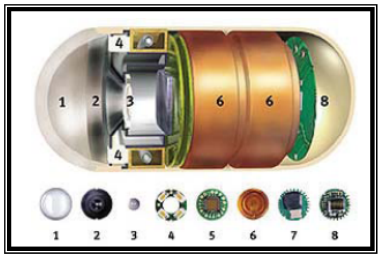

Figure 1.2: Internal structure of the M2A capsule endoscope: 1. optical dome, 2. lens holder, 3. short focal length lens, 4. four LEDs, 5. CMOS image sensor, 6. two batteries, 7. ASIC RF transmitter, 8 antenna [14].

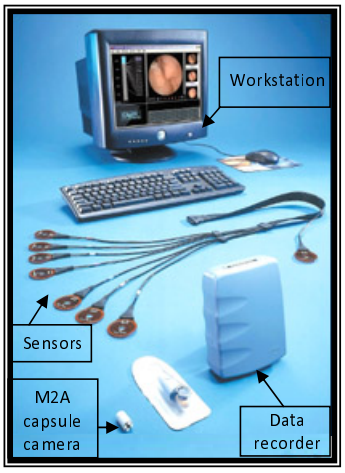

Figure 1.3: M2A capsule endoscope scheme [2].

The Given Diagnostic Imaging scheme consists of three stages: the imaging capsule, the data recorder, and the workstation as shown in Fig. 1.3. In the first stage, a disposable, swallowable capsule acquires video images at a rate of two images per second during its passive navigation by peristalsis of the GI tract. Based on the transmitter and antenna means, the image information is then transmitted outside the patient. In the second stage, the transmitted data are received by sensors array placed on the patient's abdomen and then subsequently stored in a data storage unit of an external recorder places on a belt around the patient's waist. In the final stage, the image data are reclaimed from the recorder and sent to the workstation equipped with Given Imaging's RAPID^{TM} (Reporting and Processing of Images and Data) proprietary software, which is used by the endoscopist to display, evaluate, and archive the video images [3].

The capsule endoscope M2A, which was renamed to PillCam later, received approval from the Food and Drug Administration (FDA) in 2001 for use in patients [2] [16]. The camera in a pill represents a great breakthrough in the GI tract diagnosis because, it not only diminishes the suffering caused by a traditional endoscope

manually inserted in a gastrointestine, but is also able to reach areas of the small intestine that cannot be explored by traditional endoscopic means [17] [18] [11]. Therefore, it has quickly captured widespread attention and incredible interest from endoscopists and bio-engineers. Since then, many other companies have released similar capsule cameras and achieved a great deal of scientific research in this field, such as the RF System Lab [19] and Olympus Corporation [20] in Japan, the Chong Qing Jin Shan Science and Technology and Institutes in China, and the Korean company IntroMedic [2].

1.3 Challenges of Capsule Endoscopes

The technique of the WCE has revolutionized the examination of the intestine; however, compared with traditional endoscopes, it has some technical limitations and challenges to overcome before its adoption as a commercial diagnosis tool in hospitals. Firstly, the capsule camera cannot be guided to point to a special examination direction nor to stop at a site for interactive examination. This is because it is moved passively by the natural GI peristaltic movement and gravity. Hence, it is possible that some important GI portions [8] may not be photographed. Secondly, the power capacity of the capsule batteries is insufficient to complete imaging of the whole bowel, as the device's passive navigation through the whole human GI tract takes about 20 to 36 hours, but the battery can only supply electric power for eight hours [21][22]. Finally, the capsule is not able to take biopsy samples from the target GI tract or perform any treatment procedure, such as the removal of polyps, as a traditional catheter endoscope can [2]. To overcome these obstacles, a new capsule endoscope with a locomotion mechanism should be proposed in order to improve the GI tract evaluation and control the medical device's functionality.

1.4 Active Capsule Endoscope

Development and improvement of the WCE has been continuously considered by many researchers and bio-engineers. Because major drawbacks of the endoscopic capsule are associated with its uncontrolled movement, it is a key point to give the endoscopist the ability to remotely manipulate the capsule through the digestive tract effectively [23][24]. Hence, the medical device can be externally guided to

examine and stop at any interesting spots for additional images, and can navigate the unimportant digestive regions at a much faster speed than the passive movement by the natural GI peristaltic waves and gravity [23][6][25][26][27]. Additionally, with scientific advances in gene therapy and nano-technology, such an active capsule endoscope can have injection, laser, microwave and radiation capabilities. These can be exploited to achieve many therapeutic treatments like biopsy, drug delivery [15] [28] curtailment of bleeding and the cutting out or removal of a tumour by a remote laser in a capsule [29].

In the last three decades, there has been a considerable interest by many researchers in methods of controlled actuation for these devices. A number of internal and external locomotion approaches, based on different actuation force sources, have been proposed for endoscopic capsules. The most promising of these actuation techniques are presented and discussed in the literature review in Chapter 2. The majority of these methods are based on magnetic actuation, which is a potential solution for remote capsule actuation. The reason for this is that there is no need for any cable or wire to transmit the force, and that a permanent magnet does not need a source of electrical power. In addition, the permanent dipole could be manipulated remotely by the force and torque of an external magnetic field. Furthermore, the motion trajectory of the magnet can be tracked through analysis of its magnetic field distribution. By inserting a small permanent magnet inside the capsule, localization information of the device may be obtained. The human body, moreover, has no effect on the distribution of the magnetic field due to its low magnetic permeability, which is the same as a vacuum. One other advantage is that the control scheme can be performed with low cost [14][30][31]. However, there are some drawbacks related to the magnetic navigation approach. One is that the magnetic force is reversely proportional to the fourth power of the distance between the coil and the magnet. Another is that the large suspension force for human application at a distance of $(15 - 20)$ cm means a large number of coil turns and a high current, leading to an increased response time in the actuator and power consumption problems, respectively.

1.5 Contributions

The objective of this thesis is to design a control system to enable endoscopists to remotely guide and actuate an endoscopic capsule inside the colon. The subject of the proposed manipulation system is based on the magnetic levitation concept which is considered a potential solution for capsule manoeuvring in the GI tract. During the course of this thesis,

1. Magnetic field, force and torque are analysed for various actuation schemes.

2. Design and implementation of a 1D magnetic actuation system for the WCE based on position feedback and using Hall effect sensors are explored. This process involved several steps including:

   - System design and dynamic modelling.
   - Feedback controller design for the system.
   - System simulation.
   - Magnetic actuator fabrication.
   - Signal conditioning circuit design and implementation.
   - Real-time controller implementation on a DSP.

3. The position feedback of the 1D control system is improved by using an AC magnetic field and coil sensor to find the capsule position, eliminating the influence of the actuator field.

4. There is optimisation of the response time of the control system and reduction AC interference on the coil sensor signal by a linear power amplifier driven from a digital to analogue DAC instead of the puls width modulation (PWM) approach.

5. Further reduction of the position noise is achieved by implementing digital filtering based on coherent detection in the DSP.

6. Several 2D control systems are designed, modelled, simulated, fabricated, and finally implemented digitally in DSP based on LQR, separated PID, and bang-bang techniques.

7. The position feedback of the 2D simulation design is improved by using a pair of 3-axis orthogonal coil sensors to provide the actuation algorithm by position and orientation information of the capsule.

8. A realistic simulation model for a capsule actuation system based on 3DOF LQR controller technique is designed and simulated in Matlab/Simulink to validate the improved scheme.

9. Finally, to increase the maximum levitation distance to a realistic value for the colon inspection, an optimised proposed system was designed based on Comsol software for future control system in terms of increasing current, number of turns in the coil, using a high permeability iron core, and finally optimum coil structure design.

In summary, a very stable 1D control system is successfully implemented based on DC magnetic position feedback. However, a more stable and robust control system is achieved by using an AC magnetic position signal and digital filtering. The successful implemented scheme can be adopted to actuate the capsule endoscope through the whole digestive tract by moving the actuator frame based on a 3DOF robotic manipulator. For a 2D control system, a better position feedback system is required to implement an effective movement and rotation control system in colon through providing the actuation algorithm with more accurate capsule position and orientation information.

1.6 Publications Arising From This Research

1. I. K. Mohammed, B. S. Sharif, J. A. Neasham, and D. Giaouris "Novel MIMO 4-DOF Position Control for Capsule Endoscope" Proc. of the IEEE ISCAS, Rio de Janeiro, Brazil, 909-912 May 2011.

2. I. K. Mohammed, B. S. Sharif and J. A. Neasham, "Design and Implementation of a Magnetic Levitation Control System for Robotically Actuated Capsule Endoscopes ," Accepted in IEEE ROSE2012 conference, Germany, November 2012

3. I. K. Mohammed, B. S. Sharif and J. A. Neasham, "Design and Implementation of an Effecient Positiong System Based on Coil Sensor for Capsule Endoscope," Presented as a poster paper in Digital Institute Event, Newcastle University, September 2012.

4. I. K. Mohammed, B. S. Sharif and J. A. Neasham,"Study of 1D and 2D Magnetic Actuation and Positioning Systems for Capsule Endoscope" under preparation to be submitted as a journal paper.

1.7 Thesis Outline

The thesis is organised as follows:

Chapter 2, includes two main parts. In the first part, the background and types of gastrointestinal endoscopes are presented, followed by internal and external proposed locomotion mechanisms for CE. The theory of the proposed SISO and MIMO controllers for an endoscopic capsule is presented in the second part.

In Chapter 3, mathematical analysis of magnetic field distribution around coil is presented. It also states mathematical analysis of the magnetic force and torque exerted by the actuator on a permanent magnet inside the endoscopic capsule. For colon inspection purposes, proposed actuator coil design based on Comsol software for realistic levitation distance is finally presented in this chapter.

Chapter 4, contains first original contribution of the thesis. It provides simulation for both SISO and MIMO control systems. In the SISO system, dynamic modelling and simulink design based on 1DOF PID controller using Hall effect and coil sensors are presented. For the MIMO scheme, dynamic modelling and simulation design of 2DOF controller based on pole placement (PP), entire eigenstructure assessment (EEA), and Linear Quadratic Regulator (LQR) techniques are introduced. Finally, design and simulation for 3DOF linear control system based on the LQR approach are also presented in this chapter.

In Chapter 5, the background and theory of two kinds of magnetic sensors, Hall effect and coil, are presented. Position algorithms for an endoscopic capsule based on these sensors with their circuits design and implementation are also introduced. Finally, improvement of the position feedback accuracy based on a coil sensor using the Discrete Fourier transform (DFT) technique is presented.

Chapter 6 introduces real-time implementation of the SISO and MIMO simulated systems based on the processor TMS320F2812 DSP in order to validate the proposed actuation systems. Experimental results of the control system are included in this chapter to confirm performance of the navigation system. Finally, conclusions are given in Chapter 7 and the thesis ends with recommendations for future work.

Chapter 2

A Review of Existing Actuation Methods and the Background to the Proposed Actuation System

This chapter includes two main sections. In the first section, a literature review of potential existing actuation methods for capsule endoscopes is introduced. The background and theory of SISO and MIMO controller techniques for the proposed actuation system are considered in the second section.

2.1 Capsule Endoscope Actuation

Endoscopists and bio-robotic engineers have for some time been considering the design and control of schemes that contribute to the locomotion and orientation of the capsule in the digestive tract. There are many methods that can be adopted to actuate the objects. However, using the most common approach, the rotating electric motor, is considered an inapplicable procedure for the WCE due to the difficulty of inserting the motor inside the small sized medical device. Moreover, the motor needs an operating power which will shorten the long life of the capsule batteries. This means the duration that an electric motor does not supply sufficient power to the medical device for whole digestive tract evaluation [32]. Therefore, the designers proposed other possible methods which can be applied to navigate the WCE in the GI tract. These approaches will be addressed in turn as internal and external capsule actuation techniques.

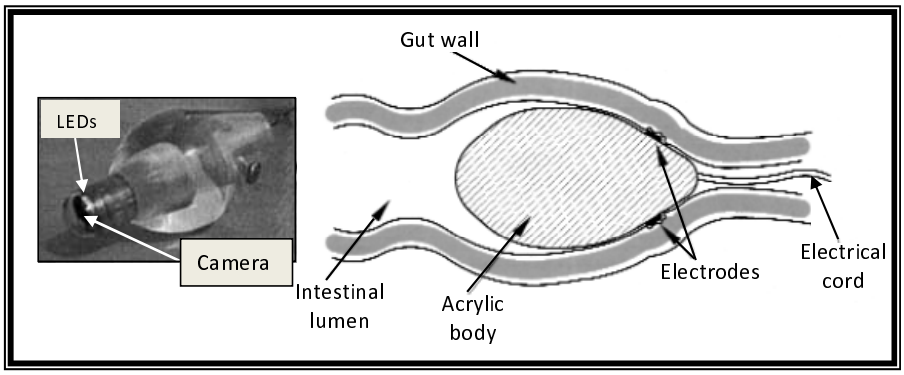

Figure 2.1: A ovoid-shape endoscope that propels itself through the intestine via electrically stimulating contractions of the gut [34].

2.1.1 Internal Capsule Guidance Methods

Many researchers have proposed different locomotion methods for a capsule endoscope based on the idea of attaching an active propelling device to the capsule. So far, such a navigation concept has been the object of many endoscopists and bio-robotic engineers. Gong et al. [33] presented their conceptual scheme for a capsule endoscope as a joystick which not only communicates with the WCE but also controls illumination, picture capturing, and data transmission from the device. However, there is no control over the motion of the capsule.

Alexander Mosse et al. [34] proposed the first locomotion mechanism for a capsule endoscope. They fabricated an acrylic ovoid-shaped endoscope provided by two stainless steel electrodes mounted on the tapered section, which is used to apply electro-stimulation to the intestine wall. Fig. 2.1 shows schematic diagram and prototype of the proposed ovoid-shape endoscopic capsule. The stimulation causes a circular muscle contraction, which might propel the capsule within the digestive tract. The experimental tests were carried out to evaluate the actuation performance of the proposed locomotion scheme. Another locomotive mechanism based on an electrical stimulus for small intestine navigation is proposed by Woo et al. [35]. By contracting the bowel by electrical stimulus the capsule can propel itself in the opposite direction, which can enhance speed of movement and change the direction of the device. In vitro tests using a pig's small intestine were carried out to assess the actuator locomotion. The experiments showed that the electric excitation of the bowel does not move the capsule quickly, and its movement is not smooth and controlled.

Louis P. et al. [36] introduced an inchworm locomotion model for the capsule en-

doscope based on extensor and clamper mechanisms to propel the device forward through the first tract of the colon. Experimental results and analysis of the locomotion efficiency are reported.

Researchers have focused on bio-inspired mechatronic methods for the actuation of the WCE. A series of active actuation mechanisms based on bio-inspired legs have been developed by the research team of CRIM Lab [2]. Menciassi et al. fabricated a capsule-type micro robot with a legged locomotion mechanism based on a sliding clamper solution [37] [38] and shape memory alloy (SMA) clamping devices [39] for semi-autonomous colonoscopy. The proposed legged locomotion systems are designed to have self-propelling and guiding abilities. For controlled pneumatic actuation power, a control system is needs to be applied, which is usually quite large and unsuitable for wireless movement. Therefore, this team has started to develop a device with SMA legs [40] [41], which are driven by micro stepper motors.
The locomotion mechanisms for on-board actuation of the legs have been developed and evaluated in vivo experiments. However, there are many drawbacks related to the proposed model; firstly, its positioning is still ill-controlled as the proposed mechanism is based on the SMA actuation. Furthermore, the hook actuation needs more electric power than it is possible to provide from the capsule batteries. Finally, the locomotion of the device with this legged mechanism system is not wireless, as it is still wired with a supplying electric power.
Kim et al. [27] [42] proposed a capsule prototype with a locomotion mechanism based on SMA springs and micro hooks. Authors fabricate a prototype locomotion system inserted in a dummy capsule using micro brushless motors, an ionic polymer metal composite actuator, SMA springs, and clampers. In the proposed active mechanism, four SMA springs are chosen to be microactuators for the capsule, and stopping devices are based on four biomimetic clampers. The actuation of the robot is based on heating and cooling of the springs, heating achieved by ohmic heat, generated by the current flowing through the springs. By repeated cycles of heating and cooling process, springs connector can move forward. The in vitro tests were carried out to evaluate the movement ability of the robot capsule.
However, the proposed actuator is not able to move backward for additional evaluation. Furthermore, the experiments showed that the proposed method was not as efficient for capsule actuation, and the average moving speed of the actuator was

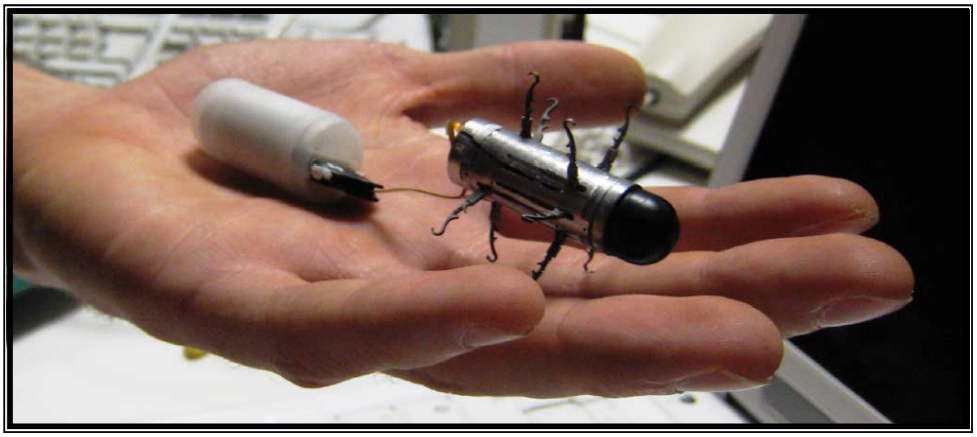

Figure 2.2: Robot endoscope [43].

slow at approximately 14.7 mm/min. The reason for this is that the increase in the clamping failures is associated with the deformation of the colon's shape. On the other hand, heating and cooling of the SMA actuator are required in order to achieve the capsule movement in the tested digestive tract, and because the human body is a closed environment, the cooling speed of the actuators is very slow, thus reducing the speed of the robot. In order to increase the actuator speed, a sequential control with two or more clamping modules are required. Moreover, the actuation of the capsule with this locomotion mechanism is not wireless as it still needs to connect to external power via electrical wires. Thus it is difficult to include the actuator and the power supply within a swallowable capsule. Finally, the micro robot was not designed based on capsule functions such as a micro camera, an RF system etc, and its actuation was not even evaluated for in-vivo test.

Wang et al. [7] fabricated a prototype of a new magnetic actuator system based on an inchworm-like locomotion mechanism with a reasonable size of capsule endoscope. The actuator is composed of a permanent magnet, a plunger, a solenoid, and a cone-shaped polymer. By applying an alternating current to the solenoid, the dipole will make a vibrating movement based on the electromagnetic force. With the directional difference of friction produced by the cone-shaped polymer, the actuator could achieve a forward displacement on the 2D surface. Experiments based on two types of surface were carried out in order to study the effect of the various frictional coefficients and find the suitable exciting voltage and frequency which governs the actuator's velocity. The actuator still needs to connect to an external power supply via cables, which make its use in the WCE impossible. Furthermore, the actuator is not validated based on the capsule functions such as camera, illuminating LEDs,

transmitter and so on. Finally, further investigations of its controllability and safety should be considered for use on a patient's body.

Valdastri et al. [43] proposed a new active locomotive mechanism for the capsule endoscope. They fabricated a prototype of a legged endoscopic capsule robot with mechanical components matching the dimensions of a commercial WCE. The robotic capsule had 12 legs made of superelastic SMA and ending with hooks for friction proposes. These were placed axially nearer the centre of the device to enhance turning as shown Fig. 2.2. Control of the legged capsule's movement is based on a human machine interface (HMI). The in vitro and in vivo tests were carried out to evaluate the locomotion ability and the velocity of the capsule based on the proposed locomotive mechanism. The experimental tests proved that the legged robotic capsule could proceed with a maximum speed of 50 mm/min and stop in the colon. However, the proposed legged robotic device still needs to connect to external power using wires, so it is difficult for this technique to be used in the WCE. Additionally, further investigations of actuator safety are required before it is used in the human body. Finally, the speed of the proposed legged robotic capsule is still not high enough as the evaluation procedure of the whole colon is based on the maximum robotic capsule speed, and needs more than 30 minutes, which is long time compared with the evaluation time based on another capsule robot proposed by Park et al. [44] .

The proposed robot, which is based on paddling locomotive mechanism, can propel itself by six paddling legs driven by a linear actuator based on a stepper micromotor and lead screw together with two mobile cylinders inserted inside the capsule. The structure of the 13 mm x 30 mm capsule-shape microrobot is shown in Fig. 2.3. The in vitro tests using a porcine small intestine showed that the microrobot could move with a velocity of up to 6.42 mm/s.

However, the experimental study was achieved on a micorobot device structure without any endoscope functions. Furthermore, the micorobot was powered externally through wires that prevent the possibility of using it in the WCE. Lastly, the moving speed of the robot still not high enough. Therefore, the research team developed their micro robot and fabricated a modified wireless paddling-based locomotive capsule endoscope as shown in Fig. 2.4 [45]. The in vivo experiments in the colon of an anesthetized pig showed that the paddled capsule endoscope could move forward and backward with an average velocity of 17 cm/min coordinately the evaluation of

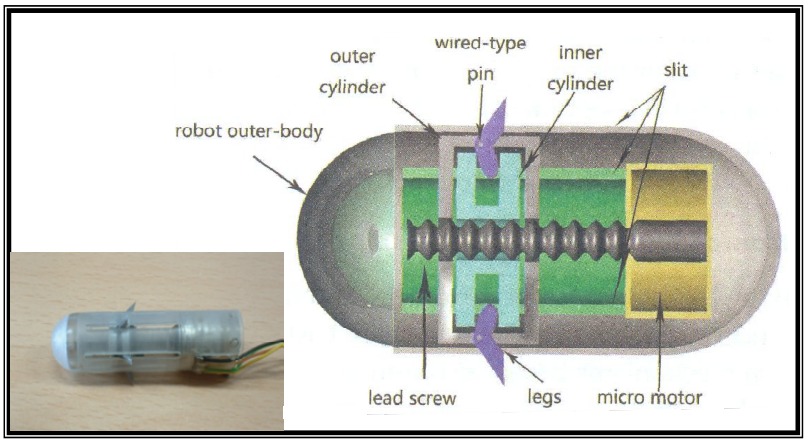

Figure 2.3: Internal structure of a paddling based microrobot for capsule endoscope [2].

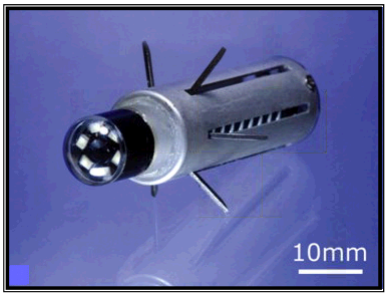

Figure 2.4: Prototype of developed paddling based robotic capsule endoscope [45].

the colon takes 20 minutes. However, further assessment of its controllability and safety is required before adoption in the diagnosis of human digestive organs.

Wang et al. [46] developed a hybrid active locomotion system for capsule endoscope combining internal actuation mechanism and external magnetic guiding. They fabricated an internal actuator based on a micro motor integrated on-board a capsule dummy for driving force. A small cylindrical permanent magnet is embedded in the capsule used to control the device's orientation and enhance the driving force through its interaction with an external magnetic field generated from a cuboidal permanent magnet fixed on a 6DOF robotic arm. The 18 mm (diameter) 64 mm (length) prototype of the capsule-shape microrobot and its internal structure are shown in Fig. 2.5. Rotating the motor by a controlled electrical power from the inserted batteries will move the capsule forward and backward by the spiral structure fixed on its body. The external guidance based on the external magnetic field will enhance continuity of the rotation movement and control the capsules orientation during evaluation procedure.

The in vivo tests showed that the dummy capsule with the wireless internal actuator

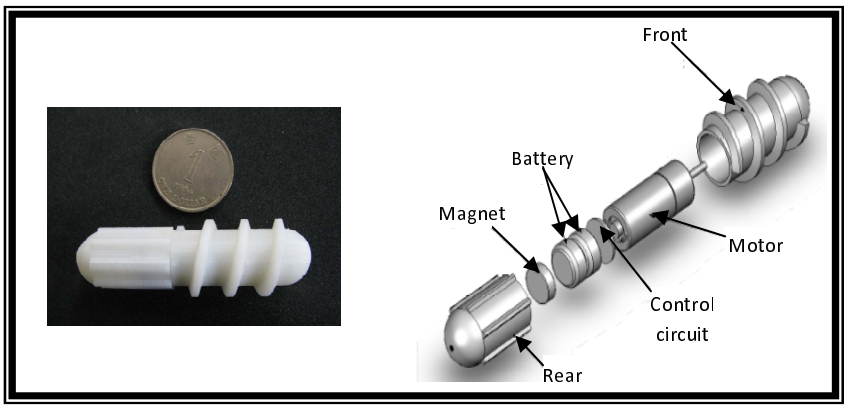

Figure 2.5: Prototype of a capsule-type robot with external guidance for capsule endoscope and its internal components [46].

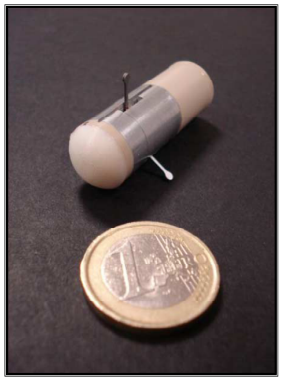

Figure 2.6: Prototype of a hybrid capsule-shape micro robot [47].

and external guidance system could achieve controlled movement with a maximum velocity of 4.2 mm/s in the porcine large intestine. However, the battery power was only sufficient to run the motor for a few minutes and, moreover, the moving speed of the actuator was not high enough. Finally, further miniaturization of the size of the proposed internal actuator is required for installation in the capsule endoscope.

In 2010, a new hybrid miniaturized endoscopic capsule for the digestive tract evaluation is proposed by Simi et al. [47]. They fabricated a prototype capsule-type micro robot with a hybrid active locomotion system which merges with an internal actuation mechanism with external magnetic dragging. The internal actuator is based on a micro motor, which is inserted with a supplying battery in the capsule, to drive the legs fixed on the body of the device. The external actuator is based on the magnetic interaction between a set of small cylindrical permanent magnets embedded in the capsule and a big external cylindrical permanent magnet mounted on a passive hydraulic arm controlled by the operator.

Fig. 2.6 shows a prototype model of the proposed capsule-shape micro robot. In the proposed navigation system, the internal legged mechanism is actuated whenever the device gets lodged in the tissue folds of the GI tract in order to free the capsule from the collapsed regions so that dragging the capsule magnetically becomes feasible and effective. The in vivo and in vitro experiments were carried out to validate the proposed hybrid locomotion system. The practical tests based on the in vitro tests showed that the proposed hybrid capsule could proceed with a maximum moving speed of 8 cm/min. It is worth considering that the achieved speed based on the hybrid locomotion scheme is considered the higher compared with their previous legged capsule prototypes. The 4-leg, 8-leg, and 12-leg capsule speeds were 3 cm/min, 4 cm/min, and 5 cm/min respectively [48][49][50].
However, the actuation of the proposed hybrid locomotion mechanism was not validated for capsule endoscope functions and the supplying ability of the inserted battery. Additionally, further miniaturization for the hybrid capsule size is required in order to achieve a swallowable capsule size.

Several kinds of active locomotion mechanisms have been proposed for capsule endoscope. However, most of these techniques are complex and their performance is still inadequate due to the inability to achieve a stable and smooth movement with a steady speed in the tested digestive organ. Therefore, the controllability of these approaches still needs further improvement. Additionally, further investigations for their safety also need to be considered for the human body.
On the other hand, some of the proposed methods, such as an inchworm-like locomotion, SMA-based locomotion, and stimulation-based mechanisms, still need to connect to an external power supply using electrical cables due to the large electrical power required to drive their actuators, so it is difficult for these capsule-shape robots to be used in the WCE. Moreover, further size miniturization for most proposed robotic navigators is required in order to achieve a swallowable pill size. Finally, the actuation performance of most proposed locomotion mechanisms has not been not validated for capsule endoscope functions [2][7][27][36][42][43][46-50].
Consequently, due to the above difficulties and drawbacks associated with the use of some active locomotion devices, another propelling method in passive mode has been proposed by many research groups for capsule endoscopes based on the force and torque produced by the external magnetic field. This is discussed in the next

section.

2.1.2 External Capsule Guidance Methods

External actuation can be achieved by using small permanent magnets inside the endoscopic capsule coupled with an external magnetic field, generated either by electromagnetic coils [51] or permanent magnets [9][11]. This method does not require supplying electric power from the on-board battery, hence saving available energy to operate other different device functions. [47].

In 1991, Fukuda [52] proposed the control and actuation idea of a micro mobile robots without any electrical wires or cords based on an external electromagnetic field generated from coil. The presented method could be used for small pipe inspections and the bio-medical field. A Giant Magnetostrictive Alloy (GMA), which does not need any power supply wires, was used as a macro actuator to move legs fixed on the bodies of two types of cableless mobile microrobots. The actuation of the proposed microbobots is based on the inchworm-type locomotive mechanism. The motion depends on the expansion and contraction of the actuator which are controlled by regulation of the coil position. The experimental tests showed that the non-contact type of actuator could proceed with a moving speed of 0.75 mm/sec based on an exciting current with an amplitude of 3.2 A and frequency of 80 Hz. However, the proposed mechanism is not validated based on the in vitro tests. Furthermore, development of the robot's velocity is required in addition to further investigations of the mechanism's controllability and safety, which need to be considered for the human body. Therefore, the development and improvement of the capsule's actuation methods has been a target of many engineers and research centres. Guo et al. [53] proposed another in-pipe micro robot driven on the basis of a screw mechanism which can be used in the medical field and industry applications. Experimental tests have taken place on the cableless micorobot to evaluate its navigation ability. The practical results showed that the in-pipe actuator could propel itself forward with a moving speed of 42 mm/s. However, the proposed actuation system is not validated based on the GI in vitro and in vivo tests.

For the purposes of the GI tract inspections, a new capsule actuation system has been proposed by a Japanese company "RF System Lab". They fabricated a

(a) NORIKA 3 capsule.

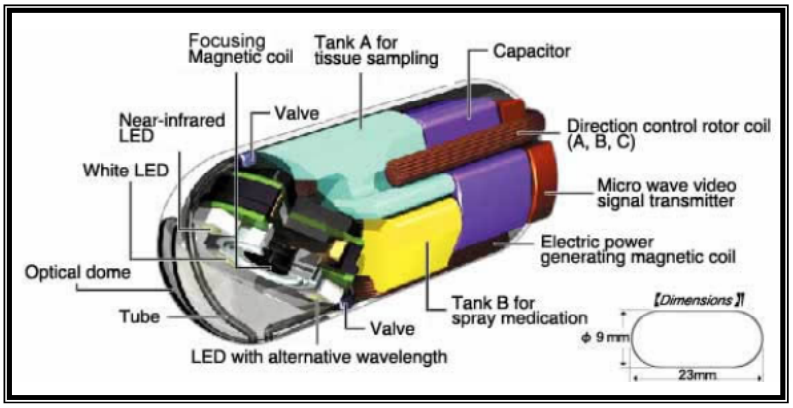

(b) Capsule internal structure.

Figure 2.7: NORIKA 3 wireless capsule endoscope and its internal structure [19][54].

prototype of a robot capsule endoscope as shown in Fig. 2.7(a); definition of its internal structure is presented in Fig. 2.7(b) [54]. Wireless power transmission is adopted to externally power the actuating device.

A schematic drawing of the proposed locomotion mechanism is depicted in Fig. 2.8. Three coils are situated at 60-degree intervals inside the capsule body, which plays a role akin to rotor coils, while three other coils inserted in a vest-like jacket act as starters. An external power unit is used to transmit electric power wirelessly in order to charge the capsule capacitor. Through the quick release of the charged energy to the rotor coil, a strong magnetic force is generated within a short period of time so as to rotate the medical device. The magnetic field's direction of the stator decides the rotation direction, and thus drives the capsule forward or backward. In the proposed control mechanism a remote operation with a joystick is used not only to

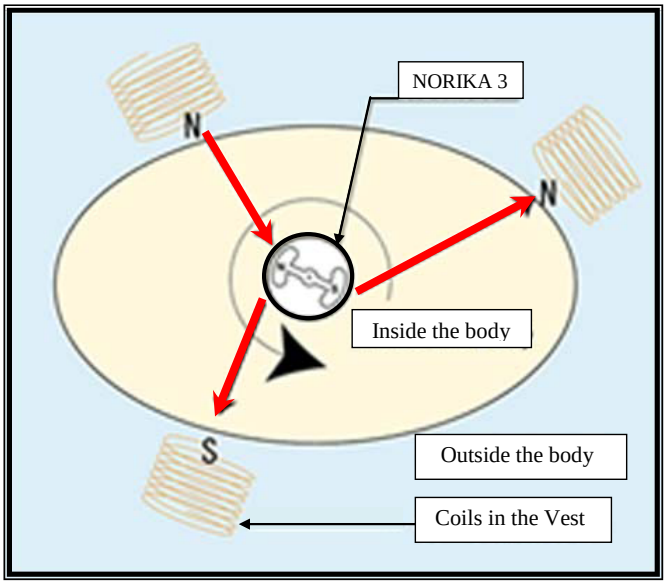

Figure 2.8: NORIKA 3 rotation mechanism [54].

control the capsule rotation movement but also to adjust the device lighting volume and switch it to infrared spectrum for multiple analysis. However, this locomotion mechanism is unable to control the orientation angle of the capsule [2][19] .

In 2004, another Japanese company, the Olympus Medical Systems Corporation also adopted a new magnetic guidance method for a capsule endoscope, developed by Sendoh et al. at Tohoku University [55] [56]. They fabricated a capsule dummy actuator for the colonoscopic navigation scheme, with the actuator being composed of an axially magnetized permanent magnet inside a capsule with a spiral structure made of rubber. The inserted magnet is rotated wirelessly by applying an external rotational magnetic field; and thus the capsule moves forward and backward by the spiral structure, as demonstrated in Fig. 2.8. The in vitro tests were carried out to examine the locomotion performance of the dummy capsule based on the proposed mechanism. The experiments proved that the capsule movement speed depends on the height of the spiral structure. It is worth considering that this locomotion technique needs a uniform external magnetic field in any direction, which may be created by three pairs of orthogonal coils placed outside the human body.
Although the proposed mechanism can achieve both forward and reverse capsule motion, it has some drawbacks. Firstly, its actuation system is based on open-loop control system. Secondly, the exciting currents of the external magnetic sources seem to be too high. Lastly, the rotational movement of the capsule could cause

blurring in the captured images.

Therefore, an alternative proposed scheme is considered, as developed by Hu et al. [8][22]. They used a magnetic localization and orientation sensor array system to measure the position and orientation of the embedded magnet. They implemented a closed-loop control system to adjust the current of the three pairs orthogonal coils based on the information from the sensors. Based on the regulated rotational magnetic field, the capsule with the spiral structure can propel forward and backward. Analysis of the magnetic force and the magnetic field distribution, together with the simulation of the proposed actuation system, are reported. However, the proposed method is not validated in real-time experiments.

In 2011, this idea was similarly proposed for GI tract examinations by Zhong et al. [57]. They inserted a small permanent magnet in a dummy capsule and used an external rotary magnetic field produced by two pairs of orthogonal rectangular coils to rotate the device. With the help of the spiral structure on its surface, the device can move forward and backward. Validation of the proposed scheme in the in vitro tests was carried out. Regarding the simulation analysis, the thickness of the coils winding was taken into consideration in the analysis of the magnetic field distribution. In addition, simulation experiments were carried out to analyse the relation of the size of the electromagnets and the character of the magnetic intensity distribution. However, as well as the blurring problems of the captured pictures, as mentioned earlier, the propulsion capsule force is not controlled as the position feedback is not considered in the proposed actuation algorithm. Moreover, the orientation of the capsule is not controlled.

Hong et al. [58] fabricated a new preliminary magnetic actuation system for a capsule endoscope based on a twistable thread module mechanism. They inserted two disc-type permanent magnets inside the MIRO capsule endoscope with its magnetization direction perpendicular to the central axis; these dipoles acted as an internal armature magnet. Fig. 2.9 shows the prototype of the capsule-type actuator. An external permanent magnet, which was used as a source of actuation magnetic field, was connected across an electric motor and then fixed on a 5DOF (x,y,z,θ,ϕ) movable frame. Rotating the external permanent magnet by the motor, and having its symmetrical axis parallel to that of the capsule, also rotates the device.

The capsule can then move and orient itself to any interesting spot in the tested digestive organ by moving the external magnet using a 5DOF robotic movable frame.

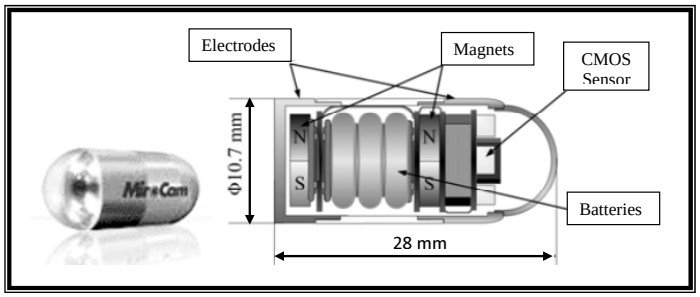

Figure 2.9: Experimental WCE based on MIRO [58].

Experiment tests for the capsule velocity based on single, double, and triple twistable thread modules in an artificial tract were carried out and compared. The practical results showed that the capsule based on the double thread module, the thread pitch angle of 35°, and the external magnet rotated at 24 rpm, could proceed through the colon simulator with a velocity not faster than 300 mm/min.
However, precise movement of the robotic movable frame was not enough to stabilize the implanted magnets in the free space of the investigated organ. To achieve that, the attraction force between the magnets must be controlled based on a closed-loop control system. Moreover, the captured pictures, as mentioned previously, were blurred due to the rotation movement of the capsule.

In 2012, a new magnetic actuation approach was proposed by Yim et al. [59] [60] for a capsule endoscope. They fabricated a prototype of a compliant magnetic capsule robot for medical procedures in the stomach. The device was actuated and oriented magnetically based on a rolling locomotion method. They implanted two permanent magnets in both ends of a dummy capsule made of soft elastomer and used the force and torque of an external permanent magnet connected across a motor and mounted on a movable frame to rotate the capsule. Preliminary tests for the proposed navigation method in the stomach simulator were carried out.
However, the magnetic force of this actuator was not controlled to manipulate the capsule in the free space of the tested organ. Additionally, further investigation of its safety is required before its use in the human body, as the rolling locomotion of the capsule could damage the internal wall of the stomach. Finally, the axial movement of the device could prevent the taking of pictures for some interesting spots in the investigated organ.

A new actuation strategy for a capsule endoscope is proposed by Federico et al [11]. They fabricated prototype magnetic shells made of a silicon rubber mixed with

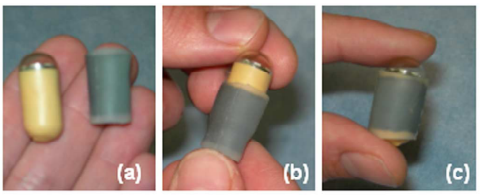

Figure 2.10: (a) Endoscopic capsule and elastic shell. (b) Application of the shell to the capsule. (c) Resulting capsule/shell complex [11].

magnetic particles to cover the central part of the capsule as shown in Fig. 2.10. These elastic shells were adopted to actuate the capsule through their interaction with an external magnetic field which is generated from magnetic cylindrical discs handled by the operator.

Based on the different configurations of the shells, it can achieve different types of capsule motions. Manipulation of the position and orientation of these magnetic sources can control the actuation and rotation of the capsule/shell complex. Preliminary bench tests reported that the use of an external magnetic field could translate and rotate the capsule/shell complex wirelessly within sample tubular structures made of bovine tissue.

However, it is hardly possible to actuate the device along the digestive tract, unless the lateral magnetic actuation force of the system is large enough to overcome the friction force between the capsule and the internal wall of the tested organ. Moreover, the system needs further work to optimise both the shell design and the magnetic field sources to achieve an applicable actuation system.

In 2011, A robotic magnetic navigation scheme (Stereotaxis system) was used by Carpi et al. [61] to robotic steering of a capsule/shell complex based on a M2A capsule camera. In vivo experiments were carried out in the main organs of the digestive tract in a domestic pig model, and the medical device was tracked in real-time using fluoroscopic imaging. However, the magnetic guiding instrumentation should be validated by using it with the next generations of endoscopic capsule schemes.

G. Kosa et al. [18] fabricated a miniature swimming mechanism for a capsule endoscope, using the static (B0) and radio frequency (RF) magnetic field inherently available in a magnetic resonance imaging (MRI) scanner for both capsule movement and wireless energy delivery. The proposed mechanism, as shown in Fig. 2.11 included three waving tails with three coils in each. Propulsion force was generated through passing alternating current in the coils on the static magnetic field of MRI.

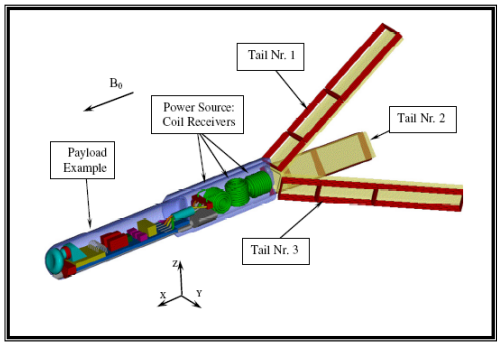

Figure 2.11: Steerable swimming micro robot for the MRI. [18].

The MRI's RF magnetic field was used to power the coils of the swimming tails. The preliminary results showed that the capsule with swimming tails could move based on the MRI's magnetic field. However, this limited experimental study was not performed on a dummy capsule and the proposed mechanism was not validated based on a practical environment. Moreover, the capsule propulsion force was not controllable.

In 2012, Lien et al. [62] proposed a magnetic actuation system to enable surgeons to control the mobility of the endoscopic capsule by means of moving their own hands as previously proposed by [11][61]. They fabricated a new prototype capsule endoscope equipped with shorter and longer focal length lenses for visualization of close-up and far-end stomach wall. A side-magnetized permanent magnet was embedded into the capsule to enable remote locomotion. An external magnetic field navigator (MFN) based on a permanent magnetic rotor with a built-in stepping motor was fabricated to manoeuvre the capsule inside a stomach. Fig. 2.12(a)(b) shows the prototype model of the fabricated endoscopic capsule and the MFN respectively. The ex vivo and in vitro tests were performed to validate the locomotion capabilities of the proposed navigation system using both simulated and resected porcine stomachs. However, the proposed endoscopic capsule was not wireless as it still needed to be connected to power and image data transfer cables. Moreover, further assessment of its safety and controllability is required before its adoption in practice.

2.2 Magnetic Levitation Technique

Magnetic levitation is a powerful technology for noncontact suspension and manipulation of objects using magnetic fields. Generally, the manipulated objects are

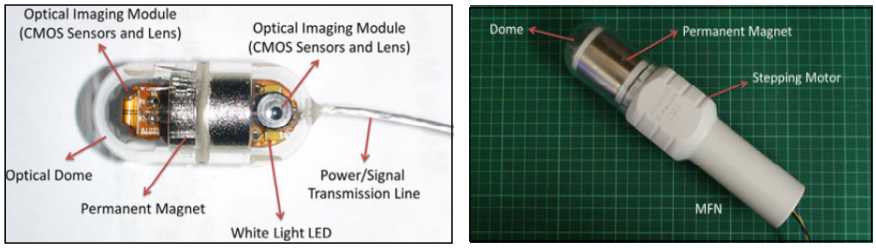

(a) Prototype capsule endoscope (b) Prototype MFN

Figure 2.12: Prototypes of proposed endoscopic capsule and its external MFN [62].

either steel or permanent magnets, in this application a small permanent magnet embedded in the capsule endoscope used a levitated object. Basically, the magnetic suspension scheme are open-loop instable and inherently nonlinear with fast dynamics [63]. According to Earnshaws Theorem [64], it is impossible to achieve a stable and static suspension for permanent magnets in space using only fixed magnetic fields. This means that if the magnetic dipole is to be levitated stably, the external electromagnetic field must be time-variant, and this should be achieved by a closed-loop control system.

The feedback control of the magnetically levitated magnet has received a great deal of interest from many of controller design methods. In this thesis, two control systems named SISO and MIMO are investigated for capsule actuation. A PID controller is adopted for 1D capsule locomotion system due to its ability to effectively regulate the suspension scheme, under the assumption of a well known controller gain parameters [65]. Where as the PP, EEA, and LQR approaches are considered for the 2D capsule control. In the next section, background and theory of these proposed controllers techniques are considered.

2.3 Background of Proposed Navigation System

2.3.1 Controller Techniques

Magnetic levitation systems are inherently unstable and, therefore, applying a control system with feedback is required to achieve the stabilization of the suspending object. The usual purposes of feedback in practice are [66]

1. To optimise or ensure the system stability.

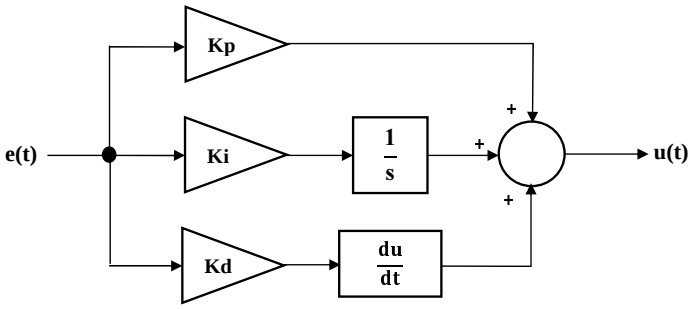

Figure 2.13: Block diagram of PID controller.

2. To decrease the sensitivity of the control scheme to modelling errors.

3. To support the system's ability to reject disturbances and to attenuate noise of the system hardware components.

4. To change the transient response of the scheme.

In this section, controller techniques for SISO and MIMO systems are presented for the problem of control.

2.3.1.1 1D Controller technique

A PID is the most popular and commonly used industrial controller due to its simplicity and performance characteristics [67]. This technique is simple to realize for SISO schemes since the control parameters are relatively independent. Fig. 2.13 shows the structure of the PID controller, in block diagram, as given by:

$$u(t) = K_p e(t) + K_i \int_0^t e(\tau)d\tau + K_d \frac{de(t)}{dt} \tag{2.1}$$

Basically, a PID controller generates an output control signal u(t) based on the controlled error signal e(t) between the desired input and actual system output. The control signal is calculated by involving three separate parameters: the proportional gain K_p, the integral gain K_i, and the derivative gain K_d. It is accordingly also called three-term control: the proportional (P), the integral (I), and the derivative (D) values. P depends on the current error value, I on the accumulation of past errors, and D is a prediction of future errors. The controller attempts to minimize the error by regulating its gain parameters. The response of the controller is evaluated based on the response error, the level to which the controller overshoots the reference input

and the degree of system oscillation. The influence of the PID controller terms on the response of the closed-loop control system can be clarified as follows:

- **Proportional term**. It produces a control action that is directly proportional to the present error value. The expression of the proportional output is given by:

$$P_{out} = K_p e(t) \tag{2.2}$$

  The system can become unstable, if the proportional part is too high. In contrast, the control action of the system based on too low proportional gain may be too small when responding to scheme disturbances.

- **Integral term**. This is proportional to both the duration and magnitude of the error, and can be expressed by multiplying the integral gain K_i by the accumulated error, which is the sum of the instantaneous error over time, as follows:

$$I_{out} = K_i \int_0^t e(\tau) d\tau \tag{2.3}$$

  The integral part accelerates the movement of the process towards the desired input and eliminates the residual steady state error that occurs with a pure proportional controller. However, since the integral part responds to accumulated errors from the past, it can cause the present value to overshoot the demand value.

- **Derivation term**. This is termed by multiplying the error gradient time by derivation gain K_d, and it can be expressed as follows:

$$D_{out} = K_d \frac{de(t)}{dt} \tag{2.4}$$

  Derivative control is used to reduce the overshoot level produced by the integral component and improve the combined controller-process stability. However, the derivative term slows the transient response of the controller. Also, differentiation of a signal amplifies noise and thus this controller part is highly sensitive to noise in the error term, and can cause a process to become unstable if the noise and the derivative gain are sufficiently large.

Finally, in most control applications, proper tuning of the gains K_p, K_i, and K_d in the controller algorithm, can enable the controller to provide control action designed for specific performance. Therefore, this technique can be adopted to implement our 1D capsule actuation system.

Based on the root locus controller design method, the time domain specifications of the control system, which include rise time t_r, overshoot M_p, and settling time t_s, are used to determine the damping factor ζ and the natural frequency of the controller ω_n as follows:

$$\zeta = \frac{\log_e (0.01 M_p)}{\sqrt{\pi^2 + \log_e (0.01 M_p)^2}} \tag{2.5}$$

$$\omega_n = \frac{4}{t_s \zeta} \tag{2.6}$$

Using on (2.5) and (2.6), a pair of complex dominant poles for the closed-loop control system is calculated as follows:

$$s_{1,2} = -\zeta \omega_n \pm j \omega_n \sqrt{1 - \zeta^2} \tag{2.7}$$

Based on the desired time response of the control system t_s and M_p, the closed-loop poles are assigned and are then used to determine the controller gains required to stabilise the system [68] [69].

2.3.1.2 2D Controller techniques

For multi-variable systems, i.e. systems with MIMO, the design of multi-degree of freedom (MDOF) controllers requires the formulation of the systems in state space form. In this research project, three methods are adopted to implement the controller of the MIMO system: entire eigenstructure assignment (EEA), pole placement (PP), and linear quadratic regulator (LQR).

EEA Method

The EEA controller approach depends on the assignment of the closed-loop eigen values and their associated eigenvectors which have an influence on the time response of scheme. In the MIMO case, there are an infinite number of feedback matrices that can assign a specific set of closed-loop eigenstructures. The controller can be applied successfully to the synthesis for both MIMO regulators and tracking systems; applying this approach in tracking systems requires the number of outputs

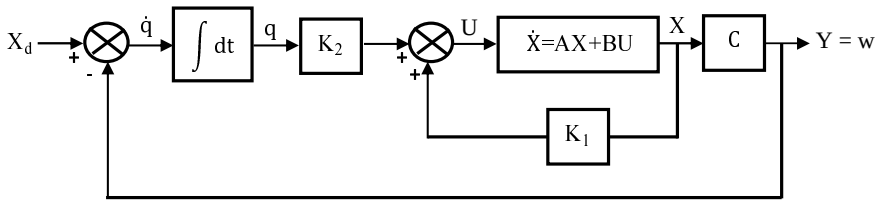

Figure 2.14: Block diagram of the control system based on EEA technique.

that can be attracted to be less than the number of control inputs [70].
For a controllable open-loop time-invariant (TI) MIMO system presented by the following plant state and output equations:

$$\dot{X}(t) = AX(t) + BU(t), \tag{2.8}$$

$$Y(t) = CX(t) + DU(t), \tag{2.9}$$

the control law

$$U(t) = \bar{K}\tilde{X}, \tag{2.10}$$

where $\bar{K} = [K_1\ K_2]$ is the gain matrix and $\tilde{X} = [X\ q]^T$ is the composite state vector of the open-loop system, is applied to the plant in order to assign its both closed-loop eigenvalues spectrum

$$\sigma\left(\bar{A_{cl}}\right) = \{\lambda_1, \lambda_2, \lambda_3.....\lambda_{n+p}\} \tag{2.11}$$

and an associated set of eigenvectors [70]

$$v\left(\bar{A_{cl}}\right) = \{v_1, v_2, v_3.....v_{n+p}\} \tag{2.12}$$

$$\bar{A_{cl}} = \bar{A} + \bar{B}\bar{K} \tag{2.13}$$

where $\bar{A_{cl}}$ is the closed-loop plant matrix, $\bar{A} = \begin{bmatrix} A & 0 \\ -C & 0 \end{bmatrix}$, $\bar{B} = \begin{bmatrix} B \\ 0 \end{bmatrix}$. Based on (2.10), the above equation can be rewritten as:

$$\bar{A_{cl}} = \begin{bmatrix} A + BK_1 & BK_2 \\ -C & 0 \end{bmatrix}. \tag{2.14}$$

The closed-loop eigenvalues and associated eigenvectors of the feedback tracking system can be seen as a block diagram in Fig. 2.14. These are related by:

$$(\bar{A_{cl}})v_i = \lambda_i v_i, \quad i = 1, 2, .., n \tag{2.15}$$

If we define

$$\psi_i = \bar{K} v_i, \quad for\ i = 1, 2, .., n \tag{2.16}$$

Then (2.15) can be written as follows:

$$S(\lambda_i) \begin{bmatrix} v_i \\ \psi_i \end{bmatrix} = 0, \quad i = 1, 2, .., n \tag{2.17}$$

where $S(\lambda_i) = \begin{bmatrix} (\bar{A} - \lambda_i I) & \bar{B} \end{bmatrix}$ is an n x $(n + m)$ matrix, for the above quality to hold, the following is required:

$$\begin{bmatrix} v_i \\ \psi_i \end{bmatrix} \in kerS(\lambda_i), \quad i = 1, 2, .., n \tag{2.18}$$

where $kerS(\lambda_i)$ denotes the Kernel or null-spaces in the $S(\lambda_i)$ which must be occupied by the vectors $[v_i \quad \psi_i]^T$. Using (2.16) for every $i = 1, 2, .., n$, we obtain the following form of the state feedback gain-matrix:

$$\bar{K} = \Psi_i V_i^{-1}, \quad i = 1, 2, .., n \tag{2.19}$$

where $\Psi = \begin{bmatrix} \psi_1, \psi_2, ..., \psi_n \end{bmatrix}$ and $V = \begin{bmatrix} v_1, v_2, ..., v_n \end{bmatrix}$. As indicated in the above equation, V must be invertible. This is in general possible when the desired closed-loop eigenvalues spectrum contains no eigenvalues of the open-loop matrix A. If the desired eigenvalue set is specified and the associated eigenvectors are selected to satisfy (2.17), then an optimal gain-matrix $\bar{K}$ is determined from (2.19).

pole placement Method

It is well known that in order to change the characteristics of a plant, a closed-loop control system based on a controller technique must be applied. Changing efficiency depends on the type and robustness of the controller used. For a completely state controllable system, the full state feedback gain matrix based on the PP technique

is designed to provide sufficient number of controller design parameters in order to move all the arbitrary closed-loop poles independently of each other and place them at desired locations [71].

- **Algorithm**. Consider a completely state controllable system with a state and output equations (2.8) and (2.9), the state feedback supplied for regulation design is given as:

$$U(t) = -KX(t), \tag{2.20}$$

where K is state feedback gain matrix. The closed-loop state equation can be obtained by substituting (2.20) into (2.8)

$$\dot{X}(t) = (A - BK)X(t). \tag{2.21}$$

This state equation expresses the scheme composed by merging the plant with the controller. It is a homogeneous equation without input, and its solution is given by:

$$X(t) = e^{(A-BK)X(t)}X(0), \tag{2.22}$$

where $X(0)$ is the initial state vector caused by external disturbances. The control input $U(t)$ drives the system states to zero for arbitrary initial conditions. The eigenvalues of closed-loop plant matrix $(A - BK)$, which are also called the regulator poles, are used to make the system stable and satisfy its transient response characteristics. If the regulator gain matrix K is chosen properly, then it can be made as an asymptotically stable matrix, and for all $X(0) \neq 0$ it is possible to make the state vector $X(t)$ approaches 0 as t approaches infinity.

A gain matrix K that yields the closed-loop poles (p_1, p_2, p_n) can be obtained by solving the equation [72]:

$$det\ (sI - A + BK) = (s - p1)(s - p2).....(s - p_n). \tag{2.23}$$

For tracking MIMO systems, the control law applied is given by:

$$U(t) = K(X_d(t) - X(t)) - K_d X_d(t), \tag{2.24}$$

where K_d is a state forward gain matrix and $X_d(t)$ is the desired state vector. If $X_d(t)$ is linear and time-invariant, then it can represented by the following state equation:

$$\dot{X}_d(t) = A_d X_d(t), \tag{2.25}$$

where A_d is state dynamic matrix (nxn). The error of tracking system is given by:

$$e(t) = X_d(t) - X(t) \tag{2.26}$$

Subtracting (2.8) from (2.25) and substituting (2.24) yields the following plant state equation in terms of the tracking error:

$$\dot{e}(t) = (A - BK)e(t) + (A_d - A + BK_d)X_d(t) \tag{2.27}$$

The feedback gain matrix K is calculated by solving (2.23), while forward gain matrix K_d, which is used to reduce the tracking error to zero, is determined based on (2.27) as follows:

$$K_d = B^{-1}(A - A_d) \tag{2.28}$$

- **Eigenvalues selection**. The system can achieve different performances based on different closed-loop system pole locations. Based on the desired response the suitable scheme eigenvalues are assigned.

linear quadratic regulator method

The optimal control method LQR is another technique for MIMO control system. The idea behind the approach is to transfer the designers iteration on pole locations as used in the full state feedback method to iterations on the elements in a cost function J. This method determines the gain that minimizes the objective function J in order to achieve some compromise between the use of control effort and the plant characteristics that will guarantee a stable system [73].

- **Algorithm**. Suppose that a system is defined by:

$$\dot{X}(t) = AX(t) + BU(t) \tag{2.29}$$

This approach involves applying the input vector [71]

$$U(t) = Ke(t) - K_d X_d(t), \tag{2.30}$$

where K and K_d are the optimal feedback and non-optimal forward gain matrices respectively, in order to track the input commands while minimizing the following LQR quadratic cost function:

$$J = \int_0^\infty \left[e^T(t)Q_c(t)e(t) + U^T(t)R(t)U(t)\right] d(t) \tag{2.31}$$

where $Q(t)$ and $R(t)$ are the state and control weighting matrices respectively which are square and symmetric. Typically, in linear control theory [74], the feedback gain matrix K is given by:

$$K = R^{-1}B^T P, \tag{2.32}$$

where P is a unique, positive semi-definite solution to the continuous Riccati equation given by:

$$A^T P + PA - PBR^{-1}B^T P + Q = 0. \tag{2.33}$$

While K_d can be calculated by solving the following equation [71]:

$$BK_d X_d(t) = AX_d(t) \tag{2.34}$$

- **Weight matrix selection**. In the LQR design method, the weight matrices Q(t) and R(t) are set such that the closed-loop system can achieve the desired performance which include system stability based on reasonable control effort. The LQR controller is an iterative bound because the parameters of the weighting LQR matrices are determined by trial and error [75][76]. The selection of these gain matrices is weakly connected to the performance specifications of the scheme, and therefore, a certain amount of trial and error is required with an interactive computer simulation before satisfactory design results are seen.

2.4 Chapter Summary

The design of a safe and reliable navigation scheme for the WCE is a very significant step to activate its role in evaluation of the digestive tract. For decades, a number of researchers have used different techniques to design many actuation systems for the endoscopic capsule. In this chapter, the literature review of several internal navigation schemes based on different locomotive mechanisms and external actuation systems for the capsule endoscope have been presented. The actuation performance of these systems was also analysed based on controllability, moving speed, size, and power consumption parameters. However, the active mobility of a medical device is still in the developmental stages and a reliable endoscopic capsule model is not available commercially yet. In this chapter, background and theory of the SISO and MIMO proposed controller techniques were also discussed.

Chapter 3

Theory and Analysis of Magnetic Actuation

This chapter provides a general derivation of the mathematical expression for magnetic field density in the 3D (x,y and z) produced by a magnetic dipole (electromagnetic coil, permanent magnet). Coil geometry (core width and height) and its electrical parameters (current, number of windings, core permeability) are considered in optimisation of actuator structure design. The magnetic field produced by coils with different physical dimensions and electrical parameters is assessed based on the strength and uniformity of the field along local axis criteria.

This chapter also focuses on the mathematical analysis of the magnetic force and torque exerted by the external magnetic source on the embedded magnet in the capsule. The magnetic force formula has been stated in the Cartesian coordinate system. In the xz-plane, for distances bigger than the characteristics length of the coil, magnetic force and torque formulas are expressed in a spherical coordinate system. This is also done for the purpose of the simplicity of the capsule orientation expression.

Finally, the proposed actuator was designed using Comsol software (COMSOL Multiphysics 3.4 version) through optimising the physical dimensions and electrical parameters of the proposed coil, such that it can maximise the levitation distance to a realistic value for colon examination.

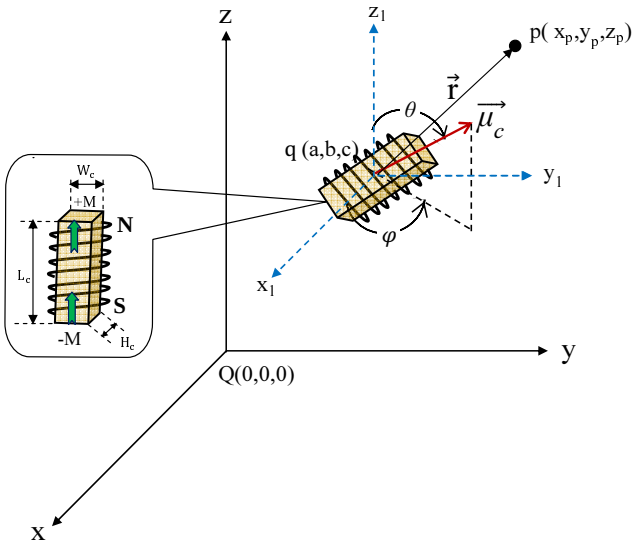

Figure 3.1: Position and orientation relations between the coil and test point.

3.1 Magnetic Field Modelling and Analysis

3.1.1 Mathematical Model of Magnetic Field Density

The proposed magnetic actuation system depends on the magnetic interaction between electromagnetic coil and embedded magnet in the capsule. In order to activate this interaction and apply a stable control system, the actuation magnetic field should be analysed.

This chapter concerns mathematical modelling for the magnetic field of the actuator and the embedded magnet. As there is no fundamental difference between the fields generated by permanent magnets and the fields generated by currents flowing around conventional electric circuits, and because the expected distance between the actuator and the manipulation region of the magnet is bigger than the biggest dimension of the coil, we can consider the magnetic source to be a magnetic dipole [77][78].

Assume a rectangular iron-cored coil with length L_c, width W_c, and height H_c positioned based on the global Cartesian coordinate system (x, y, z) at the point $q\,(a, b, c)^T$ as shown in Fig. 3.1. Magnetism pair $+M$ and $-M$ of the coil are governed by the direction of its current flow. Let $\vec{r}$ be the vector from the center of the coil to a spatial point $textp(x_p, y_p, z_p)^T$ which can be represented as follows:

$$\vec{r} = (x_p - a)i + (y_p - b)j + (z_p - c)k \tag{3.1}$$

The magnetic moment vector of the coil is given:

$$\vec{\mu_c} = \mu_c \hat{\mu}_c, \tag{3.2}$$

where $\mu_c = NIA_c$ is the magnetic moment value of the solenoid (Am^2), N, I and A_c are the number of turns, current (A) and the cross-sectional area of the coil (m^2) respectively, and $\hat{\mu_c}$ is the normalized vector representing the direction of the coil's magnetism which is defined as the direction from negative $-M$ to the positive $+M$ magnetism of the solenoid. As shown in Fig. 3.1, the orientation of the magnetic dipole moment is represented by two angles: the inclination angle (θ) and the azimuth angle (ϕ). which can be expressed by the following equation:

$$\hat{\mu_c} = mi + nj + pk, \tag{3.3}$$

where m, n, and p are the projections of the dipole direction on the x, y, and z-axis respectively, $m = \sin(\theta)\cos(\phi)$, $n = \sin(\theta)\sin(\phi)$, and $p = \cos(\theta)$. Generally, the vector magnetic field $\vec{B}$ based on air-cored coil at the spatial point p is given by [79]:

$$\vec{B} = -\frac{\mu_o}{4\pi} \nabla \left(\frac{\vec{\mu_c} \cdot \vec{r}}{r^3} \right), \tag{3.4}$$

where μ_o is the air magnetic permeability (Tm/A) and r is the length of the vector $\vec{r}$ (m). For the solenoid that has an iron core with a relative permeability of μ_r, the generated magnetic field can be expressed by (3.4) after replacing μ_o by $\mu_o \mu_r$. However, this formula is only valid within the iron core area and its surrounding space if it has the same permeability. If the solenoid is in free air the return path for the magnetic flux is through the relatively low permeability of the air medium and hence high reluctance reduces the effectiveness of the coil core, and consequently, the strength of the magnetic field around the coil. Instead, a numerical analysis based on finite element method (FEM) would probably be required to calculate the magnetic field anywhere around the coil [80].

For a specific operation region, the permeability of the coil in this research project is multiplied by an attenuation factor called $\Re$, whose value depends on the distance between the actuator and the region of interest. This factor is used to define another factor called the magnetic field strength factor $\mu_r \Re$, which is incorporated in the magnetic field expressions of the coil.

Expanding the gradient of the product of the two scalar functions $(\vec{\mu_c} \cdot \vec{r})$ and $\left(\frac{1}{r^3}\right)$ in (3.4) for iron-cored coil yields:

$$\vec{B} = -\frac{\mu_o \mu_r \Re}{4\pi} \frac{1}{r^3} \nabla \left(\vec{\mu_c} \cdot \vec{r}\right) - \frac{\mu_o \mu_r \Re}{4\pi} \left(\vec{\mu_c} \cdot \vec{r}\right) \nabla \left(\frac{1}{r^3}\right) \tag{3.5}$$

Because $\nabla \left(\vec{\mu_c} \cdot \vec{r}\right) = \vec{\mu_c}$ and $\nabla \left(\frac{1}{r^3}\right) = -\frac{3\vec{r}}{r^5}$, the magnetic field density around the coil is expressed by equation (3.6)

$$\vec{B} = \frac{\mu_o \mu_r \Re}{4\pi} \left(\frac{3 \left(\vec{\mu_c} \cdot \vec{r}\right) \vec{r}}{r^5} - \frac{\vec{\mu_c}}{r^3} \right) \tag{3.6}$$

Based on (3.2), the above equation can be rewritten in the following form:

$$\vec{B} = B_T \left(\frac{3 \left(\hat{\mu_c} \cdot \vec{r}\right) \vec{r}}{r^5} - \frac{\hat{\mu_c}}{r^3} \right), \tag{3.7}$$

where $B_T = \frac{\mu_o \mu_r \mu_c \Re}{4\pi}$, and $r = \mid \vec{r} \mid = \sqrt{(x_p - a)^2 + (y_p - b)^2 + (z_p - c)^2}$.

By substituting (3.3) into (3.7) and expanding (3.7), we can express the three components of the magnetic field in Tesla with the following equation:

$$\begin{aligned} B_x &= \frac{B_T}{r^5} \left(m \left(2X^2 - Y^2 - Z^2\right) + 3nXY + 3pXZ \right) \\ B_y &= \frac{B_T}{r^5} \left(n \left(2Y^2 - X^2 - Z^2\right) + 3mXY + 3pYZ \right) \\ B_z &= \frac{B_T}{r^5} \left(p \left(2Z^2 - X^2 - Y^2\right) + 3mXZ + 3nYZ \right), \end{aligned} \tag{3.8}$$

where $X = x_p - a$, $Y = y_p - b$, and $Z = z_p - c$. It is clear from the above equation that the magnetic field is linearly proportional to the number of turns, current, and cross-section area, and the iron core permeability of the coil, and is inversely proportional to the fifth-order of the distance of the test region.

Based on the above equation, the transverse component in the xy-plane is given by:

$$B_{xy} = \sqrt{B_x^2 + B_y^2} \tag{3.9}$$

The resultant and orientation of the magnetic field density created by the electromagnetic coil can be expressed by the following equations.

$$B = \sqrt{B_x^2 + B_y^2 + B_z^2} \tag{3.10}$$

$$\begin{aligned} \phi &= \arctan \frac{B_y}{B_x} \\ \theta &= \arctan \frac{B_{xy}}{B_z}, \end{aligned} \tag{3.11}$$

where θ and ϕ are azimuth and inclination angles of the magnetic field density.
If the coil is placed at the origin of the global coordinate system and oriented to the positive z-axis, i.e. $(a, b, c) = (0, 0, 0)$, and the coil's rotation angles $\theta = 0°$ and $\phi = 0°$, then based on (3.8) the magnetic field density components at the spatial point $p(x_p, y_p, z_p)$ become as follows:

$$\begin{aligned} B_x &= B_T \frac{3x_p z_p}{\left(x_p^2 + y_p^2 + z_p^2\right)^{\frac{5}{2}}} \\ B_y &= B_T \frac{3y_p z_p}{\left(x_p^2 + y_p^2 + z_p^2\right)^{\frac{5}{2}}} \\ B_z &= B_T \frac{\left(2z_p^2 - x_p^2 - y_p^2\right)}{\left(x_p^2 + y_p^2 + z_p^2\right)^{\frac{5}{2}}} \end{aligned} \tag{3.12}$$

Based on [81], if a cylindrical coil with a radius r_c and a length L_c placed at a region so that $r < 2L_c$, i.e. the test point $p(x_p, y_p, z_p)$ is close to the coil, the generated magnetic field density is governed by the following equations.

$$\begin{aligned} B_x &= \frac{3B_T X}{2r^3} \left[\frac{Z - \frac{L_c}{2}}{\left(1 + D - \frac{L_c}{r^2} Z\right)^{\frac{5}{2}}} + \frac{Z + \frac{L_c}{2}}{\left(1 + D + \frac{L_c}{r^2} Z\right)^{\frac{5}{2}}} \right] \\ B_y &= \frac{3B_T Y}{2r^3} \left[\frac{Z - \frac{L_c}{2}}{\left(1 + D - \frac{L_c}{r^2} Z\right)^{\frac{5}{2}}} + \frac{Z + \frac{L_c}{2}}{\left(1 + D + \frac{L_c}{r^2} Z\right)^{\frac{5}{2}}} \right] \\ B_z &= \frac{B_T}{r^3} \left[\frac{1 + D - \frac{L_c}{r^2} Z - E}{\left(1 + D - \frac{L_c}{r^2} Z\right)^{\frac{5}{2}}} + \frac{1 + D + \frac{L_c}{r^2} Z - E}{\left(1 + D + \frac{L_c}{r^2} Z\right)^{\frac{5}{2}}} \right] \end{aligned} \tag{3.13}$$

Table 3.1: Parameters of the electromagnetic coil.

Parameter	Value
L_c	80 mm
W_c	25 mm
H_c	25 mm
N	180
D_w	1 mm
I	5 A
$\mu_r\Re$	3
μ_0	$4\pi 10^{-}7\,(T\ m/A)$

where $D = \frac{L_c^2+r_c^2}{r^2}$, and $E = \frac{3}{2}\frac{X^2+Y^2}{r^2}$. To validate using the expression (3.13) for our rectangular actuator, the factor r_c should be substituted by the term $\sqrt{\frac{W_c H_c}{\pi}}$.
The design of the electromagnetic coil and the determination of its drive current are the main concerns of the proposed magnetic actuation system. The actuator should be designed so that its magnetic field is applied to the embedded magnet as strongly and uniformly as possible while keeping the excitation current within an acceptable range. For this, an analysis of the magnetic field distribution based on the physical and electrical coil parameters is considered in the next section.

3.1.2 Magnetic Field Analysis

In the design of any magnetic levitation system, the distribution of the magnetic field around an actuator should be analysed in order to activate magnetic interaction between the magnetic field source and actuated object. In order to validate the analysis for the coil's magnetic field, realistic values of the associated parameters should be considered. Because the actuator is placed outside the human body, the manipulation distance relative to the coil should be chosen according to the empirical value of the human body size. Moreover, the coil current should not exceed a certain value at which the core material reaches magnetic saturation (its calculation is given in Chapter 4).

Assume an iron-cored coil with parameters as listed in Table (3.1) is placed at the origin of the global coordinate system and oriented to the positive z-axis, i.e. $q(a, b, c) = q(0, 0, 0)$, $\theta = 0°$, and $\phi = 0°$, where D_w is the diameter of the coil's winding wire (m). Based on (3.12), the 3D distribution of the magnetic field within

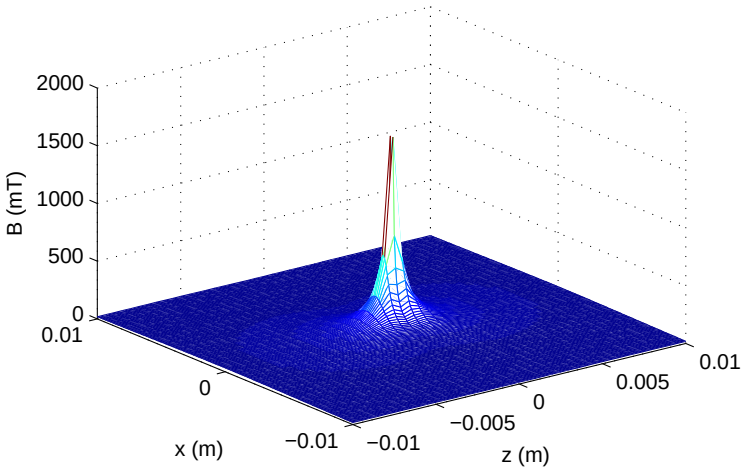

Figure 3.2: 3D magnetic field distribution at region far away of the coil.

the xz-plane at a region around the coil with a current of 5 A, as shown in Fig. 3.2. It should be noted that the magnetic field density has been distributed uniformly across the test region.

For more specific evaluation, based on the same conditions, Fig. 3.3(a), (b), and (c) shows distribution of the magnetic field components B_x, B_y, and B_z at vaild distance z=160 mm in the xz-plane respectively, while the resultant magnetic field and its orientation are illustrated in Fig. 3.3(d), and (e) respectively.
It can be noted from Fig. 3.3(d) and (e) that at the coil axis region, the magnetic field reaches a maximum value with a gradient of zero. In this region, the suspended magnet can be stabilized if a proper controller system is applied.

Fig. 3.4 shows the 3D variation of the magnetic field based on (3.13) at distance close to a cylindrical coil with the following assumptions: the position is at $q(0, 0, 0)$, the orientation is to the positive z-axis, and the physical and electrical parameters are listed in Table (3.2). It is clear from Fig. 3.4 that the coil could generate a smooth and symmetric magnetic field around its axis.

To validate an approximation field expression (3.12), which is used for far field analysis, the magnetic field at $z = 16$ mm in the xz-plane is also analysed using the exact equation (3.13), as shown in Fig. 3.5, and then compared with the analysis shown in Fig. 3.3. The comparison reveals that there is a good match between the two analyses and, consequently, it can be said that the approximation formula (3.12) can be adopted to model the magnetic field variation theoretically at a far away region with efficiency increasing with distance.

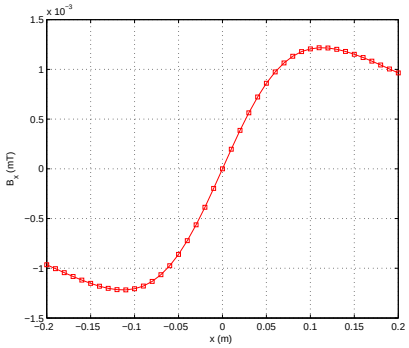

(a) B_x component.

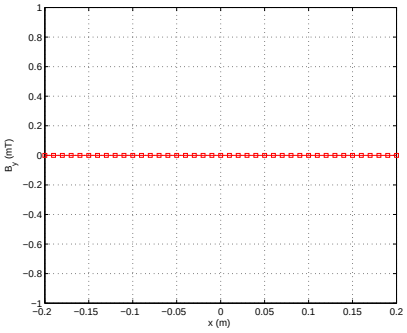

(b) B_y component.

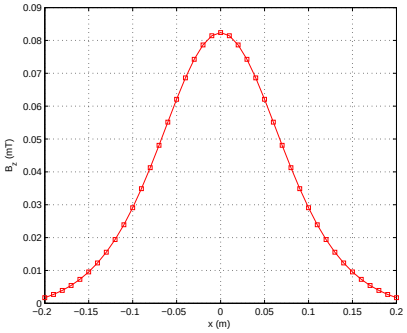

(c) B_z component.

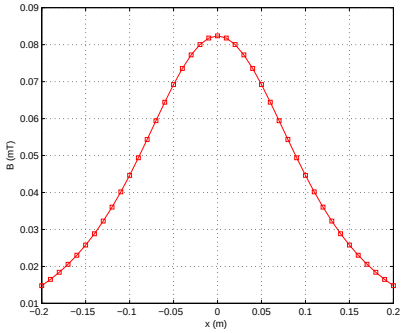

(d) Magnetic field.

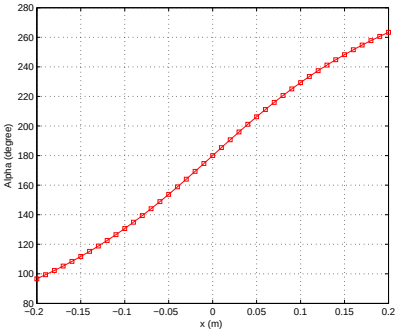

(e) Magnetic field angle.

Figure 3.3: Magnetic field components and angle.

It is worth considering that the exact formula (3.13) is not a precise mathematical expression for magnetic field modelling as it does not take the thickness of the coil windings factor into consideration.

Table 3.2: Parameters of the cylindrical electromagnetic coil.

Parameter	Value
L_c	30 mm
r_c	12.5 mm
N	180
D_w	1 mm
I	5 A
$\mu_r \Re$	3

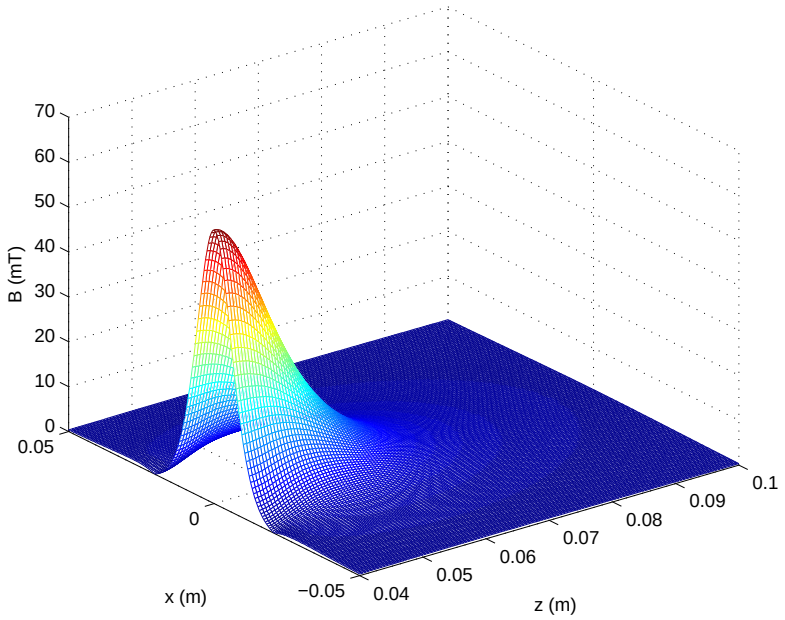

Figure 3.4: 3D magnetic field distribution at region closed to the coil.

3.2 Magnetic Force and Torque Analysis

The permanent magnet, which was modelled as a magnetic dipole in the previous section, is enclosed in the capsule endoscope not only for localization purposes, but also so that it can be moved and oriented by the magnetic force and torque of an external magnetic field. The force $\vec{F}(p)$ exerted on a small permanent magnet with a magnetic moment $\vec{\mu}_m$ placed in a magnetic field $\vec{B}(p)$ at position p, can be derived from potential energy considerations as follows [79]:

$$\vec{F}(p) = \nabla \left(\vec{B}(p) \cdot \vec{\mu}_m \right), \tag{3.14}$$

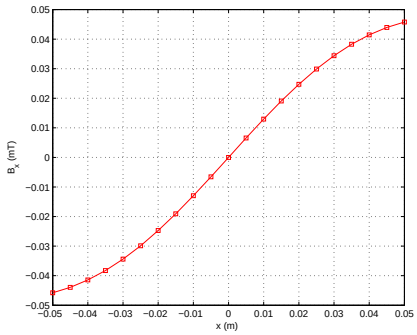

(a) B_x component.

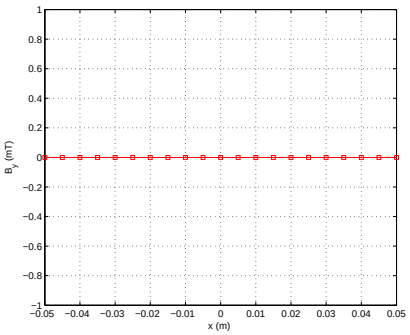

(b) B_y component.

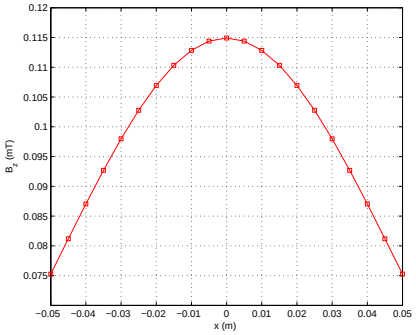

(c) B_z component.

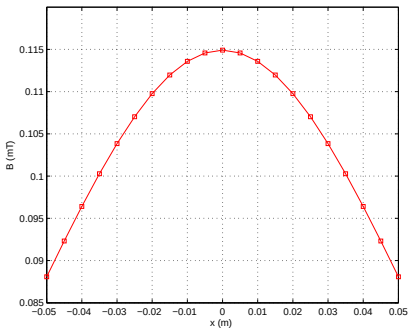

(d) Magnetic field.

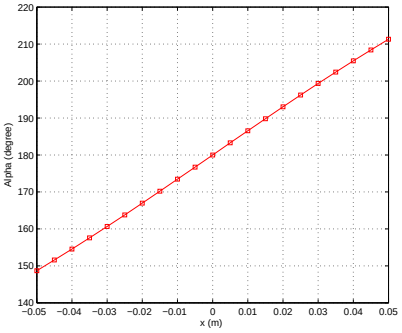

(e) Magnetic field angle.

Figure 3.5: Magnetic field components and angle based on (3.12).

and the torque measured in (Nm) is

$$\vec{T}(p) = \vec{\mu}_m \times \vec{B}(p), \tag{3.15}$$

that is, the magnetic torque tries to orient the embedded magnet along the applied magnetic field density. The magnetic moment of the permanent magnet is:

$$\vec{\mu}_m = \mu_m \hat{\mu}_m, \tag{3.16}$$

where $\mu_m = \frac{B_i V}{\mu_o}$ is the magnetic moment value ($A\ m^2$) of the magnet, B_i and V are magnetic strength (T) and the volume (m^3) of the magnet respectively and $\hat{\mu}_m$ is the magnetic moment direction of the dipole.
Using (3.4), (3.14) can be rewritten as follows:

$$\vec{F} = -\frac{\mu_o \mu_r}{4\pi} \nabla \left(\left(\nabla \frac{\vec{\mu_c} \cdot \vec{r}}{r^3} \right) \cdot \vec{\mu_m} \right). \tag{3.17}$$

In the Cartesian coordinate system, define

$$\vec{\mu}_m = \left(\mu_{mx}, \mu_{my}, \mu_{mz}\right)^T, \tag{3.18}$$

and

$$\vec{F} = \left(F_x, F_y, F_z\right)^T, \tag{3.19}$$

while the position p and magnetic field B are defined as mentioned earlier as $(x_p, y_p, z_p)^T$ and $(B_x, B_y, B_z)^T$ respectively. Then, (3.14) can be rewritten as [51]:

$$\begin{bmatrix} F_x \\ F_y \\ F_z \end{bmatrix} = \begin{bmatrix} \mu_m \frac{\partial B}{\partial x} \\ \mu_m \frac{\partial B}{\partial y} \\ \mu_m \frac{\partial B}{\partial z} \end{bmatrix}, \tag{3.20}$$

That is, the magnetic force is proportional to the directional gradient of the applied magnetic field density. After the gradient and then the simplification path of (3.17), the final magnetic force exerted by the coil on the inserted magnet becomes [79] [82]:

$$\vec{F} = \frac{3\mu_0 \mu_r}{4\pi} \left\{ \frac{(\vec{\mu_c}.\vec{r})\vec{\mu_m} + (\vec{\mu_m}.\vec{r})\vec{\mu_c} + (\vec{\mu_c}.\vec{\mu_m})\vec{r}}{r^5} - \frac{5(\vec{\mu_c}.\vec{r})(\vec{\mu_m}.\vec{r})\vec{r}}{r^7} \right\} \tag{3.21}$$

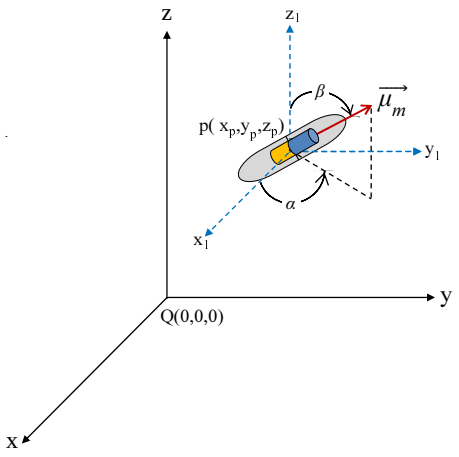

Figure 3.6: Orientation definition of the magnet in spherical coordinate system.

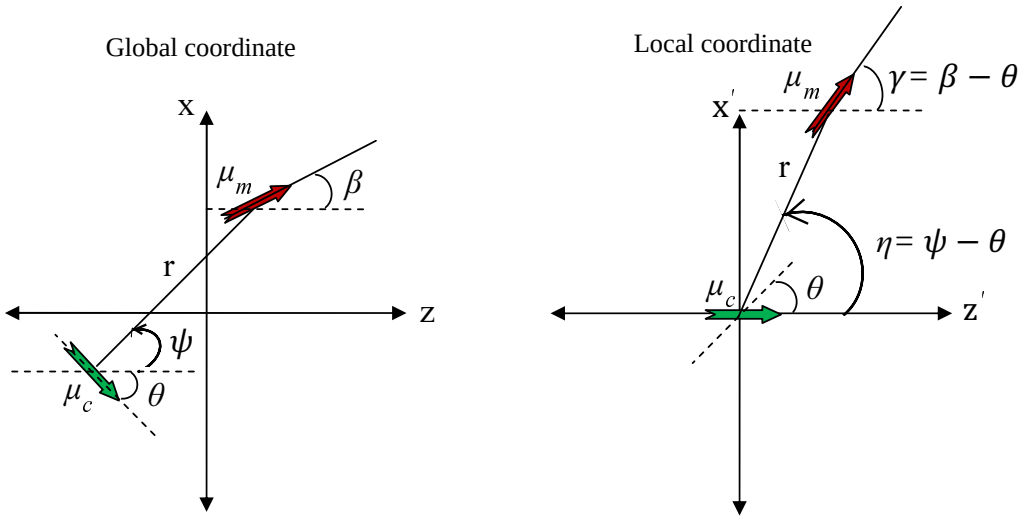

Figure 3.7: Global and local coordinate system for magnetic force between the coil and magnet.

3.2.1 Magnetic Force in a Spherical Coordinate System

In a spherical coordinate system, the magnetic moment orientation of the magnet placed at $p(x_p, y_p, z_p)$, as shown in Fig. 3.6, can be defined as follows:

$$\hat{\mu_m} = si + tj + uk, \tag{3.22}$$

where $s = \sin(\beta)\cos(\alpha)$, $t = \sin(\beta)\sin(\alpha)$, and $u = \cos(\beta)$ are the projections of the magnet direction on the three axes of the coordinate system x, y,and z respectively, β and α are the inclination and azimuth angles of the magnet's moment.

Assume a coil and magnet with azimuth angles $\phi = 0°$ and $\alpha = 0°$ respectively, placed in the xz-plane with local coordinates as shown in Fig. 3.7. If r is bigger than the characteristic distance of the coil, then its magnetic field components in the $\acute{x}$

and $\acute{z}$-direction in the local coordinate system, as previously expressed in (3.12), can be rewritten as follows [83] (its detail is presented in appendix A.1):

$$B_{\acute{x}} = \frac{\mu_o \mu_r \mu_c}{4\pi} \left(\frac{3\cos(\eta)\sin(\eta)}{r^3} \right),$$
$$B_{\acute{z}} = \frac{\mu_o \mu_r \mu_c}{4\pi} \left(\frac{3\cos(\eta)^2 - 1}{r^3} \right), \tag{3.23}$$

where $B_{\acute{x}}$ and $B_{\acute{z}}$ are the axial and radial magnetic field components respectively and η is the angle between the coil moment axis and the position vector of the inserted dipole (radians). Based on (3.23), the magnetic force expression (3.21) can be rewritten in the spherical coordinate system as follows:

$$F_r = -\frac{3\mu_0 \mu_r \mu_c \mu_m}{4\pi r^4} \left[2\cos(\psi - \theta)\cos(\psi - \beta) - \sin(\psi - \theta)\sin(\psi - \beta) \right], \tag{3.24}$$

$$F_\psi = -\frac{3\mu_0 \mu_r \mu_c \mu_m}{4\pi r^4} \sin(2\psi - \theta - \beta), \tag{3.25}$$

where F_r and F_ψ are the magnetic force components in the position vector direction and its radial direction respectively, ψ is the angle between the reference axis of the coil, and the position vector of the embedded magnet, and γ is the angle between the directions of the coil and magnet moments.

Using (3.24) and (3.25), the magnetic force components in the Cartesian coordinate system applied by the solenoid coil on the embedded magnet are given by:

$$F_z = F_r \cos(\psi) + F_\psi \cos\left(\psi + \frac{\pi}{2}\right), \tag{3.26}$$

and

$$F_x = F_r \sin(\psi) + F_\psi \sin\left(\psi + \frac{\pi}{2}\right) \tag{3.27}$$

Based on (3.26) and (3.27); the amplitude and inclination angle of the magnetic force in the xz-plane can be expressed as follows:

$$F = \sqrt{{F_x}^2 + {F_z}^2}, \tag{3.28}$$

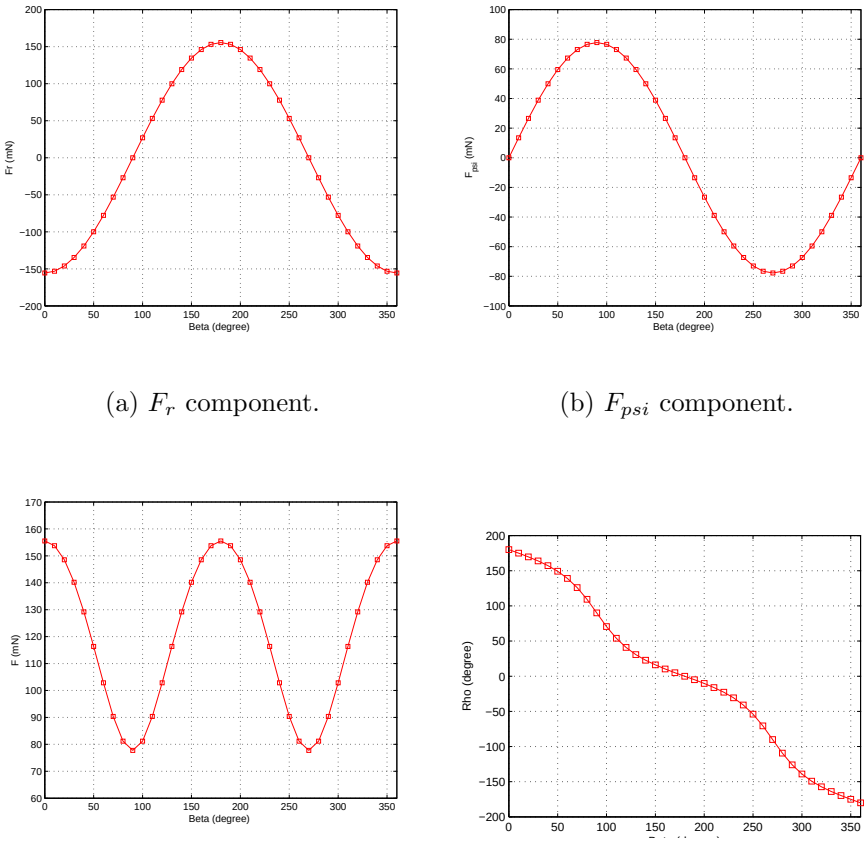

(a) F_r component.

(b) F_{psi} component.

(c) Magnetic force.

(d) Magnetic force angle.

Figure 3.8: Magnetic force components and angle with fixed dipole position.

$$\rho = \arctan\left(\frac{F_x}{F_z}\right), \tag{3.29}$$

Based on (3.15), the final mathematical formula of the torque acting on the magnet by the electromagnetic solenoid is given by [83]:

$$\tau = \frac{\mu_0 \mu_r \mu_c \mu_m}{4\pi r^3} \left[3\cos(\psi - \theta)\sin(\psi - \beta) + \sin(\beta - \theta)\right] \tag{3.30}$$

As in the magnetic field analysis, if the material of the operating region around the coil is different of the coil's core material, then the relative permeability factor μ_r must be multiplied by the attenuation factor $\Re$. Based on (3.24-3.29), Fig. 3.8, shows variation of the magnetic force components and angle exerted by the coil placed in the origin with rotation angles $\theta = 0°$ and $\phi = 0°$ on the inserted magnet placed at position $p(0, 0, 0.16)$ with the azimuth angle $\alpha = 0°$ and variable inclination angle $\beta = 0 - 360°$.

Based on (3.29), magnetic torque exerted by the coil on the embedded magnet with

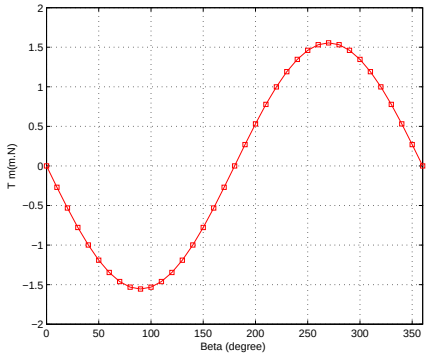

Figure 3.9: Magnetic torque variation based on fixed dipole position.

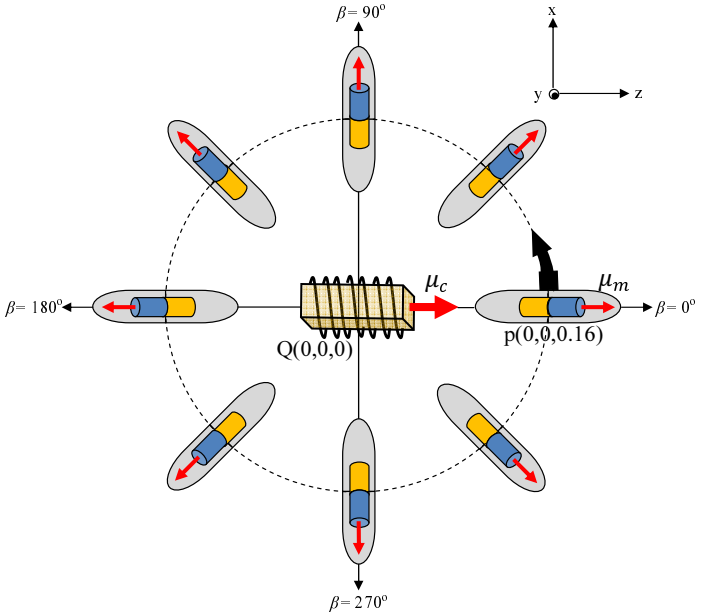

Figure 3.10: Location of the coil and the capsule.

the pitching angle variation $\beta = 0 - 360°$ is illustrated in Fig. 3.9.

For the scenario presented in Fig. 3.10, the distribution of the magnetic force components and angle based on the direction and location of the embedded dipole are shown in Fig. 3.11. Based on (3.29), Fig. 3.12 represents the distribution of the magnetic torque exerted by the coil on the embedded dipole with the inclination angle variation $\beta = 0 - 360°$.

It should be noted from Fig. 3.11 and 3.12 that, based on a different magnet position, a maximum magnetic force is applied to the embedded magnet when it is aligned with the magnetic source. Conversely, a minimum magnetic force is exerted when the inserted dipole is in a perpendicular position and vice versa for magnetic torque.

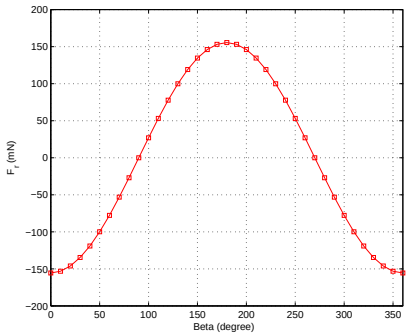

(a) F_r component.

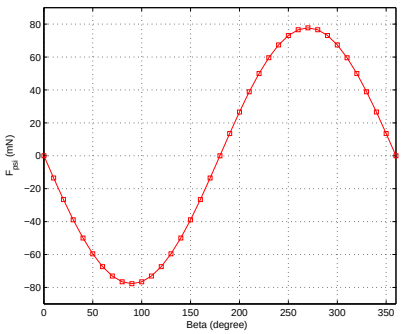

(b) F_{psi} component.

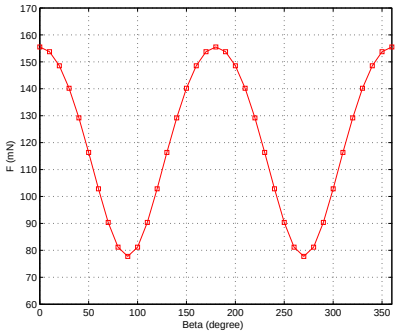

(c) Magnetic force.

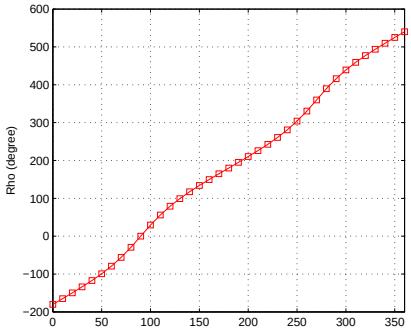

(d) Magnetic force angle.

Figure 3.11: Magnetic force components and angle based on variable dipole position.

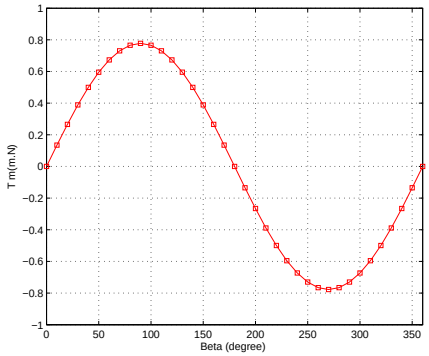

Figure 3.12: Magnetic torque variation based on variable dipole position.

3.2.2 Analysis of Coil Parameters

In this section the distribution of the magnetic field of the coil is analysed based on its physical and electrical parameters, which include size, current, the number of turns, and iron core permeability. The objective of the coil design is to increase the strength of its magnetic field to a level to which it can supply the magnetic force required to achieve a realistic capsule levitation distance. There are many parameters which can

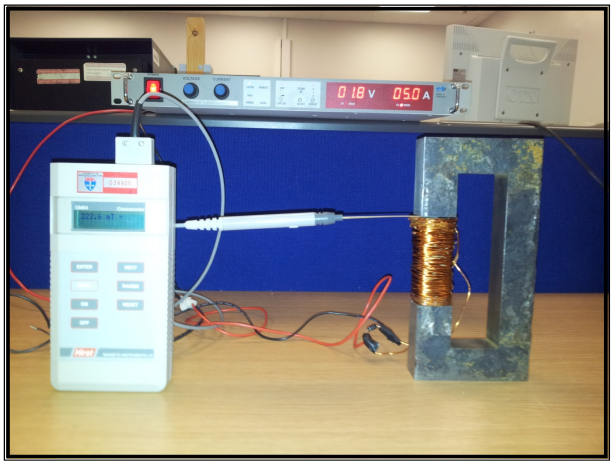

Figure 3.13: Measurement setup of iron core permeability.

be manipulated to strengthen the magnetic field of the actuator, and these include core permeability, size, current, and the number of turns of the electromagnetic coil. The strength and uniformity of the magnetic field are the considered criteria for the comparison of the magnetic behaviour of designed actuators.

3.2.2.1 Coil core permeability

Using an iron core of high permeability, μ_r can increase the magnetic field produced by the actuator in the free space medium by strength factor $\mu_r \Re$. In this application, the permeability of the iron core material is measured practically. The experimental setup is shown in Fig. 3.13, which is mainly composed of a C-shaped core, with sharp corners made of the same material of the coil core, and GUSSmeter equipment to measure the electromagnetic field produced by the solenoid.

The practical magnetization curve of the used solenoid core material is illustrated in Fig. 3.14. It can be seen from the above BH curve that, as the magnetizing field H increases, the magnetic field density approaches a maximum value asymptotically, at which the core material is saturated magnetically. The corresponding coil current value at the saturation state (I_{sat}) is (20) A, which is calculated based on the following equation:

$$I_{sat} = \frac{H L_c}{N} \tag{3.31}$$

Above saturation, the magnetic field continues to grow, but at the parametric rate, which is of the 3 orders of magnitude smaller than the ferromagnetic seen below saturation. Consequently, to keep the actuator working within the linear region, it should be excited by a current less than the saturation current value.

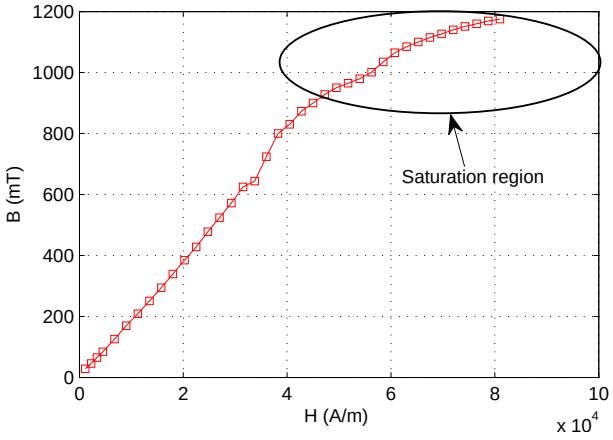

Figure 3.14: B-H curve of core material.

The magnetic permeability of the core material is given by:

$$\mu_r = \frac{B}{\mu_0 H}, \tag{3.32}$$

using the above equation, the maximum magnetic permeability of the used core material is approximately (15) which is considered too low, and its corresponding coil current value is ($I_c = 9$) A. It is worth considering that the actual value of the core permeability must be more than the measured value; the reason for this is that there is leakage of the magnetic field due to the existence of an air cap between the coil core and the C-core. In our application, the magnetic strength factor $\mu_r \Re$ is measured to be 3 which is valid within a small region around a vertical distance of 30 mm from the close coil's pole. The used material has poor permeability, so to improve the actuator strength a purified iron core with high permeability should be used instead of the one used in this setup.

3.2.2.2 Physical dimensions

The manipulation of the physical dimensions of the solenoid coil, which includes length and cross-section area, can be adopted to increase the strength of the magnetic response of the coil. As mentioned earlier, the proposed magnetic actuation system includes using an external magnetic field source to move an embedded magnet enclosed in the WCE inside the human body, so the expected manipulation region is far away from the magnetic source.

Based on (3.13) the length of the coil parameter has a little influence on the dis-

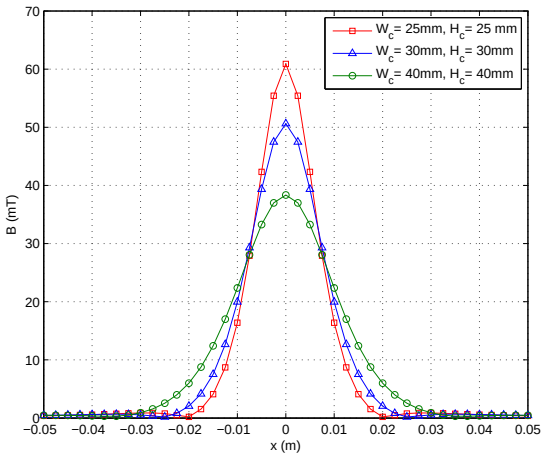

Figure 3.15: Magnetic field at $z = 40$ mm for coils with different cross section areas.

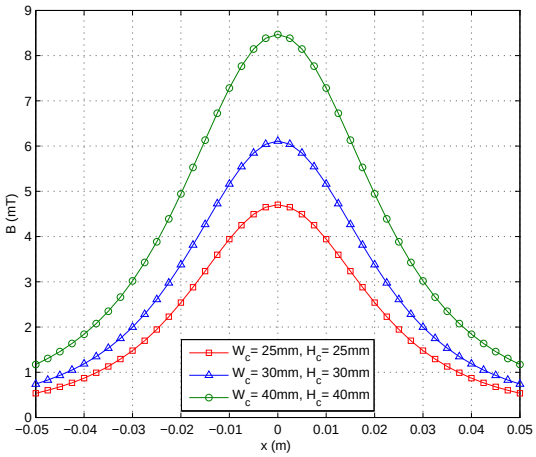

Figure 3.16: magnetic field at $z = 70$ mm for coils with different cross section areas.

tribution of the magnetic field, while based on the approximation magnetic field formula (3.12) this parameter have no influence on the magnetic behaviour of the coil. Therefore, the cross-section area of the coil is the only promising geometry parameter, which can be optimised to strengthen the magnetic field. Based on (3.13), Figs. 3.15, 3.16, and 3.17 show the magnetic field distribution along the x-axis at a distance of $z = 40, 70$ and 160 mm respectively for coil structures with cross-section dimensions of (25x25 mm, 30x30 mm, and 40x40 mm) respectively and the number of turns of 180.

It should be noted that the generated magnetic field increases as the cross-section parameter factor of the coil gets bigger. However, the relationship between the magnetic field strength and this factor is not directly proportional as it is expect that the magnetic field gets smaller at continue increasing the coil's pole face area. The

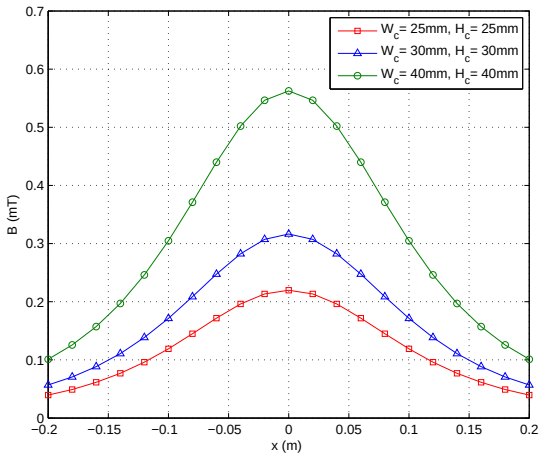

Figure 3.17: Magnetic field at $z = 160$ mm for coils with different cross section areas.

Table 3.3: Geometry and electrical parameters of the cylindrical coil.

Parameter	Value
L_c	80 mm
I	5 A
N	200
μ_r	5000
D_w	0.5 mm

finite element method based on Comsol software is adopted to analysis the magnetic field and find an optimum physical coil parameters.

Based on the coil's parameters as listed on the Table (3.3) and using Comsol software, Fig. 3.18 shows magnetic field distribution at axial distance z of 5 cm using different coil's radius. It can be seen from Fig. 3.18 that the optimum coil's radius r_c is 48 mm at which a strongest magnetic field is supplied at region around the distance $z = 5$ cm. In this research project, we define a coil dimension factor D_f as the ratio of distance z to the coil's radius r_c $(\frac{z}{r_c})$ which can be used to calculate the optimum coil's radius for any interesting distance. In this application, based on Fig. 3.18 the value of the factor D_f is 1.04167.

3.2.2.3 Coil current

Fig. 3.19 shows the magnet field distribution at $z = 160$ mm along the x-axis for coil placed at $q(0, 0, 0)$ and oriented to the positive z-axis with a cross-section area (30x30 mm)and the number of turns 0f 180 based on current range $1 - 7$ A with

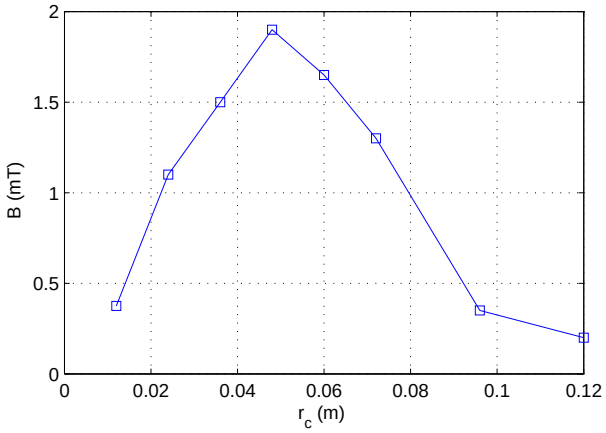

Figure 3.18: Magnetic field distribution at $z = 5$ cm based on different coil's radius.

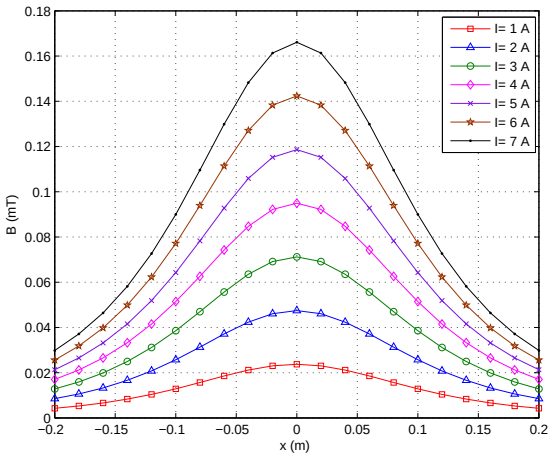

Figure 3.19: Magnetic field variation based on different coil currents.

a step of 1 A. It should be noted from Fig. 3.19 that the magnetic field increases by raising the coil excitation current in accordance with the directly proportionality between them in (3.12). In this application, the current increase is restricted by a value at which the coil core material reaches magnetic saturation, which is 20 A. It is worth considering that increasing the current I leads to an increase in power dissipation in the coil:

$$P = I^2 R, \tag{3.33}$$

where R is the coil resistance (Ω), which increases the actuator temperature and, consequentially, changing the system behaviour. Therefore, there is a trade off between magnetic field strength and solenoid heat dissipation. However, a potential solution which can be adopted to reduce the power dissipation of the system is the use of a superconductor, as its resistance is too low compared with the normal conductor. Consequentially, based on using a superconductor coil, the increasing of

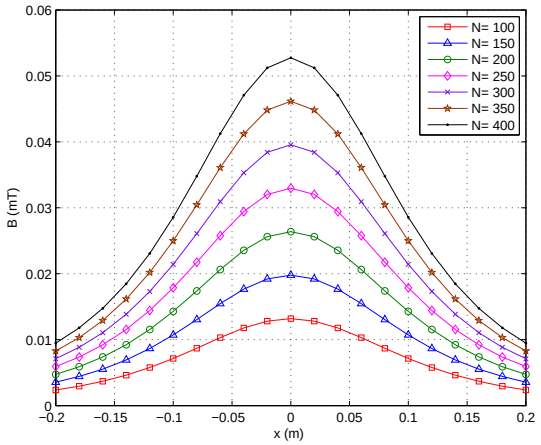

Figure 3.20: Magnetic field distribution based on different turns number.

the excitation current of the actuator may be a promising procedure to strengthen the magnetic actuation field while keeping the scheme dissipation power at a minimal value.

3.2.2.4 Turns number

Increasing the number of turns in the coil is another approach which can be adopted to support the strength of the magnetic field density. Based on (3.12), Fig. 3.20 shows that increasing the number of turns increases the strength of the magnetic field generated from the coil with a cross-section area of (30x30 mm) and a current of 1 A at $z = 160$ mm for winding number $N = 100 - 400$ with a step of 100 turns. However, based on the following equation, increasing the number of turns increases coil inductance L_n

$$L_n = \frac{\mu_r N^2 A_c}{L}, \tag{3.34}$$

and consequently the response time R_T of the system.

$$R_T = \frac{L_n}{R} \tag{3.35}$$

3.2.3 Electromagnetic Coil Design

The objective of the coil design is to increase the strength of its actuation magnetic field to a level so that it can achieve a realistic capsule levitation distance. There are many parameters which can be manipulated to strengthen the magnetic field of the actuator, and these include core permeability, size, current, and the number

Table 3.4: Geometry and electrical parameters of the cylindrical coil.

Parameter	Value
L_c	30 mm
r_c	12.5 mm
I	1 A
N	200
μ_r	25
D_w	1 mm

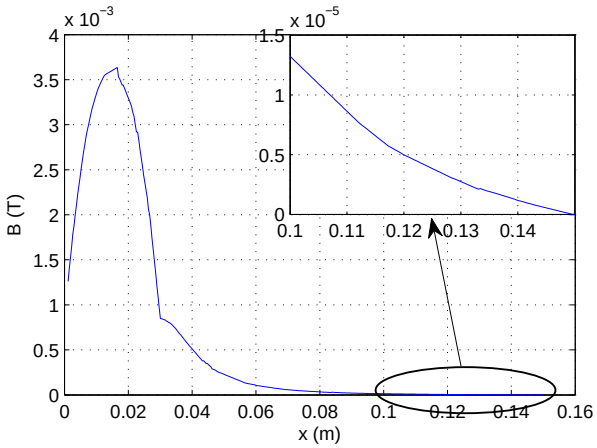

Figure 3.21: Magnetic field distribution on axis of cylindrical coil (12.5 x 30 mm).

of turns of the coil. It is worth noting that the coil parameters are designed so that the actuator can supply a high magnetic field while keeping the consumption power and the system response time within acceptable and reasonable limits. The strength and uniformity of the magnetic field are the criteria considered to evaluate the magnetic behaviour of the actuator. In this research project, Comsol software is used to design proposed actuator coil for colon examination. In order to assess the magnetic field modelling based on the simulation software, the magnetic field variation of a cylindrical coil placed at p(15 mm,0,0) and oriented to the positive x-axis with parameters as listed in Table (3.4) is analysed using Comsol software as shown in Fig. 3.21. It should be noted that the simulation yielded a magnetic field distribution as theoretically expected: the magnetic field is at its maximum in the coil center and this reduces as the third-order with distance.

To further enhance the reliability of the Comsol model, it is compared to experimental and analytical (3.12) studies, as shown in Fig. 3.22. It can be seen that there is a difference between the analyses which decreases as the distance increases. The reason for this is that the simulation results are based on a magnetic field expres-

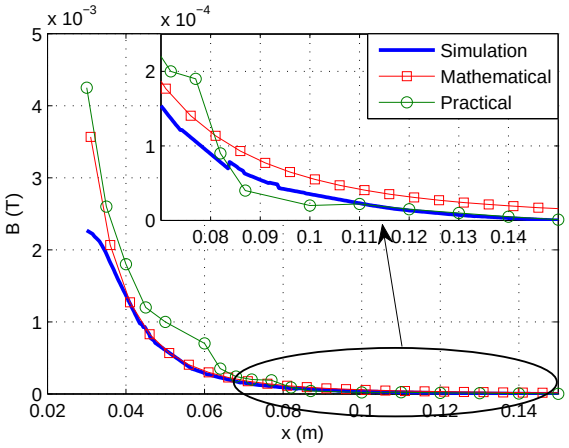

Figure 3.22: Theoretical, simulation and practical magnetic field distribution of cylindrical coil (12.5 x 30 mm).

sion which is only valid for far field analyses. However, the far field is the range of operation and because the match between the experimental and simulation results is satisfactory, the Comsol tool can be adopted to design the proposed coil.

As mentioned earlier, the objective of the coil design is to increase the strength of the actuation magnetic field. In this research project, the geometry and electrical parameters of the proposed coil are optimised based on the magnetic field analysis. The number of turns of the proposed coil is chosen as the same number as the present coil used in experiments with (200) turns based on the actuation magnetic field being strengthened while keeping the response time within a rate so that it can run an active closed-loop control system. Additionally, a purified iron core (99.8 % pure) with a higher permeability is used to increase the strength of the actuator. Further increasing in the levitation distance can be achieved by using a lighter and smaller size rare-earth magnet ($Nd_2Fe_{14}B$ sintered) with a higher magnetic strength B_i so that it can fit within the capsule endoscope, as the used one is non-ideal due to its size and heavy weight. The values of the designed coil parameters are listed in Table (3.5). Fig. 3.23 shows the distribution of the magnetic field along the x-axis of the proposed coil, which is placed at q(0.04,0,0) and oriented to the x-axis. It worth considering that based on the designed coil, the generated actuation field is increased to more than ten times that produced by the present coil used in experiments (whose parameters will be listed in Table (4.1)) and at distance $x = 15$ cm is 7 mT. The measured magnetic field produced by the present coil in experiments at a distance of 3 cm is 1.026 mT.

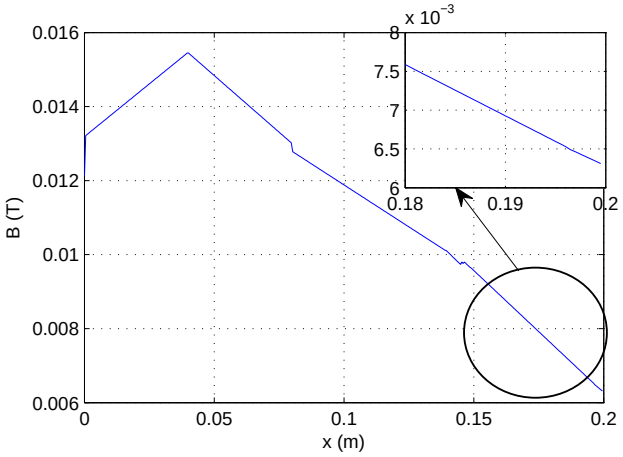

Figure 3.23: Magnetic field distribution on axis of the proposed coil.

Table 3.5: Structure design parameters of the proposed electromagnetic coil.

Parameter	Value	Parameter	Value
L_c	80 mm	m	$0.01kg$
r_c	48 mm	B_i	1.5 T
I	5 A	μ_r	5000
N	200	D_w	0.5 mm

It is worth noting that from Fig. 3.22 it is clear that the simulation results are lower than the practical results. Therefore, it is expected that the experimental result of the magnetic field strength produced by the proposed coil will be bigger than the simulated value; hence, the levitation distance will be higher than simulated.

3.3 Chapter Summary

The power source of the proposed capsule actuation system is the magnetic field density, and therefore, this chapter has emphasised the derivation of the general mathematical formula for the magnetic field produced by a magnetic source (electromagnetic coil, permanent magnet) in 3D. The distribution of the magnetic field around the coil is assessed based on strength and uniformity criteria. The core geometry and electrical parameters (permeability, current, and the number of turns) of the coil were considered as manipulation factors in the design of the proposed magnetic actuation source.

This chapter also concentrated on the derivation of the mathematical expression of the magnetic force and torque in Cartesian and spherical coordinate systems. Several coils with different geometry and electrical parameters were fabricated and

evaluated based on the experimental field measurements.

The physical and electrical parameters of the coil are analysed in order to optimise proposed coil for realistic capsule suspension distance. The practical B-H curve was presented in this analysis which revealed the poor permeability of the used core material. Increasing the strength of the actuator requires using higher permeability iron core. Based on the analyses it was found that manipulation the cross-section area of the coil's core can varying the strength of the generated magnetic field. An increasing in the actuation magnetic field was achieved based on optimum coil's radius which is obtained using Comsol software. Furthermore, the actuation field can be increased significantly by increasing the coil current, which consequently increases the maximum levitation distance. Nevertheless, this action leads to problems of power consumption and dissipation. The most practical solution to reduce the power disspation in the coil, while keeping the strength of the generated field, is to reduce the current and compensate that by using a high permeabity iron core. Another possible approach to decrease the power dissipation is using super conducor actuator windings incorpoating a suitable cooling system

The analyses were also showed that increasing the number of windings can increase the magnetic field and support the magnetic force. However, the coil inductance is raised and, as a result, so is the time system response. Moreover, this chapter introduced the B-H curve which revealed the poor permeability of the used core material. Consequently, the best way to optimize the actuator is through using a high permeability material in order to increase the maximum levitation distance to a realistic value for the inspection of the colon. Finally, the Comsol software was used to optimize the parameters of a proposed actuator for more realistic levitation distance.

In our research project, this chapter serves as a building block for the proposed actuation system as the designed actuator and the derived expression described in this chapter will be used in the simulation design and then the implementation of a realistic capsule actuation system for colon inspection.

Chapter 4

Simulation of Actuation Control System

In this chapter, SISO and MIMO linear controllers are proposed for the capsule actuation system, which is based on the well known magnetic levitation concept. A realistic simulation model of the actuation system was designed and implemented in a Matlab/Simulink environment to validate the proposed controllers.

For the 1D actuation system, 1DOF linear controllers with AC and DC position feedback based on the PID technique are considered in this chapter. For the 2D actuation system, 2DOF linear controllers with AC position feedback based on PP, EEA, and LQR approaches were also designed and simulated. To evaluate performance of the proposed system, the simulation results will then be discussed.

Finally, the simulation model equating to the 2D actuation system will be supported by improving the position feedback of the actuation algorithm through involving both the position and orientation of the capsule in the calculation of the controller output. Simulation results are provided to validate the developed actuation system.

4.1 1DOF Controller Simulation

This section introduces the design and simulation of PID controllers based on AC and DC position feedback for a 1D capsule actuation system. In the DC position feedback-based controller design, actuation and localisation of the control system is based on the DC magnetic field. In the AC position feedback-based controller system, the capsule actuation is still based on the DC magnetic field while an AC magnetic field is used for its localisation.

4.1.1 DC Position Feedback-Based Controller System

In this section, the 1DOF linear controller design based on the PID technique will be presented as the means of capsule actuation. Position feedback of the controller algorithm is based on the DC magnetic field of the magnet which is detected by a Hall effect sensor.

4.1.1.1 System configuration and modelling

System Configuration

The depicted stage of the 3DOF actuation system based on magnetic levitation is given in Fig. 4.1. The scheme consists of a controlled electromagnet, a small cylindrical permanent magnet, which made from an alloy of a neodymium, iron, and boron NdFeB enclosed by a capsule, two magnetic sensors, DSP, 3D simulated bowel tube, and a 3DOF (x, y, z) robotic movable frame.

The electromagnet is based on an iron-cored coil and fixed on the movable frame. The magnetic sensors, which are based on Hall effect sensors (A1301), are placed in the opposite extremities or poles of the electromagnet. The processor is used to implement a suitable controller algorithm in order to levitate the embedded magnet

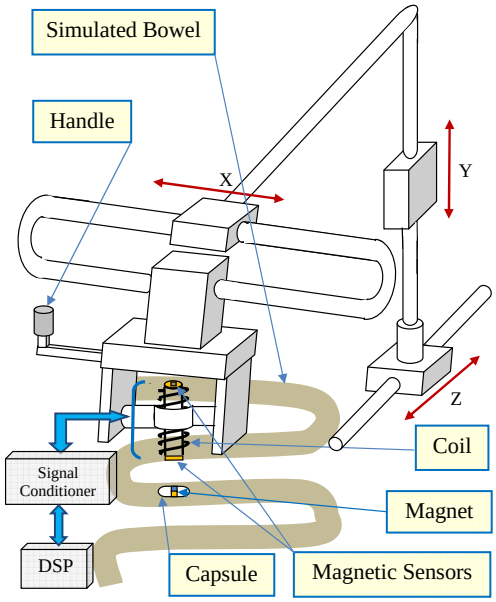

Figure 4.1: Simulated platform of the control system.

and keep it in the desired position related to the coil. In the proposed system, the levitated magnet can navigate the colon by moving the actuator above the human body using a robotic frame manipulator.

The introduced system, which is based on the magnetic levitation concept, is inherently unstable. Therefore, a closed-loop control system should be applied to stabilize the magnet at a desired position by adjusting the electrical current of the actuator. Generating an appropriate command signals needs a realistic dynamic model of the control system which will be discussed in the next section.

System Modelling and Dynamics

A schematic diagram of the 1DOF actuation system is shown in Fig. 4.2. The suspension system can be categorized into two systems: an electrical and a mechanical. The embedded dipole position in the mechanical system can be controlled by adjusting the magnetic force of the actuator in the electrical system through regulation of the coil current based on the position sensor feedback.

Assuming that the origin of the coordinate system is located in the centre of the

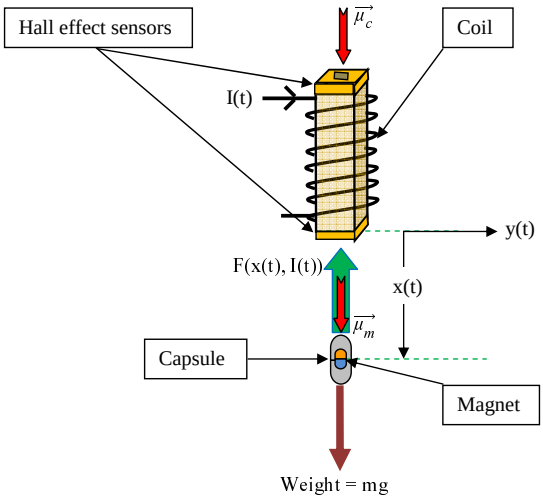

Figure 4.2: Conceptual schematic diagram of a single DOF control system.

electromagnet's lower pole, then the general magnetic force between the coil and the inserted dipole incorporating the attenuation factor $\Re$ and the magnetic moment of the coil and the magnet are as previously stated in Chapter 3 in (3.21), (3.2), and (3.16) respectively.

With the consideration of these assumptions, the magnetization of the permanent magnet and the actuator points to the positive x-axis, then based on (3.2), (3.3), (3.16), and (3.22), the magnetic moment expressions of the coil and the magnet can be rewritten as follows:

$$\begin{aligned} \vec{\mu}_c &= \mu_c i + 0j + 0k, \\ \vec{\mu}_m &= \mu_m i + 0j + 0k, \end{aligned} \tag{4.1}$$

while the position vector between the coil and the magnet placed $(x, 0, 0)$ is as follows:

$$\vec{r} = xi + 0j + 0k \tag{4.2}$$

Based on (4.1) and (4.2), the magnetic force (3.21) incorporating the attenuation factor $\Re$ can be written as follows:

$$F(x(t), I(t)) = K\frac{I(t)}{x^4(t)}, \tag{4.3}$$

where $K = \frac{3}{2\pi}\mu_r \Re N A_c B_i V$ is a force constant depends on the geometry of the system $\left(\frac{N\ m^4}{A}\right)$, $I(t)$ is the coil current (A), and $x(t)$ is the vertical distance between the magnet and the bottom pole of the actuator (m). The motion of the capsule in the magnetic field can be expressed by Newton's second law.

$$m\ddot{x}(t) = mg - K\frac{I(t)}{x^4(t)}, \tag{4.4}$$

where $\ddot{x}(t)$ is the magnet's acceleration in the x-direction $(\frac{m}{s^2})$, g denotes the acceleration of the system due to gravity $(\frac{m}{s^2})$. To design a linear control strategy, the above non-linear dynamic equation is linearized about suitable equilibrium values x_0 and I_0. Consider a perturbation about these equilibrium values is as follows:

$$\begin{aligned} \Delta x(t) &= x(t) - x_0, \\ \Delta I(t) &= I(t) - I_0, \end{aligned} \tag{4.5}$$

where $\Delta x(t)$, $\Delta I(t)$ are the position and current deviation from the equilibrium position x_0 and current I_0 respectively. Then the linearization of the model about the steady state values $(x(t) = x_0, I(t) = I_0)$ by Taylor's series expansion yields:

$$\ddot{\Delta x}(t) = \ddot{x}(t)|_{(x(t)=x_0, I(t)=I_0)} + \left.\frac{\partial \ddot{x}(t)}{\partial x(t)}\right|_{(x(t)=x_0, I(t)=I_0)} \Delta x(t) + \left.\frac{\partial \ddot{x}(t)}{\partial I(t)}\right|_{(x(t)=x_0, I(t)=I_0)} \Delta I(t) \tag{4.6}$$

At equilibrium point, $\ddot{x}(t) = 0$, then based on (4.4)

$$g = \frac{K}{m}\frac{I_0}{(x_0)^4} \tag{4.7}$$

and the equilibrium current is given by:

$$I_0 = \frac{mg(x_0)^4}{K} \tag{4.8}$$

Solving the partial differentials yields:

$$\begin{aligned} \left.\frac{\partial(\ddot{x}(t))}{\partial x(t)}\right|_{(x_0,I_0)} &= \frac{4KI_0}{mx_0^5}, \\ \left.\frac{\partial(\ddot{x}(t))}{\partial I(t)}\right|_{(x_0,I_0)} &= -\frac{K}{mx_0^4} \end{aligned} \tag{4.9}$$

Substituting (4.9) and (4.7) in (4.6) yields

$$\ddot{\Delta x}(t) = \frac{4KI_0}{mx_0^5}\Delta x(t) - \frac{K}{mx_0^4}\Delta I(t). \tag{4.10}$$

Finally, taking the Laplace transform of (4.10), the transfer function of the scheme with the change in electromagnet current as the system input and the change in device position as the system output is given by:

$$\frac{\Delta X(s)}{\Delta I(s)} = -\frac{d}{(s^2 - e)}, \tag{4.11}$$

where $\Delta X(s)$ and $\Delta I(s)$ are the Laplace transform of $\Delta x(t)$ and $\Delta I(t)$ respectively, $d = \frac{K}{mx_0^4}$, and $e = \frac{4KI_0}{mx_0^5}$. The negative sign in the above transfer function of the linearized system implies that with an increase in $\Delta I(t)$, there will be a decrease in Δx(t) and vice versa. It can be noted from the above transfer function that the system has two poles, one of which is in the right half plane at $\sqrt{4KI_0/mx_0^5}$, which makes the open-loop system unstable. Hence, a PID controller is presented in this

chapter to stabilize the capsule at the desired position.

To implement the controller in state space, the linearized system dynamics should be formulated in state space form. Let $\Delta X_{(n\times 1)}=\left[\Delta x(t)\ \dot{\Delta} x(t)\right]^T$ be the state vector of the system, $\Delta x(t)$ be the controlled output, and $\Delta U_{(m\times 1)}=[\Delta I(t)]$ be the control input vector, then based on (4.10), the state and output equation of the continuous time-invariant (TIV) system can be written as in (4.12) and (4.13) respectively.

$$\dot{\Delta X}(t) = A\Delta X(t) + B\Delta U(t) \tag{4.12}$$

$$\Delta Y(t) = C\Delta X(t) + D\Delta U(t), \tag{4.13}$$

where A is the system matrix (n×n), B is the input matrix (n×1), C is the output matrix (1×m), and D is the feed forward matrix (1×1), for the designed system. These matrices are given by:

$$A = \begin{bmatrix} 0 & 1 \\ e & 0 \end{bmatrix},\ B = \begin{bmatrix} 0 \\ -d \end{bmatrix},$$

$$C = \begin{bmatrix} 1 & 0 \end{bmatrix},\quad \text{and} \quad D = \begin{bmatrix} 0 \end{bmatrix}.$$

4.1.1.2 Actuation system design

Actuation Strategy

The main idea of the proposed approach is that the magnet, which is enclosed in the device as a marker for localisation, can also be moved and oriented by the magnetic force and torque of the external controlled DC magnetic field produced by coils placed outside the human body.

The proposed motion strategy for the WCE in the digestive tract includes the following steps:

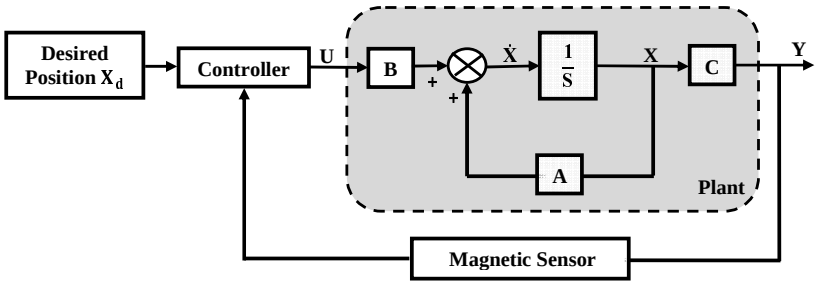

Figure 4.3: Block diagram of the control system in state space form.

- **Step1.** Applying a linear control system to move the embedded magnet in 1D within an area around the operating point and keep it at a desired position with a controllable x set-point relative to the coil.

- **Step2.** Navigate the inserted magnet through the bowel in the x, y and z-direction by translating the controlled electromagnet and/or the patient's bed using the 3DOF manipulator.

This research focuses on achievement of step1. The idea presented here for the proposed capsule navigation scheme is very simple as it has been based on the magnetic levitation concept which is highly recommended for accurate movement applications. Basically, the magnetic suspension systems are open-loop instable with fast dynamics, therefore, in order to stabilize the floating object at a desired position, a closed-loop control system must be applied to regulate the system.

The block diagram of the proposed feedback control scheme based on state space form is shown in Fig. 4.3. The main part of the control system is the controller, which is designed to adjust the actuator current based on the feedback information of the capsule position provided by the magnetic sensor.

Controller Technique

The controller for magnetic levitation systems requires a high degree of control and data-processing speed to achieve good performance. The proposed magnetic suspen-

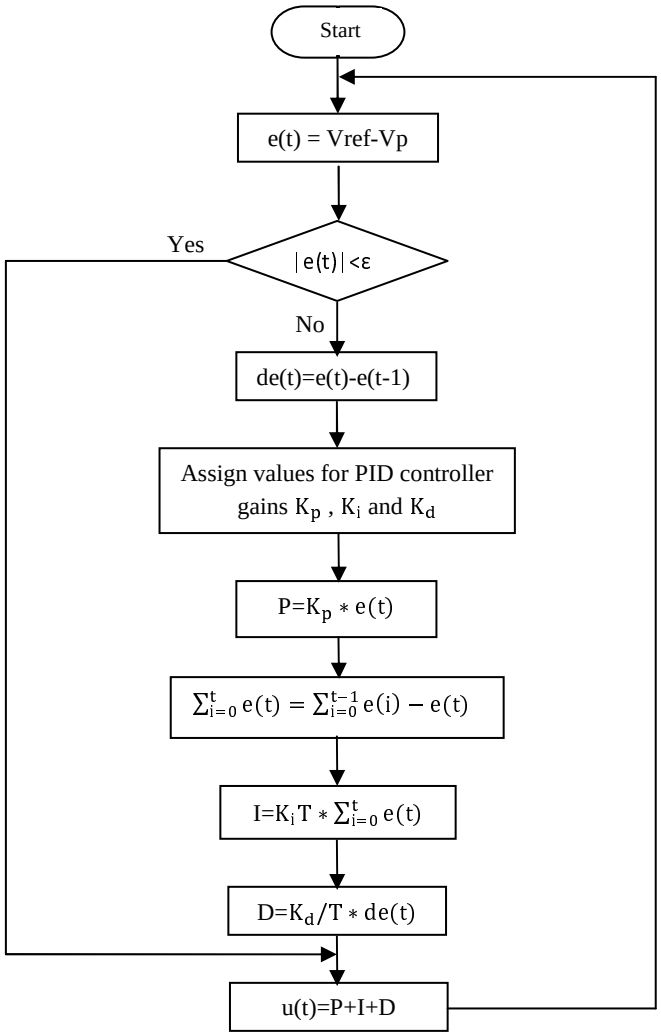

Figure 4.4: Flowchart of simulated PID controller.

sion system is inherently unstable and has nonlinear behaviour. In order to stabilize it, the linear PID controller is used due to its simplicity and reliability [67]. Details of the PID controller were stated in Chapter 2 section (2.3.1.1).

For known modelling systems, the performance of the controller depends on its parameter values K_p, K_i and K_d, which are obtained based on the scheme modelling expressions. The procedure of the implemented PID controller is clarified by the flowchart as shown in Fig. 4.4. The validity of the obtained controller parameters depends on realism of the system modelling, which is supported by including not only realistic electrical and mechanical system parameters, but also simulated process and measurement noise to compensate the actual system noise. In order to

achieve a good control response in the presence of this noise, tuning for the calculated controller parameters should be applied.

Controller Algorithm

In the proposed control algorithm, the magnet position detection is based on the idea that the upper sensor measures the magnetic field of the electromagnet, while the lower sensor senses the magnetic field for both the coil and dipole.

The position signal of the floating object is calculated based on its magnetic field which is effectively isolated by subtracting the sensor readings by a differential amplifier. The position signal is amplified and filtered by conditioner circuit, which will be discussed in detail in Chapter 5, and then sent to the DSP for sampling. In the processor, the sampled signal is compared with reference voltage corresponding to the desired capsule position to generate an error signal which is fed to the PID controller.

The controller calculates the control signal based on the error value and its gains K_p, K_i, and K_d. The controller parameters are set based on the demand system response which is based on maximum overshoot, rise time and steady state error. The controller output is finally sent through a current driver circuit to the electromagnet which supplies the magnetic force required to guide the capsule gradually to the desired position.

4.1.1.3 System simulation

A simulation design for a closed-loop control system must not only verify the proposed controller performance before validating it in real-time implementation, but also help to design the controller. A Matlab/Simulink environment is used as the

Table 4.1: Physical and magnetic parameters of the control system

Parameter	Value	Parameter	Value
N	200	m	0.0157 kg
L_c	0.03m	B_i	1T
W_c	0.03m	g	$9.81\frac{m}{s^2}$
r_d	0.006m	μ_0	$4\pi * 10^{-7}\frac{T\ m}{A}$
L_d	0.016m	K	$2.3328 * 10^{-7}\frac{N\ m^4}{A}$

simulation tool to verify the performance of the proposed controller based on the rise and settling time, maximum overshoot, and steady state error. The PID controller is designed for desired response with settling time t_s of 0.25 s and maximum percent overshoot $MPOS$ of 10%. The efficiency of the control system design depends on the similarity of the simulated and real-time systems. In this thesis, the realism of the simulation design of the actuation system is supported by using realistic magnetic and physical parameters values, which are listed in Table (4.1).

To further validate the system simulation design, the following procedures are taken into consideration:

1. The magnetic force constant K, which mainly depends on the vertical distance between the bottom of the coil pole and the centre of the floating object and the coil current at the equilibrium case, is measured experimentally as follows: after placing the dipole at the desired distance x_0, the coil current I_0 was increased slightly until the magnet just lifted off. Then, the practical magnetic force constant K can be calculated by substituting the measured parameters, x_0, I_0, m, and g into (4.8).

2. Two categories of noise, process and measurement noise, are included in the simulation model. Process noise based on Gaussian noise with mean value of

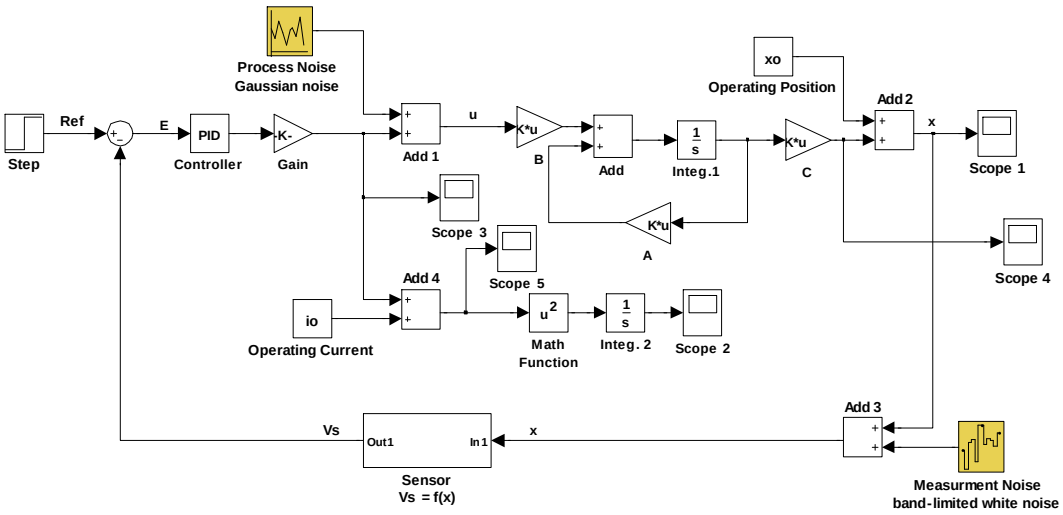

Figure 4.5: Simulink block diagram of the control system.

0 V and variance of 0.24 mV is added to include the effect of modelling system linearization, while measurement noise, which is based on band-limited white noise with power of 25 μV, is added to compensate for A/D quantization error and position sensor error.

3. Because it is difficult to make an accurate mathematical model of the sensor processor, an empirical model based on experimental measurements for the position sensor is considered. In the simulink design, a realistic calibration expression is used for capsule positioning, which is derived from practical positioning data (as seen in Chapter 5) instead of using the theoretical expression of the sensor stated in (5.1).

Realistic simulation design of the closed-loop control system based on the considerations mentioned above is shown in Fig. 4.5. In the Simulink model, the output of the system plant is calibrated into its corresponding voltage by the positioning unit which is then compared with the demand voltage to generate the error signal. After processing the error signal, the controller calculates the command signal which is used to guide the magnet through the demand trajectory.

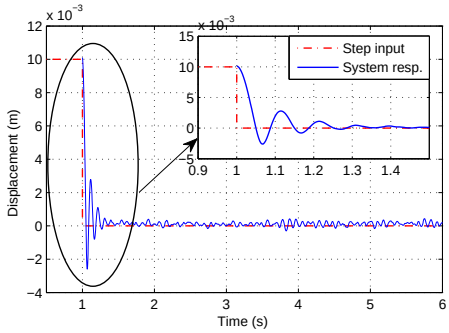

(a) Response of the state $\Delta x(t)$

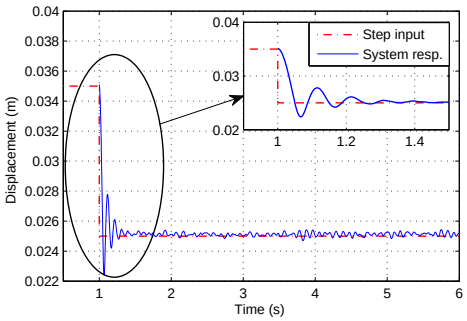

(b) Dipole position state $x(t)$ response

Figure 4.6: Simulated responses of the dipole position for step input based on the Hall effect sensor.

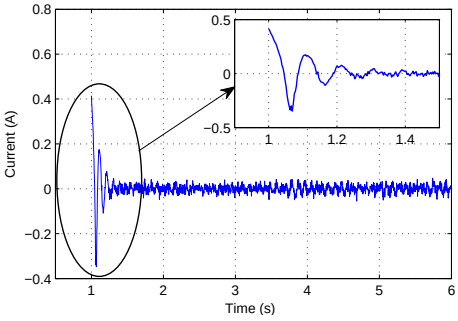

(a) Response of the state $\Delta i(t)$.

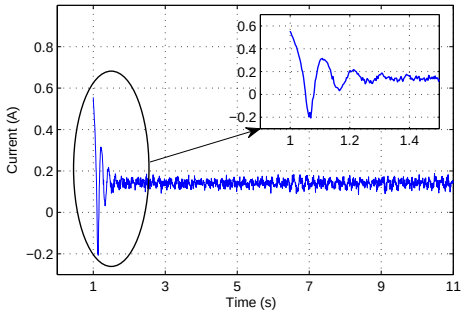

(b) Response of the system input signal $i(t)$.

Figure 4.7: Simulated responses of the system control effort under step input based on the Hall effect sensor.

4.1.1.4 Simulation results

Let the desired position of the actuation system be $x_0 = 25$ mm, then the operation current and the matrices elements of the scheme dynamics are calculated based on (4.8) and (4.10) respectively as follows:

$$I_0 = 0.14A, \qquad d = 69.7, \qquad e = 1569.6$$

In the simulated scheme, the initial position of the demand trajectory must be close to the operating point as the proposed linear controller is valid just around the equilibrium point by a distance of ± 1.25 cm.

Based on the initial dipole position $x_i = 35$ mm and velocity $V_{xi} = 0\ \frac{m}{s}$, the performance of the Simulink design is evaluated under step input. Standard control criteria which include rise and settling time, overshoot, and steady state error, are considered to evaluate the response of the simulated system.

For the position voltage step input $V_p = 2.0275$ V which corresponds to the vertical magnet position $x(t) = 25$ mm, the actual and desired time responses of the states $\Delta x(t)$ and $x(t)$ based on controller gains $K_p = 1.2, K_i = 0.02$, and $K_d = 0.035$ are shown in Fig. 4.6(a) and (b) respectively. Based on these gains, the pole p_1 and zeros z_1, z_2 locations of the controller are (0,-0.0167, and -34.3) respectively. Moreover, Fig. 4.7(a) and (b) show the control efforts required for $\Delta x(t)$ and $x(t)$ journey respectively.

The results of Fig. 4.6(a) and (b) suggest that, the controller enables the manipulating object to follow the desired step input trajectory very well. Based on the mini plot of Fig. 4.6(a), it should be noted that the controller output achieved a fast fall and settling time of 0.035 s and 0.35 s respectively. It is worth considering that the designed controller gains are tuned in order to achieve a simulation response close as much as possible to the desired response while keeping the control signal of the system as small as possible. However, there is a variance of approximately ± 0.35 mm around the desired position and an overshoot of approximately 2.5 mm due to process and measurement noise, which was incorporated into the system model. This variance in the embedded magnet position has no effect on the resolution of the taken pictures due to the low capture rate of the WCE's camera (2 frames per second) [84]. Regarding the overshoot, its level is within tolerance and will have no influence on the colon, as the shooting distance is very small in proportion to the diameter of narrowest region (approximately 60 mm) within the investigated

organ [85]. Regarding the system control effort, it can be seen from the mini figure Fig. 4.7(a) and (b) that the actuator control effort required to track the step trajectory was within reasonable and applicable values, with the initial value being approximately 0.41 A while the steady state value is approximately 0.14 A.

4.1.2 AC Position Feedback-Based Controller System

In this section, the AC magnetic signal is used for position feedback of the controller system which is also based on the linear PID technique.

4.1.2.1 System configuration

Simply, the AC position feedback-based controller system is the DC position feedback-based controller system with improved position sensing. In this positioning unit, a generating coil attached to the capsule is used to transmit the AC magnetic position signal through exciting it by an AC voltage signal. Furthermore, a coil sensor placed on the electromagnet's lower pole is also used instead of the Hall effect sensors for AC induced signal detection purposes. As in the controller system based on the Hall effect sensor, the coil sensor is modelled empirically based on experimental measurements which are used to derive an expression of the capsule position calibration (as seen in Chapter 5).

The Linear PID technique is also adopted to implement the controller of the proposed actuation system. Finally, it is worth considering that the capsule coil should be excited by a low frequency signal, which in this application is 100 kHz, in order to minimize absorption loss in human tissue.

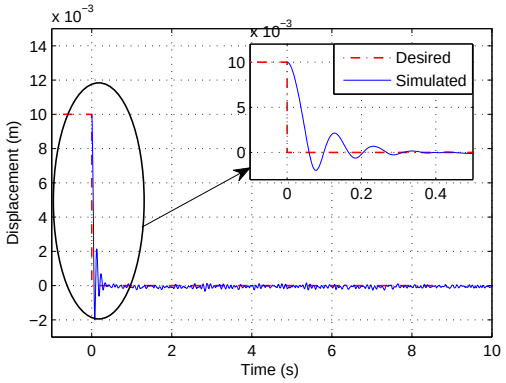

(a) Response of the state $\Delta x(t)$.

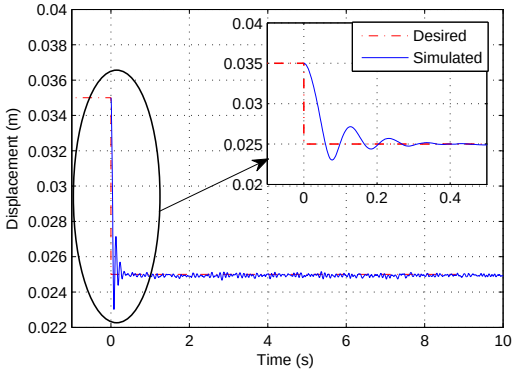

(b) Dipole position state $x(t)$ response.

Figure 4.8: Simulated responses of the dipole position for step input based on coil sensor

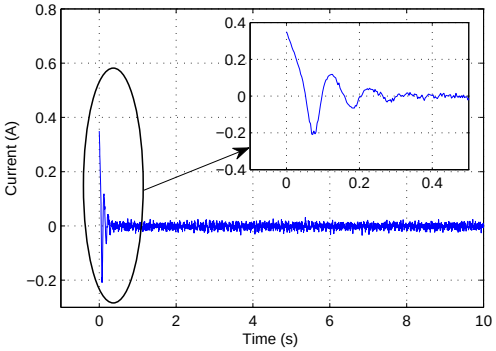

(a) Response of the state $\Delta I(t)$.

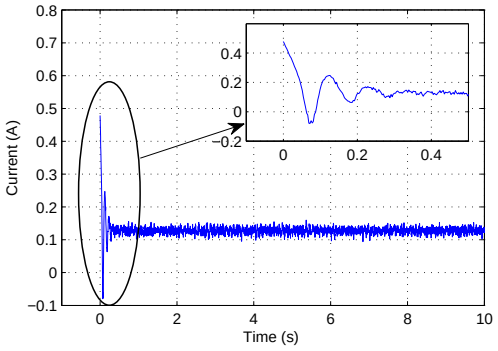

(b) Response of the system input signal $I(t)$.

Figure 4.9: Simulated responses of the system control effort under step input based on coil sensor

4.1.2.2 Simulation results

Based on the controller parameters $K_p = 0.576$, $K_i = 0.024$, and $K_d = 0.0216$, Fig. 4.8(a) and (b) show the actual and desired time response of the control system for the states $\Delta x(t)$ and $x(t)$ respectively for the desired capsule position $x = 25$ mm, which corresponds to the voltage sensor $Vcs(t) = 3.371$ V. The control signal required for the capsule displacement $\Delta x(t)$ and $x(t)$ are presented in Fig. 4.9(a) and (b) respectively. It can be seen from Fig. 4.8 that the controller based on coil sensor effectively guided the inserted magnet through the desired trajectory.

By comparing the mini plot of Fig. 4.6(a) and (b) and Fig. 4.8(a) and (b), it should be noted that the response of the system based on the coil sensor retains a short settling time of approximately of 0.25 s. In addition, the overshoot value is reduced from 28% to 20% and the position variation about the desired magnet position is reduced to approximately of ±0.2 mm. Moreover, the initial current of the system is decreased from 0.41 A to 0.33 A.

The good response of the AC position feedback-based controller system is achieved since the controller algorithm is fed by more accurate position feedback.

4.2 2DOF Controller Simulation

In this section, three controller techniques, PP, EEA, and LQR, are proposed for the 2D capsule actuation system. The controllers will be designed and simulated and their output response will be compared based on settling time, overshoot, and steady state error parameters in order to evaluate their tracking performance for the desired trajectories.

4.2.1 System Configuration and Modelling

4.2.1.1 System configuration

The simulated stage of the proposed 4DOF capsule actuation system is shown in Fig. 4.10. The scheme consists of a controlled electromagnet which is assembled using two iron-cored coils fixed symmetrically on a 4DOF Cartesian coordinate slide, a small cylindrical permanent magnet enclosed by a capsule with a generating coil, two magnetic position sensors attached to the lower poles of the actuator coils, a 3D simulated bowel tube, a controller and a 4DOF robot to move the coils frame.

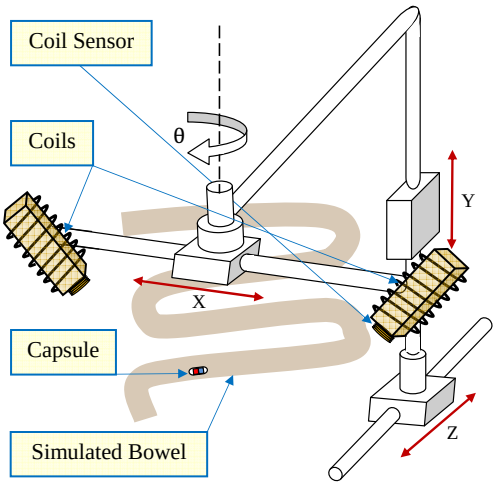

Figure 4.10: Platform of the 4DOF control system.

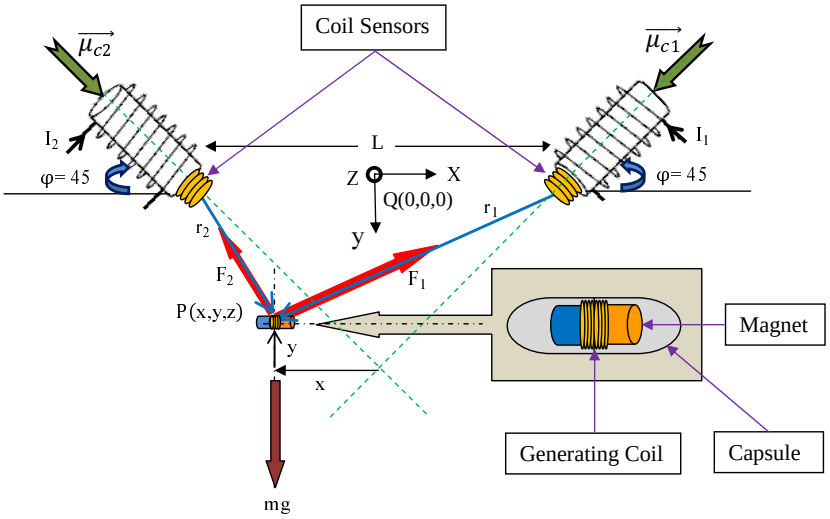

Figure 4.11: Schematic diagram of the 2D control system.

The sensors, which are based on the coil sensors, are used to provide the controller with feedback information about the capsule position, and is then used to adjust the actuator current required to move the capsule to the desired position.

4.2.1.2 System modelling and dynamics

A schematic diagram of the 2DOF control system is shown in Fig. 4.11. The magnetic force expression between the coil and the dipole is governed by (3.21) Considering these assumptions, the embedded magnet is initially placed close to the desired position in the xy-plane and the magnetization pole axis of the actuators are orthogonal in the plane $z = 0$. The movement of the inserted magnet in the x

and y-direction is governed by Newton's second law, and can be expressed as follows:

$$m\frac{d^2(x(t)y(t))}{dt^2} = \vec{F_1} + \vec{F_2} + \vec{W}, \tag{4.14}$$

where $\vec{F_1}$, $\vec{F_2}$ are vectors of the magnetic force exerted on the inserted magnet by coil_1 and coil_2 respectively (N) and $\vec{W}$ is the weight vector of the floating magnet (N). Using the general magnetic force expression (3.21) incorporating the attenuation factor $\Re$, (4.14) can be rewritten as follows:

$$\begin{aligned} m\frac{d^2(x(t)y(t))}{dt^2} =& \frac{3\mu_0\mu_r\Re}{4\pi}\sum_{k=1}^{2}\left\{\frac{(\vec{\mu}_{c_k}.\vec{r}_k)\vec{\mu}_m + (\vec{\mu}_m.\vec{r}_k)\vec{\mu}_{c_k} + (\vec{\mu}_{c_k}.\vec{\mu_m})\vec{r}_k}{r_k^5}\right. \\ & \left. -\frac{5(\vec{\mu}_{c_k}.\vec{r}_k)(\vec{\mu}_m.\vec{r}_k)\vec{r}_k}{r_k^7}\right\} + \vec{W} \end{aligned} \tag{4.15}$$

$$\text{where } \vec{\mu}_{c_1} = \mu_{c_1}\hat{\mu}_{c1} = N_1I_1A_{c1}\ (-\frac{1}{\sqrt{2}}i + \frac{1}{\sqrt{2}}j + 0k),$$

$$\vec{\mu_{c_2}} = \mu_{c_2}\hat{\mu}_{c_2} = N_2I_2A_{c2}\ (\frac{1}{\sqrt{2}}i + \frac{1}{\sqrt{2}}j + 0k),$$

$$\vec{\mu_m} = \mu_m\hat{\mu}_m = \frac{B_iV}{\mu_0}\ (i + 0j + 0k),$$

$$\vec{W} = W\hat{W} = mg\ (0i + j + 0k),$$

$$\vec{r_1} = r_1\hat{r_1} = \sqrt{X_1^2 + y^2(t)}\ \left[-\frac{X_1}{\sqrt{X_1^2 + y(t)^2}}i + \frac{y(t)}{\sqrt{X_1^2 + y^2(t)}}j + 0k\right],$$

$$\vec{r_2} = r_2\hat{r_2} = \sqrt{X_2^2 + y^2(t)}\ \left[\frac{X_2}{\sqrt{X_2^2 + y^2(t)}}i + \frac{y}{\sqrt{X_2^2 + y^2(t)}}j + 0k\right],$$

$X_1 = \frac{L}{2} - x(t)$, and $X_2 = \frac{L}{2} + x(t)$.

After simplification, the above equation can be rewritten as follows:

$$\begin{aligned} m\frac{d^2(x(t)y(t))}{dt^2} =& \sum_{k=1}^{2}\frac{K_kI_k}{r_k^4}\{(\hat{\mu}_{c_k}.\hat{r}_k)\hat{\mu}_m + (\hat{\mu}_m.\hat{r}_k)\hat{\mu}_{c_k} + (\hat{\mu}_{c_k}.\hat{\mu}_m)\hat{r}_k \\ & -5(\hat{\mu}_{c_k}.\hat{r}_k)(\hat{\mu}_m.\hat{r}_k)\hat{r}_k\} + W\hat{W}, \end{aligned} \tag{4.16}$$

where $K_k = \frac{3}{4\sqrt{2}\pi}\mu_r \Re N_{ck} A_{ck} B_i V$ is a magnetic force constant of coil$_k$ for $k = 1, 2$ that depends on the geometry of the system $\left(\frac{N\ m^4}{A}\right)$.

Assume the electromagnets have the same physical and magnetic parameters i.e $K_1 = K_2 = K$, then the equation of the manipulator motion in the x-direction based on (4.16) can be written as:

$$\ddot{x}(t) = \frac{K}{\sqrt{2}m} \sum_{k=1}^{2} I_k(t) \left[\frac{(3X_k + y(t))}{r_k^5} - \frac{5X_k^2(X_k + y(t))}{r_k^7} \right] \tag{4.17}$$

where $\ddot{x}(t)$ is the magnet's acceleration in the x-direction, k is the number of the coil.

To design a linear control system, the above non-linear dynamic equation is linearized using Taylor's series expansion about a suitable equilibrium point (x_0, y_0, I_{01}, I_{02}). If $X_{01} = \frac{L}{2} - x_0$, $X_{02} = \frac{L}{2} + x_0$, $r_{01} = \sqrt{X_{01}^2 + y_0^2}$, and $r_{02} = \sqrt{X_{02}^2 + y_0^2}$. Then the linearized model can be described by:

$$\ddot{\Delta x}(t) = C_1 \Delta I_1(t) + C_2 \Delta I_2(t) + (C_{3a} + C_{3b})\Delta x(t) + (C_{4a} + C_{4b})\Delta y(t), \tag{4.18}$$

where

$$C_1 = \frac{K}{\sqrt{2}m} \left[\frac{(3X_{01} + y_0)}{r_{01}^5} - \frac{5X_{01}^2(X_{01} + y_0)}{r_{01}^7} \right],$$

$$C_2 = \frac{K}{\sqrt{2}m} \left[\frac{(3X_{02} + y_0)}{r_{02}^5} - \frac{5X_{02}^2(X_{02} + y_0)}{r_{02}^7} \right],$$

$$\begin{aligned} C_{3a} \;=\; & \frac{K}{\sqrt{2}m}\, I_{01} \left[\frac{-3(X_{01}^2 + y_0^2) + 5X_{01}(3X_{01} + y_0)}{r_{01}^7} \right. \\ & \left. -\, 5\, \frac{X_{01}(X_{01}^2 + y_0^2)(-3X_{01} - 2y_0) + 7X_{01}^3(X_{01} + y_0)}{r_{01}^9} \right] \end{aligned}$$

$$C_{3b} = \frac{K}{\sqrt{2}m} I_{02} \left[\frac{3(X_{02}^2 + y_0^2) - 5X_{02}(3X_{02} + y_0)}{r_{02}^7} - 5 \frac{X_{02}(X_{02}^2 + y_0^2)(3X_{02} + 2y_0) - 7X_{02}^3(X_{02} + y_0)}{r_{02}^9} \right],$$

$$C_{4a} = \frac{K}{\sqrt{2}m} I_{01} \left[\frac{(X_{01}^2 + y_0^2) - 5y_0(3X_{01} + y_0)}{r_{01}^7} - 5 \frac{X_{01}^2(X_{01}^2 + y_0^2) - 7y_0X_{01}^2(X_{01} + y_0)}{r_{01}^9} \right]$$

and

$$C_{4b} = \frac{K}{\sqrt{2}m} I_{02} \left[\frac{(X_{02}^2 + y_0^2) - 5y_0(3X_{02} + y_0)}{r_{02}^7} - 5 \frac{X_{02}^2(X_{02}^2 + y_0^2) - 7y_0X_{02}^2(X_{02} + y_0)}{r_{02}^9} \right]$$

In the y-direction, the magnetic force between the coils and the inserted magnet can be expressed based on (4.3.1.2) as follows:

$$\ddot{y}(t) = \frac{K}{\sqrt{2}m} \sum_{k=1}^{2} (-1)^k I_k(t) \left[\frac{(X_k + y(t))}{r_k^5} - \frac{5X_k y(t)(X_k + y(t))}{r_k^7} \right] + mg, \quad (4.19)$$

where $\ddot{y}(t)$ is the magnet's acceleration in the y-direction ($\frac{m}{s^2}$). For linear controller implementation purposes, the above dynamic equation is linearised around the equilibrium point (x_0, y_0, I_{01}, I_{02}) as follows:

$$\ddot{\Delta y}(t) = D_1 \Delta I_1(t) + D_2 \Delta I_2(t) + (D_{3a} + D_{3b}) \Delta x(t) + (D_{4a} + D_{4b}) \Delta y(t), \quad (4.20)$$

where

$$D_1 = \frac{K}{\sqrt{2}m} \left[\frac{-(X_{01} + y_0)}{r_{01}^5} + 5 \frac{X_{01} y_0 (X_{01} + y_0)}{r_{01}^7} \right],$$

$$D_2 = \frac{K}{\sqrt{2}m} \left[\frac{(X_{02} + y_0)}{r_{02}^5} - 5 \frac{X_{02} y_0 (X_{02} + y_0)}{r_{02}^7} \right],$$

$$D_{3a} = \frac{K}{\sqrt{2}m} I_{01} \left[\frac{(X_{01}^2 + y_0^2) - 5X_{01}(X_{01} + y_0)}{r_{01}^7} + 5 \frac{y_0(-2X_{01} - y_0)(X_{01}^2 + y_0^2) + 7X_{01}^2 y_0(X_{01} + y_0)}{r_{01}^9} \right],$$

$$D_{3b} = \frac{K}{\sqrt{2}m} I_{02} \left[\frac{(X_{02}^2 + y_0^2) - 5X_{02}(X_{02} + y_0)}{r_{02}^7} - 5 \frac{y_0(2X_{02} + y_0)(X_{02}^2 + y_0^2) - 7X_{02}^2 y_0(X_{02} + y_0)}{r_{02}^9} \right],$$

$$D_{4a} = \frac{K}{\sqrt{2}m} I_{01} \left[-\frac{(X_{01}^2 + y_0^2) - 5y_0(X_{01} + y_0)}{r_{01}^7} + 5 \frac{X_{01}(X_{01} + 2y_0)(X_{01}^2 + y_0^2) - 7X_{01}y_0^2(X_{01} + y_0)}{r_{01}^9} \right],$$

$$D_{4b} = \frac{K}{\sqrt{2}m} I_{02} \left[\frac{(X_{02}^2 + y_0^2) - 5y_0(X_{02} + y_0)}{r_{02}^7} - 5 \frac{X_{02}(X_{02} + 2y_0)(X_{02}^2 + y_0^2) - 7X_{02}y_0^2(X_{02} + y_0)}{r_{02}^9} \right].$$

From the free body diagram in Fig. 4.11, at the equilibrium point, the resultant magnetic force exerted by the actuator on the levitated magnet in the x-direction is zero where as in the y-direction equals the gravitational force. Based on (4.17) and (4.19), the control inputs I_{01} and I_{02} at the equilibrium point can be calculated using the following equations:

$$I_{01} = -\frac{mg \left[\frac{3X_{02}+y_0}{r_{02}^5} - \frac{5X_{02}^2(X_{02}+y_0)}{r_{02}^7} \right]}{\sqrt{2}K(S_1 - S_2)}, \tag{4.21}$$

$$I_{02} = \frac{mg \left[\frac{3X_{01}+y_0}{r_{01}^5} - \frac{5X_{01}^2(X_{01}+y_0)}{r_{01}^7} \right]}{\sqrt{2}K(S_1 - S_2)}, \tag{4.22}$$

where $S_1 = \left[\frac{-X_{01} - y_0}{r_{01}^5} + \frac{5X_{01}y_0(X_{01} + y_0)}{r_{01}^7} \right] \left[\frac{3X_{02} + y_0}{r_{02}^5} - \frac{5X_{02}^2(X_{02} + y_0)}{r_{02}^7} \right],$

and $S_2 = \left[\frac{-X_{02} - y_0}{r_{02}^5} - \frac{5X_{02}y_0(X_{02} + y_0)}{r_{02}^7}\right]\left[\frac{3X_{01} + y_0}{r_{01}^5} - \frac{5X_{01}^2(X_{01} + y_0)}{r_{01}^7}\right]$.

To design the MIMO controller, the system dynamics should be formulated in state space form, let $\Delta X_{(n\times 1)}=\left[\Delta x(t)\ \dot{\Delta}x(t)\ \Delta y(t)\ \dot{\Delta}y(t)\right]^T$ be the state vector of the system, $\Delta x(t)$ and $\Delta y(t)$ be the controlled output, and $\Delta U_{(m\times 1)}=[\Delta I_1(t)\ \Delta I_2(t)]^T$ be the control input's vector, then the state and output equation of the system can be written based on (4.18) and (4.20) as in (4.23) and (4.24) respectively.

$$\dot{\Delta X}(t) = A\Delta X(t) + B\Delta U(t) \tag{4.23}$$

$$\Delta Y(t) = C\Delta X(t) + D\Delta U(t), \tag{4.24}$$

where

$$A = \begin{bmatrix} 0 & 1 & 0 & 0 \\ C_3 & 0 & C_4 & 0 \\ 0 & 0 & 0 & 1 \\ D_3 & 0 & D_4 & 0 \end{bmatrix},\ B = \begin{bmatrix} 0 & 0 \\ C_1 & C_2 \\ 0 & 0 \\ D_1 & D_2 \end{bmatrix},$$

$$C = \begin{bmatrix} 1 & 0 & 0 & 0 \\ 0 & 0 & 1 & 0 \end{bmatrix}, \quad \text{and} \qquad D = \begin{bmatrix} 0 & 0 \\ 0 & 0 \end{bmatrix}.$$

4.2.2 Strategy of the Actuation System

The proposed motion strategy for the WCE in the digestive tract includes implementation of the following steps:

- **Step1**. Move the embedded magnet in the xy-plane by the control system around the operating point and keep it at a variable-y desired position relative to the electromagnetic frame.

- **Step2**. Navigate the inserted dipole in the x, y and z-direction and orient it horizontally with inclination angle θ through the simulated bowel by moving

the actuator frame and/or the patient's bed using the robotic frame manipulator.

This research focuses on the design of a linear MIMO 2DOF controller based on the PP, EEA and LQR tracking techniques to achieve step1. The protocol of the proposed actuation system is based on the basic idea that the vertical and horizontal magnetic force generated by the actuator and exerted on the embedded magnet can be used to fix the position of the dipole in the xy-plane (with a controllable y setpoint) and fix the orientation with respect to the coils. The stable device then navigates in the 4DOF (x, y, z and θ) through the bowel by moving the frame and/or the patient's bed. To realise the desired position, the controller is designed to supply reasonable control inputs required for capsule actuation based on the position feedback information from the magnetic sensors.

4.2.3 Controller Design Methods

In this section, the state feedback controller based on the PP, EEA, and LQR techniques is designed to implement a tracking algorithm so that the system outputs can follow the command of the desired inputs. In the PP and LQR approaches, all the states are assumed to be measurable.

The trackers are simulated at equilibrium point $[x_0\ y_0]^T = [0\ 0.025]^T$, initial states position $[\Delta x_i\ \dot{\Delta x}_i\ \Delta y_i\ \dot{\Delta y}_i]^T$=$[0.005\ 0\ 0.01\ 0]^T$, and desired inputs $X_{d(p\times 1)}$=$[\Delta x_d\ \dot{\Delta x}_d\ \Delta y_d\ \dot{\Delta y}_d]^T$=$[0\ 0\ 0.005\ 0]^T$ based on Gaussian process noise with mean value of 0 V and variance of 0.24 mV and band-limited white measurement noise with power of 25 μV. To evaluate the proposed controllers, their tracking performance is compared based on maximum overshoot, settling time and steady state error parameters.

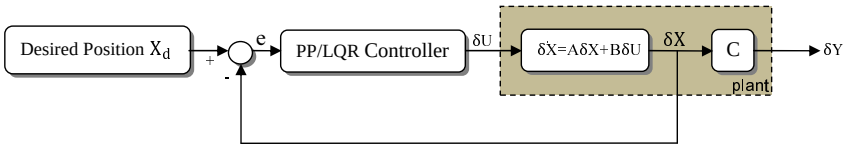

Figure 4.12: Block diagram of the PP tracker system.

Table 4.2: Physical and magnetic parameters of the control system

Parameter	Value	Parameter	Value
I_{01}	-0.7472 A	C_4	0
I_{02}	0.7472 A	D_1	9.285
C_1	-5.472	D_2	-9.285
C_2	-5.472	D_3	0
C_3	46.144	D_4	716.372

4.2.3.1 Simulation and results of the PP tracker

The block diagram of the closed-loop control system based on the state feedback pole placement controller is shown Fig. 4.12. The design of the controller involves applying the input vector [71]

$$\delta U(t) = K(X_d(t) - \Delta X(t)) - K_d X_d(t), \tag{4.25}$$

to minimize the tracking error

$$e(t) = X_d(t) - \Delta X(t), \tag{4.26}$$

through forcing the plant states $\Delta X(t)$ to follow a specified desired trajectory $X_d(t)$, where K_d and K are forward and feedback gain matrices.

Let the horizontal distance between the coils $L = 0.06$ m and the magnetic field strength factor $\mu_r \Re$ of the actuator core material be 3, then the main parameters and the matrices' elements of the tracking scheme, are calculated at the operating point X_0=$[x_0\ y_0]^T$= $[0\ 0.025]^T$ using (4.18), (4.20), (4.21) and (4.22) and listed in

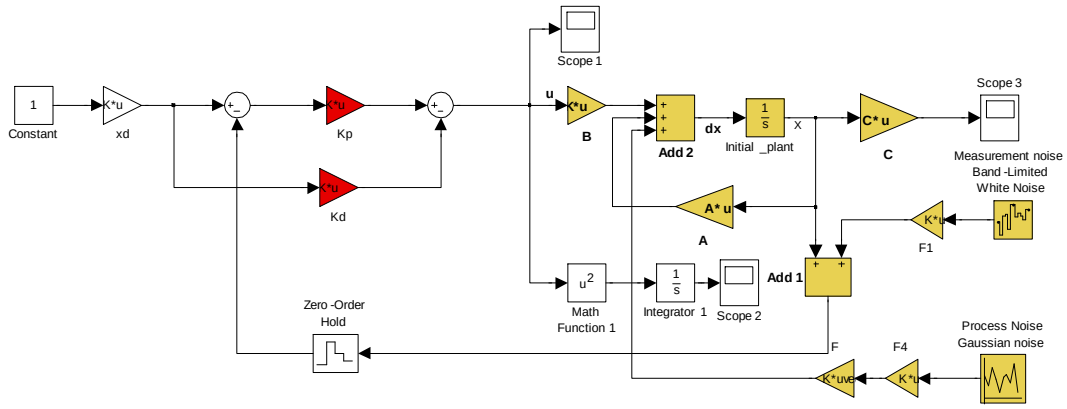

Figure 4.13: Simulink design of the MIMO tracking system based on the PP controller.

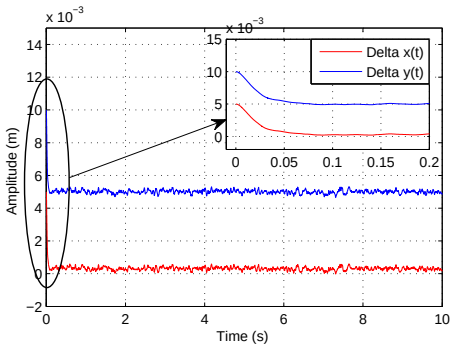

(a) $\delta x(t)$ and $\delta y(t)$ response

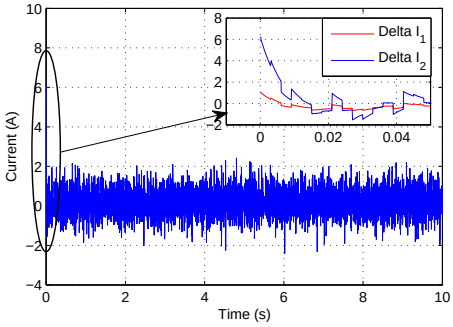

(b) Control effort of the control system

Figure 4.14: Output response and control signals of the PP tracker system

Table (4.2).

The Simulink block diagram of the simulated MIMO tracking system is presented in Fig. 4.13, in which both process and measurement noise are considered in order to validate the simulation of the system. The forward controller gain matrix K_d is calculated based on (2.28). For this application, because the demand values are DC not change with the time so, $A_d(n \times n)$=0, therefore the forward gain matrix K_d is design so that the steady-state tracking error

$$e_{ss} = A - BK_d, \tag{4.27}$$

is reduced as much as possible. However, the stability of the system is governed by the feedback gain matrix K, which is calculated using the Matlab command "place" based on arbitrary closed-loop system poles. It is worth considering that the large magnitude of the closed-loop poles reduces the transient response of the control system and increases the control signal [86]. Therefore, compromising between the system response speed and the control effort should be considered in the choice of the location of the system poles.

Using the following controller gain matrices which are calculated based on the closed-loop poles $(-90 \pm 2i, -95 \pm 1i)$;

$$K(t) = \begin{bmatrix} 0 & 0 & 87.15 & 0 \\ 0 & 0 & 10 & 0 \end{bmatrix}, \text{ and } K_d(t) = \begin{bmatrix} -796.860 & -17.021 & 489.987 & 9.873 \\ -784.551 & -16.895 & -502.291 & -9.987 \end{bmatrix},$$

the step response and the input signals of the tracking scheme are shown in Fig. 4.14(a) and (b) respectively. It is observed from the mini plot of Fig. 4.14(a) that, the PP tracker can achieve a fast and stable response, albeit with unacceptable steady-state error values. The system output $\Delta x(t)$ and $\Delta y(t)$ followed the desired trajectories with no overshoot, a settling time of 0.08 s and 0.07 s, and a steady-state error of 3.5 mm and 0.1 mm respectively.

Regarding the tracker control signals, it can be seen from the mini plot of the input signals response as shown in Fig. 4.14(b), the steady-state control signals of the tracker were reasonable values while the initial values were high, especially for coil2. The system inputs $\Delta I_1(t)$ and $\Delta I_2(t)$ have the same steady-state value of 0.2 A and their initial values are 1 A and 6 A respectively.

It is worth considering that the reason behind the large value of the steady state error is that there are insufficient controller gain elements to make the error identically zero [71].

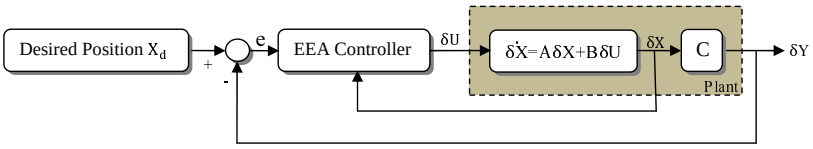

Figure 4.15: Block diagram of the EEA tracker system.

4.2.3.2 Simulation and results of the EEA tracker

The block diagram of the MIMO tracking system based on the EEA approach is shown in Fig. 4.15. In this tracker, the controller is designed to supply the system plant by the gain matrix $\bar{K} = [K_1\ K_2]$ in order to enable the system output to track the desired input $X_d(t)$. The tracking algorithm is based on both the Eigenvalue spectrum of closed-loop plant matrix $\bar{A}_{cl}$, $\sigma\left(\bar{A}_{cl}\right) = \{\lambda_1, \lambda_2, \lambda_3.....\lambda_{n+p}\}$ and an associated set of Eigenvectors $v\left(\bar{A}_{cl}\right) = \{v_1, v_2, v_3.....v_{n+p}\}$ [70],

where $\bar{A}_{cl}$ as mentioned previously in (2.14) is:

$$\bar{A}_{cl} = \begin{bmatrix} A + BK_1 & BK_2 \\ -C & 0 \end{bmatrix}.$$

To evaluate performance of the proposed EEA controller, the tracking system is simulated as shown in Fig. 4.16. As mentioned earlier, the performance of the tracking system is based on Eigenvalues and Eigenvectors of the closed-loop control system. In the proposed EEA controller, the closed-loop Eigenvalues are assigned arbitrarily and then the system performance is investigated based on all its Eigenvectors sets, whose number is given by [87]:

$$N_v = m^{n+p} \tag{4.28}$$

The response and control effort of the tracker based on all the Eigenvectors sets and the optimum set of Eigenvectors under the desired input $X_d(t) = [0\ 0.005]^T$ is shown in Fig. 4.17. The controller gain matrix based on the optimum Eigenvectors

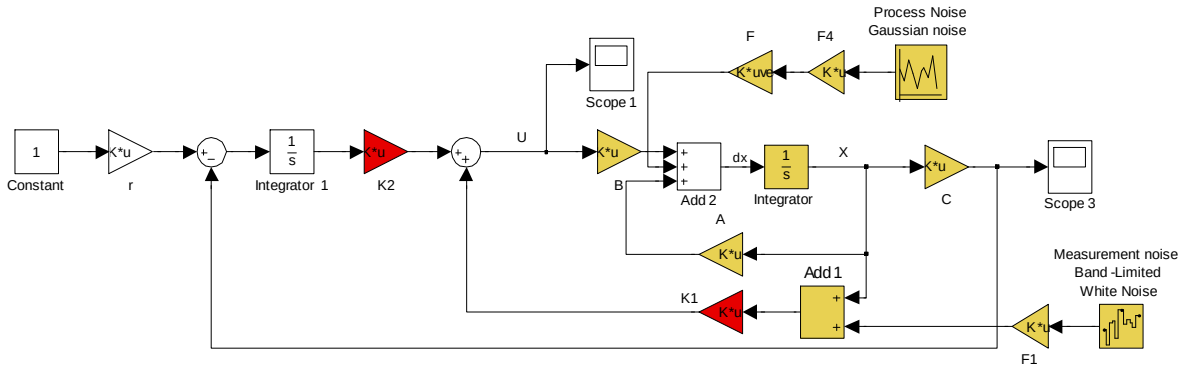

Figure 4.16: Simulink block diagram of the EEA tracker system.

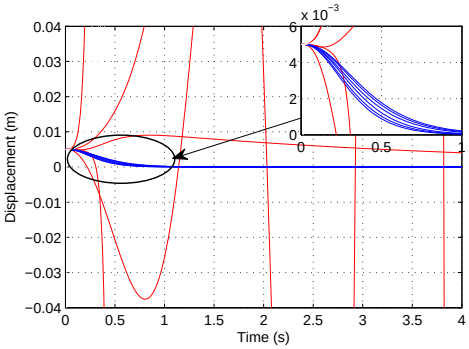

(a) $\Delta x(t)$ response.

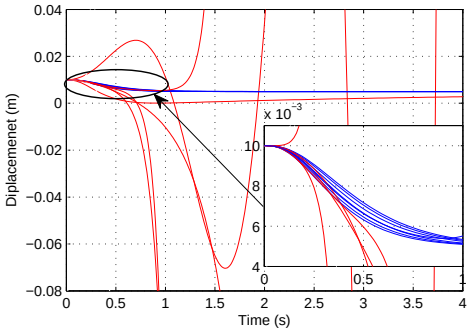

(b) $\Delta y(t)$ component.

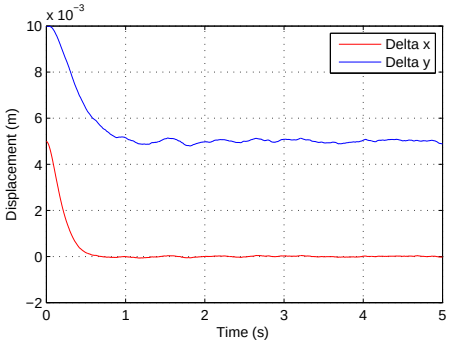

(c) Optimum response.

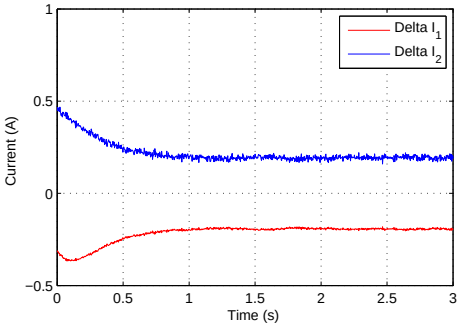

(d) Control effort.

Figure 4.17: Output response and control signals of the EEA tracker system.

set is listed below:

$$K_1 = \begin{bmatrix} 18.3784 & 2.0101 & -47.9474 & -1.2386 \\ 18.3784 & 2.0101 & 47.9474 & 1.2386 \end{bmatrix},$$

$$K_2 = \begin{bmatrix} -31.9792 & 23.2636 \\ -31.9792 & -23.2636 \end{bmatrix}.$$

Fig. 4.17(a) and (b) show the response of the system output $\Delta x(t)$ and $\Delta y(t)$ based on promising Eigenstructure sets respectively. The red responses represent the system output ($\Delta x(t)$ and $\Delta y(t)$) based on unsuitable eigenvectors sets and the blue responses present the system performance based on the acceptable eigenstructure sets. It can be seen that the response of the tracker depends on the Eigenvalues of the closed-loop control system and their associated eigenvectors. Based on the optimum Eigenstructure set, Fig. 4.17(c) and (d) show output response and the control signals of the tracker.

Compared with the PP tracker response, the capsule actuator system based on the EEA controller is improved through keeping the stability and reduction of the steady state error. However, the response time of the system is not fast enough, based on Fig. 4.17(c) the settling times of the $\Delta x(t)$ and $\Delta y(t)$ are 0.5 s and 1 s respectively. Regarding the control effort, it can be seen from Fig. 4.17(d) that the control signals of the system $\Delta I_1(t)$ and $\Delta I_2(t)$ are reduced from 1 A and 6 A to 0.33 A and 0.43 A respectively.

To improve scheme performance, a complex optimization algorithm based on numerical analysis should be applied to assign an optimum set of closed-loop Eigenvalues and Eigenvectors; nevertheless, there is no guarantee of realizing acceptable transient response behaviour based on a reasonable control inputs range [86][88]. Therefore, another controller technique should be adopted to implement the capsule actuation system based on the simplicity of the design and trade off between the performance efficiency and the accepted control effort.

4.2.3.3 Simulation and results of the LQR tracker

Because the proposed system is observable and state controllable, the LQR technique can be used to implement its controller as this approach bases on the full state feedback. The block diagram of the tracking system based on the LQR technique is the same block diagram of the PP control system as previously shown in Fig. 4.12. The LQR controller design includes choosing a control law [71]:

$$\Delta U(t) = Ke(t) - K_d X_d(t) \tag{4.29}$$

where K and K_d are the optimal feedback and non-optimal forward gain matrices respectively and $e(t) = X_d(t) - X(t)$ is the tracking error, which stabilizes the magnet at the desired position while minimizing the quadratic cost function:

$$J = \int_0^\infty \left\{ e^T(t)Q(t)e(t) + \delta U(t)^T(t)R(t)\delta U(t) \right\} d(t), \tag{4.30}$$

where $Q(t)$ and $R(t)$ are the combined state and control penalty matrices respectively. The Simulink model of the LQR tracker system against the same simulation model of the PP tracker scheme is shown in Fig. 4.13. Tracking performance can be investigated by a proper setting of the gain matrices K and K_d which determines the input vector $\Delta U(t)$ and eliminates the steady state error respectively. The controller gain K was calculated based on the LQR matrices $Q(t)$ and $R(t)$, which are set to effectively enable the system states to track the desired inputs while keeping

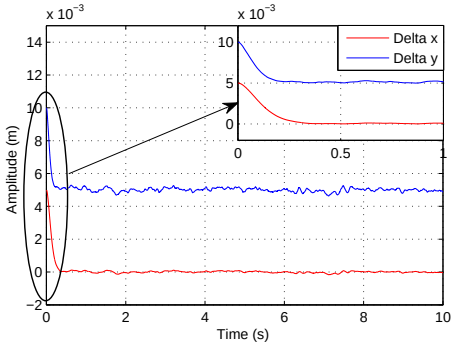

(a) $\delta x(t)$ and $\delta y(t)$ response

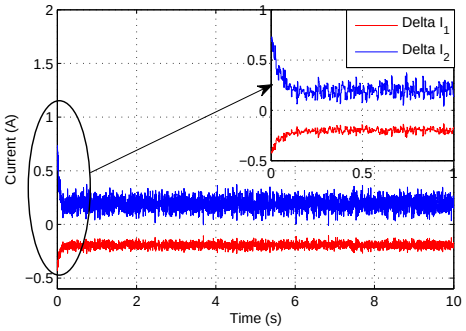

(b) Control effort of the control system

Figure 4.18: Output response and control signals of the LQR tracker system

the control inputs as small as possible.

$$Q(t) = \begin{bmatrix} 9*10^4 & 0 & 0 & 0 \\ 0 & 350 & 0 & 0 \\ 0 & 0 & 20 & 0 \\ 0 & 0 & 0 & 0.05 \end{bmatrix}, R(t) = \begin{bmatrix} 1.1 & 0 \\ 0 & 0.825 \end{bmatrix},$$

$$K = \begin{bmatrix} -26.219 & -3.002 & 73.082 & 3.247 \\ -26.281 & -2.838 & -81.997 & -3.6435 \end{bmatrix}$$

While the forward gain matrix K_d was calculated based on (2.34) as follows:

$$K_d = \begin{bmatrix} 0 & 0 & 38.577 & 0 \\ 0 & 0 & -38.577 & 0 \end{bmatrix}$$

The output response and the control signals of the simulated tracking system based on the above controller parameters are shown in Fig. 4.18(a) and (b) respectively.

It is observed from the mini plot of Fig. 4.18(a) that the controller output $\Delta x(t)$ and $\Delta y(t)$ followed the demand inputs in a short settling time of approximately 0.18 s and 0.27 s respectively with no overshoot, zero steady state error and a minimal system noise of 0.15 mm and 0.25 mm respectively

The mini figure of Fig. 4.18(b) suggests the initial and the steady state control input

of the controller system were within acceptable values. The initial value of the ΔI_1 and ΔI_2 are 0.4 A and 0.7 A respectively, while their steady state values have the same value of 0.2 A.

Based on the above analysis, it can be said that under the assumption of a perfectly matched coil parameters, the LQR controller has achieved a good stability and performance robustness based on Gaussian process noise with mean value of 0 V and variance of 0.24 mV and band-limited white measurement noise with power of 25 μV. Consequently, this approach can be adopted to design the controller of the capsule actuation system. However, practical implementation of the LQR controller, which will be discussed in Chapter 6, has shown that the controller was not able to achieve a stable 2D system.

The reason for this is that the simulation design of the proposed system is simple, as the effect of the capsule orientation on the position feedback, is not considered in the controller algorithm. Therefore, in this research project, a more realistic simulation design for a capsule actuation system will be considered in the next section.

4.3 3DOF Controller Simulation

In this section, the 3DOF capsule navigation system is designed and simulated based on the LQR controller. A positioning feedback system based on coil sensors is used to provide the controller algorithm with capsule position and orientation information.

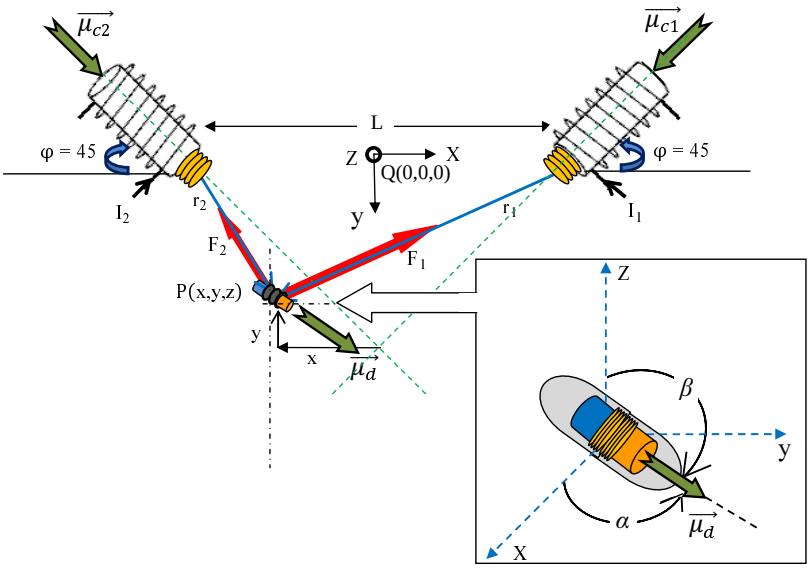

Figure 4.19: Schematic diagram of the 2D control system.

4.3.1 System Configuration and Modelling

4.3.1.1 System configuration

The proposed system has the same configuration and the simulated platform of the 2D controller system as previously shown in Fig. 4.10, except a pair of 3-axis orthogonal coil sensors is used instead of a pair of 1-axis coil sensors. The mutual coil sensors are used to detect the AC magnetic signal generated by the capsule coil, including the device position and orientation information. The sensor outputs are conditioned and then sent to the controller which delivers control signals to the electromagnets in order to guide the capsule through the desired trajectory.

4.3.1.2 System modelling and dynamics

A schematic diagram of the 3DOF controller scheme is illustrated in Fig. 4.19. The coil and dipole moment are governed by (3.2) and (3.22) respectively while the exerted force by the actuators on the inserted magnet is governed by (3.21). Taking these assumptions into consideration, the actuators are orthogonal in the

plane $z = 0$, and so the magnetic moment of the coils can be expressed as follows:

$$\vec{\mu}_{ck} = \mu_c \left[\frac{(-1)^k}{\sqrt{2}} i + \frac{1}{\sqrt{2}} j + 0k \right], \qquad k = 1, 2 \tag{4.31}$$

Assume the initial position of the capsule is close to the plane z = 0 and, therefore, the coils work to drag the dipole to their plane. Then, based on an appropriate controller design the coils can control the magnet's position and orientation in the xy-plane. In the manipulating plane ($z = 0$), the dipole inclination angle $\beta = 90°$ and then the magnetic dipole moment $\vec{\mu}_m$ based on (3.22) becomes as follows:

$$\vec{\mu}_m = \mu_m(\cos(\alpha)i + \sin(\alpha)j + 0k) \tag{4.32}$$

The expression which governs the movement of the embedded magnet in the xy-plane is the same expression used in the 2DOF controller system as previously shown in (4.3.1.2), which is:

$$m\frac{d^2(x(t)y(t))}{dt^2} = \sum_{k=1}^{2} \frac{K_k I_k}{r_k^4} \{(\hat{\mu}_{c_k}.\hat{r}_k)\hat{\mu}_m + (\hat{\mu}_m.\hat{r}_k)\hat{\mu}_{c_k} + (\hat{\mu}_{c_k}.\hat{\mu}_m)\hat{r}_k$$
$$-5(\hat{\mu}_{c_k}.\hat{r}_k)(\hat{\mu}_m.\hat{r}_k)\hat{r}_k\} + W\hat{W},$$

If the coils have the same physical and magnetic parameters, then based on (4.3.1.2), (4.31), and (4.32), the x-direction movement expression of the inserted magnet can

be written as:

$$\begin{aligned}\ddot{x}(t) = \frac{K}{\sqrt{2}m} I_1 \Bigg[& \frac{(-3\cos(\alpha) + \sin(\alpha))X_1 + (\cos(\alpha) - \sin(\alpha))y(t)}{r_1^5} \\ & -5\frac{(-X_1^2 + X_1 y(t))(\cos(\alpha)X_1 + \sin(\alpha)y(t)}{r_1^7}\Bigg] \\ + \frac{K}{\sqrt{2}m} I_2 \Bigg[& \frac{(3\cos(\alpha) + \sin(\alpha))X_2 + (\cos(\alpha) + \sin(\alpha))y(t)}{r_2^5} \\ & -5\frac{(X_2^2 + X_2 y(t))(\cos(\alpha)X_2 + \sin(\alpha)y(t))}{r_2^7}\Bigg],\end{aligned} \tag{4.33}$$

where $K = \frac{3}{4\pi}\mu_r \Re N_c A_c B_i V$, $X_1 = \frac{L}{2} - x(t)$, $X_2 = \frac{L}{2} + x(t)$, $r_1 = \sqrt{X_1^2 + y(t)^2}$, and $r_2 = \sqrt{X_2^2 + y(t)^2}$.

For the linear control system design, the above non-linear dynamic equation is linearized using Taylor's series expansion based on the Jacobian method about an operating point (x_0, y_0,α_0, I_{01}, I_{02}). If $X_{01} = \frac{L}{2} - x_0$, $X_{02} = \frac{L}{2} + x_0$, $r_{01} = \sqrt{X_{01}^2 + y_0^2}$, and $r_{02} = \sqrt{X_{02}^2 + y_0^2}$. Then the linearized model can be described by:

$$\ddot{\Delta x}(t) = C_1 \Delta I_1(t) + C_2 \Delta I_2(t) + C_3 \Delta x(t) + C_4 \Delta y(t) + C_5 \Delta\alpha(t), \tag{4.34}$$

where $C_1 = \frac{\partial(\ddot{x}(t))}{\partial I_1}\Big|_{(x_0,y_0,\alpha_0,I_{01},I_{02})}$, $C_2 = \frac{\partial(\ddot{x}(t))}{\partial I_2}\Big|_{(x_0,y_0,\alpha_0,I_{01},I_{02})}$, $C_3 = \frac{\partial(\ddot{x}(t))}{\partial x}\Big|_{(x_0,y_0,\alpha_0,I_{01},I_{02})}$, $C_4 = \frac{\partial(\ddot{x}(t))}{\partial y}\Big|_{(x_0,y_0,\alpha_0,I_{01},I_{02})}$, and $C_5 = \frac{\partial(\ddot{x}(t))}{\partial \alpha}\Big|_{(x_0,y_0,\alpha_0,I_{01},I_{02})}$. These expressions are included in Appendix B.1.

In the y-direction, the magnetic force exerted on the embedded magnet by the coils

is expressed based on (4.3.1.2), (4.31), and (4.32) as follows:

$$\begin{aligned}\ddot{y}(t) = \frac{K}{\sqrt{2}m} I_1 \Bigg[& \frac{(\cos(\alpha) - \sin(\alpha))X_1 + (3\sin(\alpha) - \cos(\alpha))y(t)}{r_1^5} \\ & -5\frac{y(t)(-X_1 + y(t))(\cos(\alpha)X_1 + \sin(\alpha)y(t))}{r_1^7}\Bigg] \\ + \frac{K}{\sqrt{2}m} I_2 \Bigg[& \frac{(\cos(\alpha) + \sin(\alpha))X_2 + (\cos(\alpha) + 3\sin(\alpha))y(t)}{r_2^5} \\ & -5\frac{y(t)(X_2 + y(t))(\cos(\alpha)X_2 + \sin(\alpha)y(t))}{r_2^7}\Bigg] + g\end{aligned} \tag{4.35}$$

For the linear MIMO controller design, the above non-linear dynamic equation is linearized around the operating point (x_0,y_0,α_0,I_{01},I_{02}) as follows:

$$\ddot{\Delta y}(t) = D_1\Delta I_1(t) + D_2\Delta I_2(t) + D_3\Delta x(t) + D_4\Delta y(t) + D_5\Delta\alpha(t), \tag{4.36}$$

where $D_1 = \frac{\partial(\ddot{y}(t))}{\partial I_1}\Big|_{(x_0,y_0,\alpha_0,I_{01},I_{02})}$, $D_2 = \frac{\partial(\ddot{y}(t))}{\partial I_2}\Big|_{(x_0,y_0,\alpha_0,I_{01},I_{02})}$, $D_3 = \frac{\partial(\ddot{y}(t))}{\partial x}\Big|_{(x_0,y_0,\alpha_0,I_{01},I_{02})}$, $D_4 = \frac{\partial(\ddot{y}(t))}{\partial y}\Big|_{(x_0,y_0,\alpha_0,I_{01},I_{02})}$, and $D_5 = \frac{\partial(\ddot{y}(t))}{\partial \alpha}\Big|_{(x_0,y_0,\alpha_0,I_{01},I_{02})}$. These expressions are provided in Appendix B.2.

The dipole rotation in the xy-plane, which is represented by the angle α, is also governed by Newton's second law, and can be expressed as follows:

$$J\ddot{\alpha}(t) = \frac{L_d}{2}\left[\sqrt{(F_{2x}\sin(\alpha))^2 + (F_{2y}\cos(\alpha))^2} - \sqrt{(F_{1x}\sin(\alpha))^2 + (F_{1y}\cos(\alpha))^2}\right] \tag{4.37}$$

where $\ddot{\alpha}(t)$ is the magnet's acceleration in the α-direction, $J = \frac{m}{12}(3r_d^2 + L_d^2)$ is the moment of inertia of the dipole ($kg\ m^2$), F_{kx} and F_{ky} are the magnetic force components of the coil$_k$ in the x and y-direction respectively. This can be expressed

based on general force expression (3.21), (3.1) (4.31), and (4.32) as follows:

$$F_{1x} = \frac{K}{\sqrt{2}m} I_1 \left[\frac{(-3\cos(\alpha) + \sin(\alpha))X_1 + (\cos(\alpha) - \sin(\alpha))y(t)}{r_1^5} + 5\frac{X_1(X_1 - y(t))(\cos(\alpha)X_1 + \sin(\alpha)y(t)}{r_1^7} \right], \tag{4.38}$$

$$F_{1y} = \frac{K}{\sqrt{2}m} I_1 \left[\frac{(\cos(\alpha) - \sin(\alpha))X_1 + (3\sin(\alpha) - \cos(\alpha))y(t)}{r_1^5} + 5\frac{y(X_1 - y(t))(\cos(\alpha)X_1 + \sin(\alpha)y(t))}{r_1^7} \right], \tag{4.39}$$

$$F_{2x} = \frac{K}{\sqrt{2}m} I_2 \left[\frac{(3\cos(\alpha) + \sin(\alpha))X_2 + (\cos(\alpha) + \sin(\alpha))y(t)}{r_2^5} - 5\frac{X_2(X_2 + y(t))(\cos(\alpha)X_2 + \sin(\alpha)y(t))}{r_2^7} \right], \tag{4.40}$$

$$F_{2y} = \frac{K}{\sqrt{2}m} I_2 \left[\frac{(\cos(\alpha) + \sin(\alpha))X_2 + (\cos(\alpha) + 3\sin(\alpha))y(t)}{r_2^5} - 5\frac{y(X_2 + y(t))(\cos(\alpha)X_2 + \sin(\alpha)y(t))}{r_2^7} \right] \tag{4.41}$$

The Jacobian linearization of the system about the equilibrium point (x_0,y_0,α_0,I_{01},I_{02}) is given by:

$$\ddot{\Delta\alpha}(t) = E_1\Delta I_1(t) + E_2\Delta I_2(t) + E_3\Delta x(t) + E_4\Delta y(t) + E_5\Delta\alpha(t), \tag{4.42}$$

where $E_1 = \frac{\partial(\ddot{\alpha}(t))}{\partial I_1}\Big|_{(x_0,y_0,\alpha_0,I_{01},I_{02})}$, $E_2 = \frac{\partial(\ddot{\alpha}(t))}{\partial I_2}\Big|_{(x_0,y_0,\alpha_0,I_{01},I_{02})}$, $E_3 = \frac{\partial(\ddot{\alpha}(t))}{\partial x}\Big|_{(x_0,y_0,\alpha_0,I_{01},I_{02})}$, $E_4 = \frac{\partial(\ddot{\alpha}(t))}{\partial y}\Big|_{(x_0,y_0,\alpha_0,I_{01},I_{02})}$, and $E_5 = \frac{\partial(\ddot{\alpha}(t))}{\partial \alpha}\Big|_{(x_0,y_0,\alpha_0,I_{01},I_{02})}$.

At the equilibrium point, the change in the magnet position and orientation is zero, so based on (4.33) and (4.35), the control inputs I_{01} and I_{02} of the system at the

steady state point can be calculated using the following equations:

$$I_{01} = -\frac{\sqrt{2}mgA_1}{K(A_1A_3 - A_2A_4)} \tag{4.43}$$

$$I_{02} = \frac{\sqrt{2}mgA_2}{K(A_1A_3 - A_2A_4)}, \tag{4.44}$$

where

$$A_1 = \frac{(3\cos(\alpha_0) + \sin(\alpha_0))X_{02} + (\cos(\alpha_0) + \sin(\alpha_0))y_0}{r_{02}^5} - 5\,\frac{X_{02}(X_{02} + y_0)(\cos(\alpha_0)X_{02} + \sin(\alpha_0)y_0)}{r_{02}^7},$$

$$A_2 = \frac{(-3\cos(\alpha_0) + \sin(\alpha_0))X_{01} + (\cos(\alpha_0) - \sin(\alpha_0))y_0}{r_{01}^5} + 5\,\frac{X_{01}(X_{01} - y_0)(\cos(\alpha_0)X_{01} + \sin(\alpha_0)y_0}{r_{01}^7},$$

$$A_3 = \frac{(\cos(\alpha_0) - \sin(\alpha_0))X_{01} + (3\sin(\alpha_0) - \cos(\alpha_0))y_0}{r_{01}^5} + 5\,\frac{y_0(X_{01} - y_0)(\cos(\alpha_0)X_{01} + \sin(\alpha_0)y_0)}{r_{01}^7},$$

$$A_4 = \frac{(\cos(\alpha_0) + \sin(\alpha_0))X_{02} + (\cos(\alpha_0) + 3\sin(\alpha_0))y_0}{r_{02}^5} - 5\,\frac{y_0(X_{02} + y_0)(\cos(\alpha_0)X_{02} + \sin(\alpha_0)y_0)}{r_{02}^7}.$$

To design a MIMO controller, the system dynamics should be formulated in state space form: let $\Delta X_{(n\times1)}=\left[\Delta x(t)\ \dot{\Delta x}(t)\ \Delta y(t)\ \dot{\Delta y}(t)\ \Delta\alpha(t)\ \dot{\Delta\alpha}(t)\right]^T$ be the state vector of the system, $\Delta x(t)$, $\Delta y(t)$, and $\delta\alpha(t)$ be the controlled output, and $\Delta U_{(m\times1)}=[\Delta I_1(t)\ \delta I_2(t)]^T$ be the control inputs' vector, then the state and output

equation of the system can be written based on (4.34), (4.36), and (4.42) as in (4.45) and (4.46) respectively.

$$\dot{\Delta X}(t) = A\Delta X(t) + B\Delta U(t), \tag{4.45}$$

$$\Delta Y(t) = C\Delta X(t) + D\Delta U(t), \tag{4.46}$$

where

$$A = \begin{bmatrix} 0 & 1 & 0 & 0 & 0 & 0 \\ C_3 & 0 & C_4 & 0 & C_5 & 0 \\ 0 & 0 & 0 & 1 & 0 & 0 \\ D_3 & 0 & D_4 & 0 & D_5 & 0 \\ 0 & 0 & 0 & 0 & 0 & 1 \\ E_3 & 0 & E_4 & 0 & E_5 & 0 \end{bmatrix}, \; B = \begin{bmatrix} 0 & 0 \\ C_1 & C_2 \\ 0 & 0 \\ D_1 & D_2 \\ 0 & 0 \\ E_1 & E_2 \end{bmatrix},$$

$$C = \begin{bmatrix} 1 & 0 & 0 & 0 & 0 & 0 \\ 0 & 0 & 1 & 0 & 0 & 0 \\ 0 & 0 & 0 & 0 & 1 & 0 \end{bmatrix}, \text{and} D = \begin{bmatrix} 0 & 0 \\ 0 & 0 \\ 0 & 0 \end{bmatrix}.$$

4.3.2 Strategy of the Actuation System

The proposed motion strategy for the WCE in the digestive tract includes applying the following steps:

- **Step1**. Move the embedded magnet using the control system in the xy-plane within a small area around the operating point, with the ability to set its azimuth angle (α) to 0° or 90° and keep it at the variable-y desired position.
- **Step2**. Navigate the magnet through the simulated bowel in the x, y, and z-direction with ability to manipulate its inclination angle (β) by moving the actuator frame and/or the patient's bed using the robotic frame manipulator.

Table 4.3: Physical and magnetic parameters of the 3DOF controller system.

Parameter	Value	Parameter	Value
I_{01}	-0.205 A	D_3	0
I_{02}	0.205 A	D_4	318.9488
C_1	-32.6	D_5	0
C_2	-32.6	E_1	8921.5
C_3	693.148	E_2	8921.5
C_4	0	E_3	$-4.318 * 10^5$
C_5	-13.8755	E_4	0
D_1	33.8	E_5	-731.89
D_2	-33.8	K	$4.948 * 10^-7 \frac{N\ m^4}{A}$

4.3.3 Simulation Design and Results

The proposed MIMO tracking system based on the LQR approach was simulated in order to evaluate its performance in tracking the desired trajectories. It is worth considering that increasing the levitation distance and including the capsule rotation angle as a controlled parameter in the control system based on the current physical and electrical parameters increased the control effort exerted by the actuator to unreasonable value. Therefore, the proposed 3DOF control system was optimised in order to run the control system based on acceptable coil currents through using a high permeability core material so that the magnetic field strength factor of the system $\mu_r \Re$ becomes 8.

To further reduce the system control signal, the magnetic force strength between the actuator and the levitating object was increased using a stronger permanent magnet with an intrinsic field strength B_i of 1.5 T.

At the operating point $X_0=[x_0\ y_0\ \alpha_0]^T= [0\ 0.03\ 0^\circ]^T$, the tracker was simulated based on the equilibrium coil currents and the Jacobian matrices elements which were calculated using (4.34), (4.36), (4.42) (4.43), and (4.44). These are listed in Table (4.3).

It is worth noting that it can successfully implement the 3DOF LQR controller for

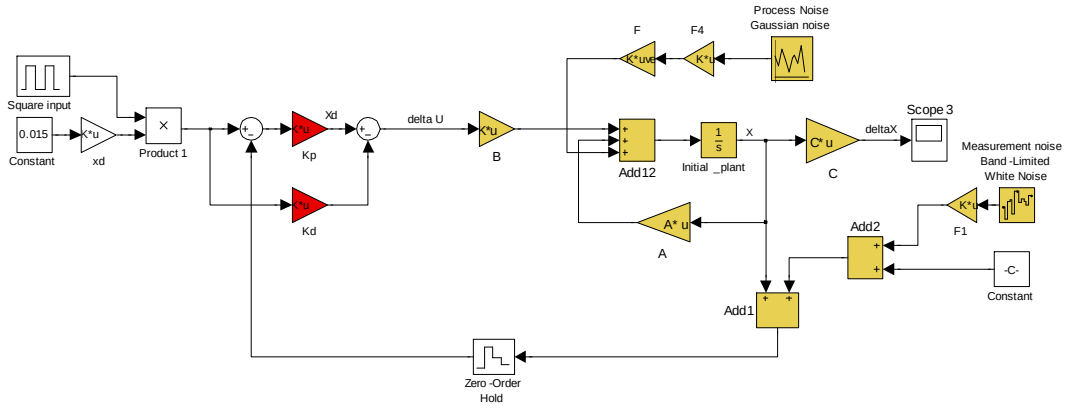

Figure 4.20: Simulink design of the MIMO LQR tracking system.

the proposed actuation system as the system matrices (A,B) and (A,C) are completely controllable and completely observable respectively. Based on the assumption that all the system states are measurable, Fig. 4.20 shows the Simulink model of the 3DOF LQR controller system. At the state and control weighting matrices $Q(t)$ and $R(t)$ which are given:

$$Q(t) = \begin{bmatrix} 10^{12} & 0 & 0 & 0 & 0 & 0 \\ 0 & 75*10^{11} & 0 & 0 & 0 & 0 \\ 0 & 0 & 15*10^{7} & 0 & 0 & 0 \\ 0 & 0 & 0 & 2500 & 0 & 0 \\ 0 & 0 & 0 & 0 & 5*10^{11} & 0 \\ 0 & 0 & 0 & 0 & 0 & 0 \end{bmatrix}, \quad R(t) = 10^{3} \begin{bmatrix} 1 & 0 \\ 0 & 1 \end{bmatrix},$$

the forward and feedback gain matrices are calculated based on (2.32) and (2.34) respectively as follows:

$$K_d = \begin{bmatrix} 0 & 0 & 4.7175 & 0 & 0 & 0 \\ 0 & 0 & -4.7175 & 0 & 0 & 0 \end{bmatrix},$$

$$K = \begin{bmatrix} -305.46 & -61244 & 278.616 & 3.5916 & 15812 & -0.0184 \\ -305.46 & -61244 & -278.616 & -3.5916 & 15812 & -0.0184 \end{bmatrix}.$$

Under the assumption of a perfect match between the coil parameters, using the above LQR controller gain matrices and initial states $[\Delta x_i \ \dot{\Delta x_i} \ \Delta y_i \ \dot{\Delta y_i} \ \Delta \alpha_i \ \dot{\Delta \alpha_i}]^T$

$= [0.01m\ 0\ 0.005m\ 0\ \frac{\pi}{6}\ 0]^T$, the response of the controller output $\Delta x(t), \Delta y(t)$ and $\Delta\alpha(t)$ based on Gaussian process noise with mean value of 0 V and variance of 0.24 mV and band-limited white measurement noise with power of 25 μV, for the following desired input:

$$X_d(t) = \begin{bmatrix} \Delta x_d \\ \Delta\dot{x}_d \\ \Delta y_d \\ \Delta\dot{y}_d \\ \Delta\alpha_d \\ \Delta\dot{\alpha}_d \end{bmatrix} = \begin{bmatrix} 0 \\ 0 \\ f(t) = \begin{cases} 0.01 & \text{for } t\text{=2s,4s,6s,...} \\ 0 & \text{for } t\text{=1s,3s,5s,...} \end{cases} \\ 0 \\ 0 \\ 0 \end{bmatrix},$$

is shown in Fig. 4.21(a), (b), and (c) respectively. The control input of the tracking system is presented in Fig. 4.21(d). The response of the tracking system suggests that, based on acceptable control effort, the controller enables the embedded magnet to be successfully guided through the demand trajectories. Based on the mini figures of Fig. 4.21 (a) and (b), it can be seen that the controller output $\Delta x(t)$ and $\Delta y(t)$ tracked the desired input with a short settling time of approximately 0.225 s and 0.025 s, overshoot of 08% and 0% respectively, and a zero steady state error.

For the dipole rotation angle response, it can be seen from the mini plot as shown in Fig. 4.21 (c) that the LQR controller can provide a response with a very short settling time and minimal steady state tracking error. However, the inserted magnet has an overshoot of 38%, which is considered acceptable proportional to the area of the investigation organ, particularly because its influence on the inspection procedure is little as it happens within a very short transient time of 0.1 s.

Regarding the system control signals, Fig. 4.21 (d) shows that the exciting current of the coils is equal at steady state with an acceptable value which swings between 0.2 A and 2.7 A. It is worth considering that manipulation in the control weighting

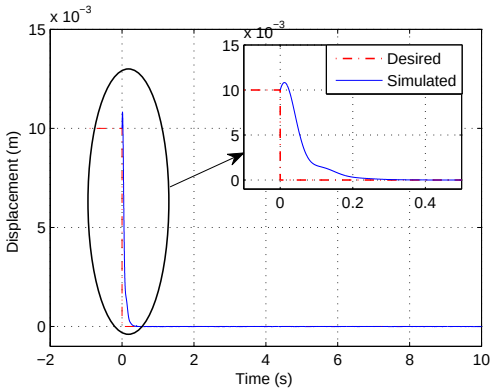

(a) $\Delta x(t)$ response.

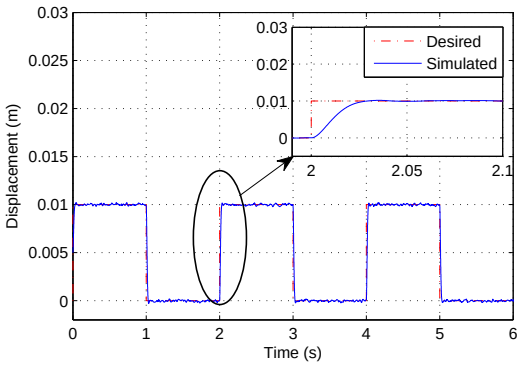

(b) $\Delta y(t)$ response.

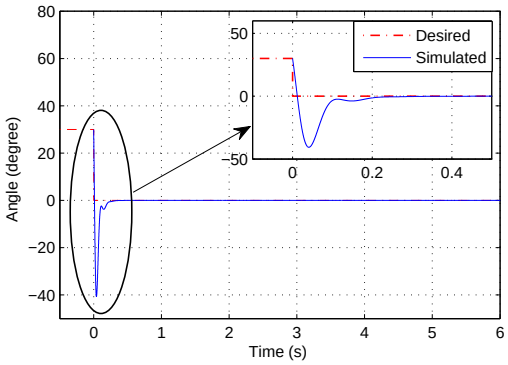

(c) $\Delta\alpha(t)$ response.

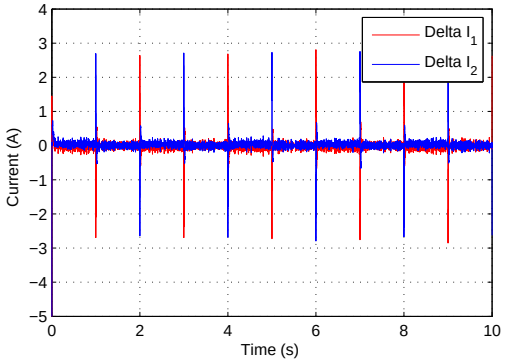

(d) System control signals.

Figure 4.21: Output response and control signal of the 3DOF tracking system.

matrix $R(t)$ could improve the controller response, but this action increases the system control effort which should be as small as possible.

The good performance of the 3DOF LQR controller system encourages its real-time implementation using the DSP in order to validate the simulation results of the

proposed actuation system. In the practical implementation, it is expected that the valid manipulation distance around the equilibrium position is very small due to the linearisation of the high order system modelling terms.

4.4 Chapter Summary

In this chapter, SISO and MIMO actuation schemes are proposed for a capsule endoscope. These systems, which are based on the magnetic levitation concept, are modelled in state space form and hence linear controllers were designed and simulated to realise the system mathematical analysis and validate the proposed approaches.

In the SISO system, the inserted magnet was used for actuation and a marker for localisation. A linear PID controller, based on a Hall effect sensor, was designed to move the embedded magnet in the vertical dimension within an area around the operating point and to maintain it at the desired position.

The proposed 1DOF controller system was then developed through improvements to the capsule position feedback. This improvement included using a coil sensor by which it could obtain the device position information from the AC magnetic field, which was decoupled from the DC actuation fields. Simulation results have shown that, based on reasonable control effort, the controller using both sensing strategies was able to successfully guide the embedded magnet through the desired input trajectory. However, the response of the system based on the coil sensor had the shortest settling time, smallest overshoot value and steady state error.

In the MIMO actuation system, the 2DOF linear PP, EEA, and LQR controllers were designed and simulated for the 2D capsule actuation and finally their tracking performance was compared. Simulation results have shown that, based on acceptable

control inputs, the linear LQR controller had the fastest response with minimal overshoot value and steady state error.

In the last section, a more realistic design for the 2D capsule actuation system was considered by including the capsule rotation angle in the modelling of the system as a controlled parameter. The linear 3DOF LQR controller was designed and simulated to evaluate the developed system. Simulation results have shown that the controller was able to effectively guide the dipole through the desired input trajectory. However, the modelling of the system dynamics includes high order terms which their linearisation process could be valid in the real-time controller implementation just for very narrow region around the operating point.

Chapter 5

Position Sensing

In the area of biomedical applications, suitable fields for a location position scheme are either static or quasi-static magnetic fields. These are suitable because they do not significantly interact with human body tissue. Static magnetic fields are time invariant and produced by either passing a DC current though a loop of wire or permanent magnet. Quasi-static fields are also time invariant and are produced by passing a low frequency AC current through a loop of wire, but otherwise they behave identically to static magnetic fields.

In this research project, these two types of magnetic fields are used to transmit capsule position feedback and the magnetic sensors, Hall effect sensors and coil sensors, are used to detect this magnetic information. Detection of the DC magnetic field by the Hall effect sensor will be discussed in this chapter, along with two types of coil sensors, 1-axis coil sensor and 3-axis orthogonal coil sensor, which are used to sense low frequency transmitted magnetic fields.

5.1 Introduction

A magnetic sensor measures the magnetic field density around it and converts the field to a voltage or current signal. It is widely used in control applications such as determination of an object's position [89]. There are many types of magnetic sensors that can be used to detect magnetic fields, such as search coil sensors, superconducting quantum interference devices (SQUID), fluxgate, magneto-inductive magnetometers, Hall sensors, anisotropic magnetoresistive (AMR), and giant magnetoresistive (GMR) devices, among others [90][91] [92].

Coil magnetic sensors can only detect AC magnetic fields, while the other sensing devices are sensitive to both AC and DC magnetic fields [93]. Of the DC magnetic sensors, Hall effect sensors, AMR, and GMR have the advantages of good linearity, high reliability, small size, ease of realization, and low cost. GMR devices have a precision response, but remnant magnetism exists after it is exposed to a magnet. Therefore, to correct the measurement, an additional de-magnetic coil is needed, and this process makes the implementation of the sensing system complicated. Consequently, the Hall effect sensor and AMR device can be adopted to detect the DC magnetic signal from the embedded magnet for capsule positioning purposes.

It is worth considering that position feedback accuracy based on a DC magnetic field is not high due to interference between positioning and actuation DC fields. In this research project, two positioning approaches based on the Hall effect sensor are used in the localization part of the proposed capsule actuation system which are one Hall sensor and two Hall sensors on the opposit poles of the electromagnet. For more accurate position detection, the coil sensor is adopted for the capsule actuation system due to its simplicity, good response and very low cost. It is used to receive a specific frequency AC magnetic signal from the generating coil attached

Table 5.1: Designed parameters of the proposed electromagnetic coil.

Characteristics	Values
Supply current (I_{cc})	11 mA
Output type	Ratiomateric
Output voltage span	$0.2 - (V_{cc} - 0.3)$
Magnetic sensitivity	2.5 mV/G
Magnetic range	±880 G
Operating ambient temperature (T_A)	−40-125°C
Output linearity	±2.5%
Size	2.9 x 3 x 1mm

to the capsule, so that, by an appropriate algorithm, it can find the position and orientation parameters of the device [21][31][94]. Details of Hall effect sensor and coil sensor will be taken into consideration next.

5.2 Positioning With DC Magnetic Field Measurement

5.2.1 Hall Effect Sensor Descriptions

In the proposed actuation system, positioning of the WCE is based on using of a 1-axis Hall effect sensor. Fig. 5.1 shows the block diagram of a linear Hall effect sensor integrated circuit (IC) (Alergo Microsystem, A1301) employed to measure the position of the WCE [95]. It converts magnetic field, produced by an embedded magnet in the capsule, into electrical signals for processing by electronic circuits. Generally, the output voltage of Hall effect devices can be quite small, even when a strong magnetic intensity is applied, therefore, they are manufactured with built-linear amplifiers and CMOS Class A output structure, not only to reduce the size and improve the sensor's sensitivity, hysteresis and output signal, but also to allow operation over a wide range of magnetic field conditions and power supplies. High

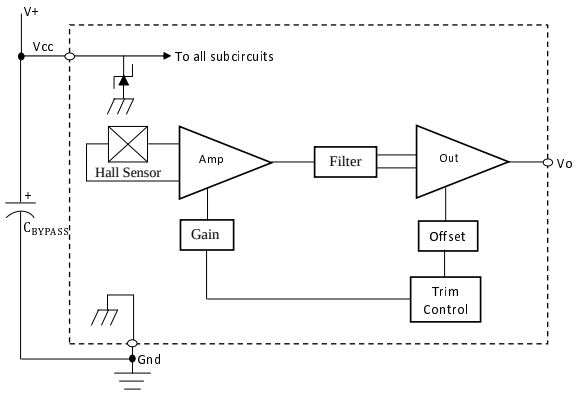

Figure 5.1: Block diagram of A1301 Hall effect sensor [92].

precision in device output levels is obtained by internal gain and offset trim regulations made at the end-of-line during the manufacturing process.

The voltage supply range of the Hall sensor IC is 4.5-6 V. The relationship between the magnetic field sensed by the device and its corresponding voltage output is defined by the transfer characteristics curve as shown in Fig. 5.2 [64]. The ratiometric output voltage is govern by the supply voltage and changes in proportion to the strength of the magnetic field passing through the device. Based on the above characteristics function, it is clear that the device, which has a quiescent out voltage that is 50% of the supply voltage, can respond to either positive or negative fields, monitoring either or both magnetic poles. More details about the electrical, ratiomateric, and magnetic characteristics of the integrated circuit Hall effect sensor are listed in Table (5.1) [95].

In our proposed actuation system, which is based on the magnetic levitation concept, the voltage across the Hall effect sensor (V_o) attached to the coil, induced by the levitating magnet distance x and the electromagnet curring current I, can be closely approximated as [96].

$$V_o = \lambda I + \frac{\varepsilon}{x^2} + \iota, \tag{5.1}$$

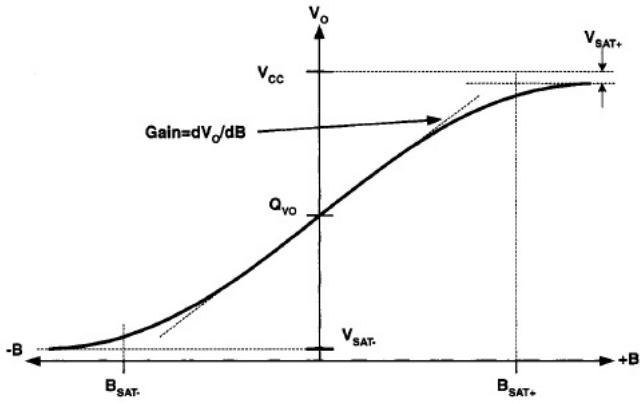

Figure 5.2: Linear Hall effect sensor transfer curve [64].

where the parameters λ, ε and ι are constants that depend on the particular Hall effect sensor used, as well as the geometry of the system, and x is the axial distance between the sensor and the floating magnet (m). Usually, ι is quiescent output voltage ($0.5V_{cc}$) that matches the sensor characteristics curve shown in Fig. 5.2, while λ and ε should be determined from measurement, as they depend not only on the sensitivity of the Hall effect sensor, but also on its location and the properties of the actuator coil.

5.2.2 Positioning Based on One Hall Sensor

5.2.2.1 Experimental setup

The conditioner circuit schematic diagram of the Hall sensor signal is shown in Fig. 5.3. The function of the processing circuit is to prepare the feedback position signal for processing in the DSP. It consists of the following stages:

- **Voltage follower**. This is the unity gain amplifier stage, used to buffer the Hall effect sensor voltage output to enable it to drive the subsequent circuits.

- **Amplification**. This stage, as shown in Fig. 5.3, is based on an inverter amplifier circuit, and its function is to amplify the buffered position signal.

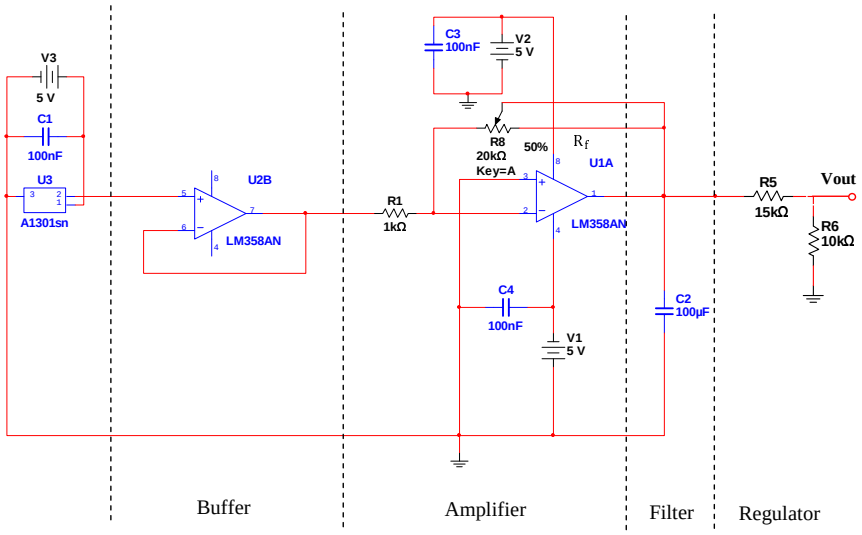

Figure 5.3: Schematic diagram of the conditioner circuit based on single Hall effect sensor.

The gain of the amplifier is given by:

$$G = \frac{-R_f}{R_3}, \tag{5.2}$$

The level of the output signal is governed by the value of the variable feedback resistor R_f. For our application, the position signal is amplified to a level so that we can distinguish the position signal from the sensor noise when the magnet is at the typical operating distance from the actuator coil. The feedback resistor is adjusted until the amplified position signal becomes 5 V when the dipole is placed at a minimum operating distance of 15 mm from the Hall effect sensor.

- **Filtering**. This is a RC low pass filtering (LPF) stage used to reject the high frequency interference. As shown in Fig. 5.3, it is implemented by adding a shunt capacitor C_2 to the output of the differential amplifier which has a low output impedance R_o of approximately 50 Ω. Solving the impedance of the

resistor/capacitor network gives the transfer function of the filter:

$$H(f) = \frac{1}{1 + 2\pi f R_o C_2} \tag{5.3}$$

The cut-off frequency of the filter is given by :

$$f_c = \frac{1}{2\pi R_o C_2}. \tag{5.4}$$

In our application, the cut-off frequency was chosen to be 31.8 Hz, at which a compromise between noise rejection and the system response time is considered. The cut-off frequency was calculated using (5.4) based on the shunt capacitor $C_2 = 100\ \mu$F.

- **Regulation**. This was a simple voltage divider circuit, used to protect the DSP from the position signal with a voltage level higher than its maximum input voltage of 3 V.

5.2.2.2 Hall effect sensor calibration

The position feedback of the embedded magnet was based on the Hall effect sensor, which was calibrated practically using a precision vertical positioning look up table. By keeping the inserted magnet concentric with the magnetic sensor, the calibration was carried out by lowering the dipole from the minimum vertical operating distance, which was 15 mm below the electromagnet, up to 55 mm. The position sensor reading was amplified by a non-inverter amplifier to a level so that we could discriminate the dipole position signal from the sensor noise when the magnet was at the typical operating distance from the actuator coil. The amplified signal was then filtered to reduce noise and sampled using the DSP's on-chip ADC, which was

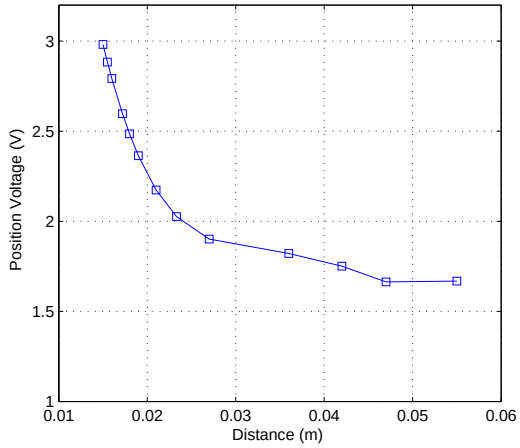

Figure 5.4: Axial displacement versus conditioned magnet position signal based on Hall effect sensor.

calibrated in order to reduce conversion error due to inherent gain and offset errors. To further reduce the influence of noise on the positioning calibration procedure, at each distance step, the dipole position measurement was derived from an average of ten repeated readings. The data curve used to calibrate the vertical dipole position is shown in Fig. 5.4.

To reduce computational complexity and enable real-time controller program execution, the positioning calculation was approximated by a fourth-order polynomial generated using the Matlab command "polyfit". The resulting positioning expression which converts the DSP's ADC reading $Vp(t)$ to the corresponding position $x(t)$ is as follows:

$$x(t) = 0.0574Vp^4(t) - 0.587Vp^3(t) + 2.236Vp^2(t) - 3.77Vp(t) + 2.4 \tag{5.5}$$

To evaluate the performance of the proposed positioning method, the magnet position error was measured based on practical operating conditions. By keeping the magnet at a practical vertical distance 30 mm from the below actuator pole, the coil was excited by a step current of 0.5 A over the current range (0-5) A with the step

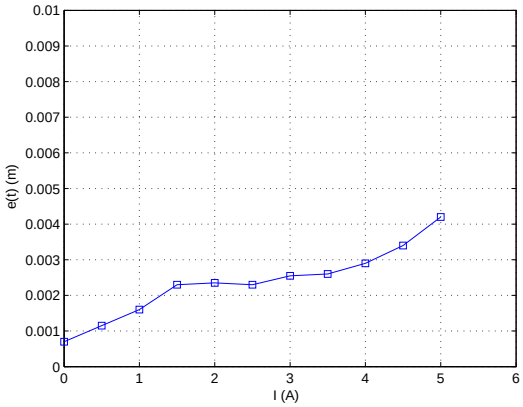

Figure 5.5: Position error based on single Hall effect sensor.

time of 30 s. Over the current range, the practical dipole position was measured based on the (5.5) and then compared with its actual distance 30 mm to generate the position error which is shown in Fig. 5.5. It can be seen from the Fig. 5.5 that increasing the coil current increased the position error. The reason for this is that increasing current heats the coil hence changing the magnetic behaviour of the actuator.

5.2.2.3 Positioning algorithm

In this approach, a magnetic dipole, which is based on a small embedded permanent magnet in the capsule, is used as a magnetic source. The Hall effect sensor is fixed on the lower pole of the actuator, to detect the position signal produced by the dipole. Initially, while keeping the dipole away from the actuator, sensor readings, which are amplified, filtered, and then regulated by a conditioner circuit and finally sampled by the DSP's ADC, are saved in a calibration array in the DSP during the excitation of the actuator by a full PWM range.

During the system operation with the presence of the inserted magnet, a subtraction operation in the DSP is implemented between the sensor signal and its corresponding lookup value for the current PWM value to extract the current dipole position.

The dipole position signal is compared with the demand position to generate an error signal that is sent to the PID controller implemented digitally in the DSP. The output of the controller, which is in the form of a pulse width modulation (PWM) signal with varying duty cycle, is supplied to the current driver circuit which adjusts the current of the coil. However, the positioning efficiency of this procedure drops dramatically as the excitation current increases due to increasing in the power dissipation in the coil which increases the actuator temperature that changes the characteristics and behaviour of the system. To avoid this problem, the following algorithm is used:

5.2.3 Differential Measurement Based on Two Hall Sensors

5.2.3.1 Experimental setup

The conditioner circuit of the position signal is based on two Hall effect sensors shown in Fig. 5.6. The circuit is simply composed of the following stages:

- **Voltage follower**. As mentioned earlier, in the processing circuit of single Hall effect sensor positioning system there is a 2-channels unity gain amplifier stage, used to buffer the output of the Hall effect sensors to enable them to drive the subsequent circuits.

- **Amplification**. This stage, as shown in Fig. 5.6, is used to subtract and amplify the buffered position signals. R_2 is a variable resistor, and used to adjust the zero deviation of the amplifier output, when the embedded magnet is away from the manipulation area, due to mismatch of the sensors characteristics. From the amplifier circuit, it is evident that, the required amplification level of the position signal can be governed by the following equation:

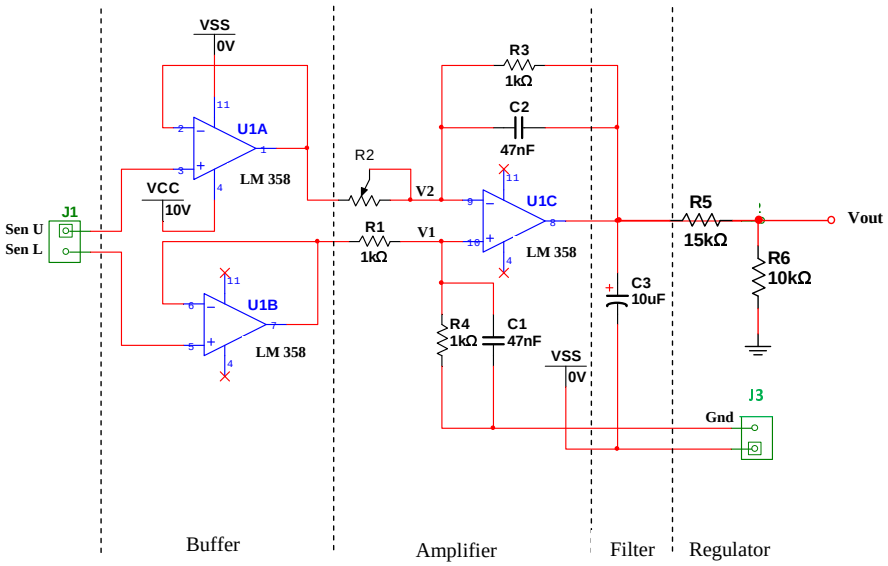

Figure 5.6: Schematic diagram of the conditioner circuit based two Hall effect sensors.

$$V_{out} = \frac{R_3}{R_2}(V_1 - V_2), \tag{5.6}$$

where V_{out} is the output of the amplifier and V_1 and V_2 are buffered voltage outputs of the lower and upper Hall effect sensors respectively. The amplifier resistances are also adjusted so that the amplifier output reaches 5 V when the dipole is placed at a minimum vertical operating distance of 15 mm from the lower Hall effect sensor..

- **Filtering**. This stage, as shown in Fig. 5.6, is a LPF stage which is also implemented by connecting a shunt capacitor across the differential amplifier output. It is used to filter unwanted noise frequencies from the amplified difference voltage signal. Optimum performance of the filter is achieved at a cut-off frequency of 31.8 Hz, calculated using (5.4) based on $C = 100\ \mu$F.

- **Regulation**. This stage as shown in Fig. 5.6 is a voltage divider circuit in which both sensor outputs are scaled down to 3.3 V range.

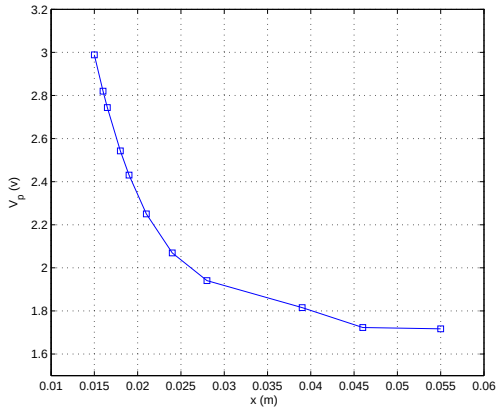

Figure 5.7: Axial displacement versus processed position signal based on Hall effect sensor.

5.2.3.2 Hall effect sensor calibration

The two Hall effect sensors were adopted to provide the actuation algorithm by position feedback; however, with this positioning method, only below magnetic sensor is calibrated based on the same calibration procedure mentioned in the section (5.2.2.2). The data curve used to calibrate the vertical dipole position is shown in Fig. 5.7. To reduce computational complexity and enable real-time controller program execution, the positioning calculation was approximated by a fourth-order polynomial generated using the Matlab command "polyfit". The resulting positioning expression which converts the DSP's ADC reading to the corresponding position $x(t)$ is as follows:

$$x(t) = 0.093Vp^4(t) - 0.93Vp^3(t) + 3.476^2Vp(t) - 5.754Vp(t) + 3.585 \tag{5.7}$$

The fit of the above equation to the measured readings practically has a zero mean error with a standard deviation of $\sigma = 0.32$ mm. For simulation purposes, the position voltage signal $Vp(t)$ based on the vertical dipole position $x(t)$ can be formulated

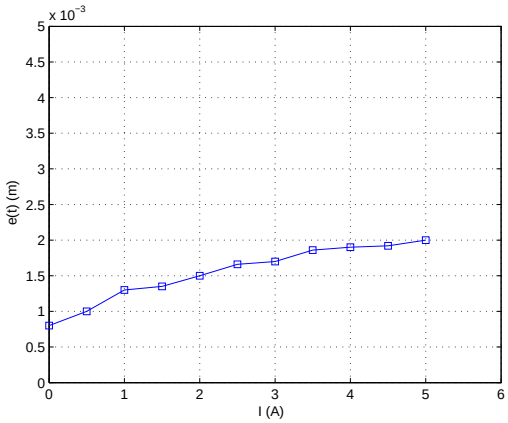

Figure 5.8: Position error based on two Hall effect sensors.

as follows:

$$Vp(t) = 3.217 * 10^6 x^4(t) - 5.1 * 10^5 x^3(t) + 2.965 * 10^4 x^2(t) - 769.1x(t) + 9.41 \quad (5.8)$$

To evaluate the performance of the positioning approach, based on the same error measurement procedure mentioned previously in section (5.2.2.2), the dipole position errors were measured and are shown in Fig. 5.8. It is obvious from Fig. 5.8 that there was an important reduction in the position error based on the two Hall effect sensor position method, due to cancellation of the problems of heating the coil. However, there were still some differences between the actual and the measured dipole positions. The reason for this is that it very hard to achieve a perfect cancellation for the actuation field due to problems of mechanical tolerance, thermal drift, and the winding distribution of the actuator.

5.2.3.3 Positioning algorithm

In this algorithm, the inserted magnet is still used as a marker for positioning, and two Hall effect sensors attached to the pole faces of the coil are used to measure the position signal of the suspended magnet. Magnet position detection as demonstrated in Fig. 5.9 is based on the idea that the upper sensor measures the magnetic field of

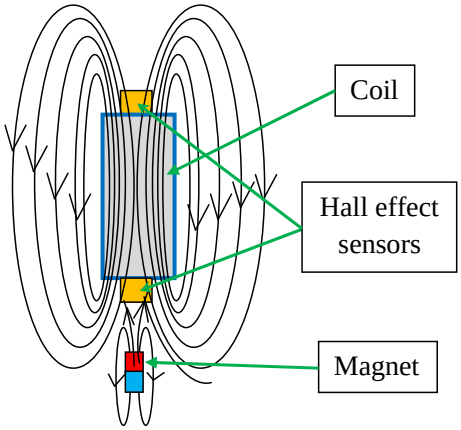

Figure 5.9: Magnet's field detection approach.

the electromagnet, while the lower sensor senses the magnetic field for both the coil and the dipole. The position signal of the floating object is determined by measuring its position with the two Hall effect sensors, and then these position signals are sent to the signal conditioner circuit as shown in Fig. 5.6.

In this circuit, the low current position signals are buffered by a voltage follower circuit, subtracted and amplified by a differential amplifier and finally filtered to reject interference and sensor noises. The processed position signal is also passed to the DSP for sampling and PID controller implementation, and finally the PWM processor output with varying duty cycle is used to regulate the electromagnetic current. This positioning approach needs a high degree of accuracy, not only in coil geometry design and manufacturing, but also in coil winding, in order to obtain a symmetric magnetic field distribution around the coil which will enhance the accuracy of the position feedback information of the capsule.

It is worth considering that positioning methods based on both one and two Hall effect sensors on the opposite poles of the actuator can be adopted to measure the dipole position, however, the accuracy of the positioning system based on single Hall effect sensor on the lower pole of the coil influences by changing of the actuator magnetic behaviour due to rise its temperature at high exciting current values. On

the other side, the two sensors positioning system is still not an efficient positioning system as the sensors measurements influence by the problem of the DC actuation field cancellation. Therefore, another positioning approach based on an AC magnetic field will be considered in the next section.

5.3 Positioning With AC Magnetic Field Measurement

5.3.1 Coil Sensor Background and Descriptions

Coil sensors are one of the oldest and most well-known types of magnetic sensor. It is practically the only sensor that can be manufactured directly by a user (in comparison to Hall, magnetro sistive or flux-gate type sensors). There are two types of coil sensors (either with air cores and ferromagnetic cores). The response function of air core coil sensors is easy to characterize by Faraday's fundamental law of induction, as follows:

$$V = -N_s \frac{d\Phi}{dt}, \tag{5.9}$$

where V is the induced voltage (V), N_s is the number of coil turns, and Φ is the magnetic flux passing through a coil sensor. The above expression refers to the fact that induced voltage in a N_s turn coil winding is equal to the rate of change of electromagnetic flux, the concept which inductive transducers use for measurements. Generally, the sensitivity of an air coil sensor is relatively low so to improve the output response a ferromagnetic core with high permeability should be used. Based on the above equation the output voltage of an iron-cored coil sensor is governed

by:

$$V = -\mu_0 \mu_R N_s A \frac{dH}{dt}, \tag{5.10}$$

where A is the cross-sectional area of the coil sensor (m^2), H is the magnetic field intensity ($\frac{A}{m}$), and μ_R is the resultant permeability of the core which is:

$$\mu_R = \frac{\mu_r}{1 + DF(\mu_r - 1)}, \tag{5.11}$$

where μ_r is the relative permeability of the iron core of the coil sensor and DF is the demagnetization factor, which depends on the geometry of the iron core. However, this enhancement is accompanied by the sacrifice of one of the most important advantages of the air core coil sensor which is the linearity. The core, even if made from highly permeable ferromagnetic material, adds some nonlinear factors to the transfer function of the coil sensor, which depends on temperature, frequency and flux density, among others. Furthermore, the resolution of the coil sensor also decreases by additional magnetic noise (e.g. Barkhausen noise). Moreover, the ferromagnetic core alters the distribution of the investigated magnetic field, which can have important consequences [90]. Therefore, in this study, an air-cored coil sensor will be adopted for capsule positioning. How its sensitivity can be improved will be discussed later in this section.

The equation (5.10) can be simply stated as follows [97]:

$$V = -N_s(\pi r_s^2)\frac{d(B)}{dt} \propto N_s r_s^2 f, \tag{5.12}$$

where r_s is the radius of the coil sensor (m) and dB/dt is the change of magnetic field which is linearly proportional to the coil exciting frequency,f. For control and measurement, what is needed is a magnetic sensor with high sensitivity, adequate

stability and reliability. Based on the above equation, an increase in the number of turns of the coil sensor can be adopted to improve its output sensitivity. However, this process will increase the coil resistance as the total length of wire increases, hence increasing in resistance noise.

Following the scaling rules outlined, [98] [97], if the overall coil physical dimensions are maintained constant then the cross-sectional area of the sensor winding wire must be reduced proportionally to N_s by using a different wire gauge. The resistance for a given geometry is then $2\pi r_s N_s^2$. If the coil size is reduced by decreasing all its physical dimensions (including wire diameter) proportionally to r_s, then the active resistance of the coil sensor will scale according to:

$$R = \frac{2\pi N_s^2}{r_s}, \tag{5.13}$$

The sensitivity of a coil sensor is limited by Johnson noise given by:

$$V_{noise} = \sqrt{4K_B T R \Delta f} \propto \frac{N_s}{\sqrt{r_s}} \tag{5.14}$$

where K_B is Boltzmann's constant in joules per kelvin ($\frac{J}{K}$), T is the coil resistor's absolute temperature (K), and Δf is the bandwidth (Hz) over which the noise is measured. Then the signal-to-noise ratio SNR of an inductive coil for a given geometry is independent of the number of coil turns N_s but depends on the physical dimension, r_s , of the coil:

$$SNR = \frac{V}{V_{noise}} \propto r_s^{\frac{5}{2}} f \tag{5.15}$$

Because the SNR of coil sensors reduces rapidly with reduction in coil size, and also decreases linearly with exciting frequency, therefore, coil sensors become less effective for both low frequency and high resolution applications.

In practice, the coil sensor must have sufficient windings in order to obtain sufficient signal amplitude so that the system performance is not affected by amplifier noise. Optimal coil sensors are still wound by user hand or by machine from copper wire. However, the optimization process for coil sensor performance, in many cases, is not as easy [90].

5.3.2 Coil Sensor Design

Because the coil sensor is placed outside the human body on the actuator pole, there is no limitation in the geometry and the number of turns parameters of the coil sensor. Consequently, these parameters can be manipulated in the design of a high sensitivity coil sensor. In this research project, the coil sensor was designed with a diameter of 40 mm and 50 turns with a 38 American wire gauge (AWG) copper wire.

5.3.3 Positioning With 1-Axis Coil Sensor

This section presents the hardware design and experimental setup of the transmission and receiving stages for the 1D AC position signal.

5.3.3.1 Position signal transmitter

The main part of the AC position signal transmission is the generating coil, which is a magnetic coil wound around the capsule body. The schematic diagram of the electronic circuit for the signal generation and driving of the transmitter coil is shown in Fig. 5.10. It consists of a simple oscillator, driving amplifier, and series LC resonant circuit. For the generator part, a square wave signals with a specific frequency can be generated by programming a logic unit within the capsule body.

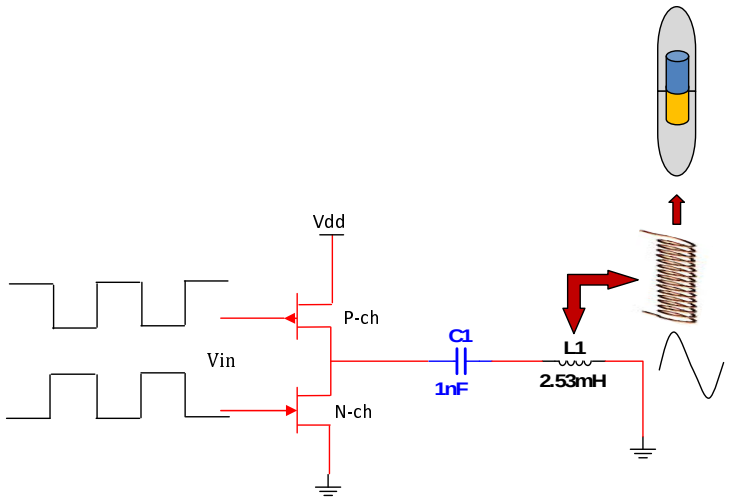

Figure 5.10: Transmission circuit of AC position signal.

To support the exciting signal, a simple class D amplifier, which is commonly used in transmitter circuits, is used to amplify it so that it can drive the LC circuit.

To generate a high power AC coupling signal, the current of the LC circuit should be maximum. The LC circuit is designed to work at a resonant frequency at which the impedance of the circuit is zero, as the capacitor and inductor reactances are equal in absolute value.

The resonant frequency of the LC series resonant circuit is given by:

$$f_o = \frac{1}{2\pi\sqrt{LC}}, \tag{5.16}$$

where L is the inductor of the generating coil (H) and C is a capacitor included in the internal components of the capsule (F). Exciting the coil with AC current provides an accurate capsule position information through detecting the generated AC magnetic field, which is decoupled from the DC actuation fields, by a suitable sensor. The transmitted signal level is governed by the amplitude and frequency of the exciting signal and the generating coil parameters, which include the number of turns, coil size, and core material. The transmitted signal must be of a value so that the sensor coil can receive an adequate AC signal from the generating coil over

the entire positional range of the system.

The frequency of the transmitted signal should not be of a high value if damage to human tissue is to be avoided, meaning that the operating frequency is 100 kHz. The only capsule coil parameter that can be manipulated is the number of turns, since the generating coil is attached to the capsule, which means using a high permeability core and increasing the coil size are impossible. In our application, the AC magnetic source is made with 20 turns of AWG 20 copper wire. The inductance of the coil is 2.53 mH, at resonant frequency 100 kHz; the capacitor should be inserted in the capsule based on (5.16) is 1 nF.

5.3.3.2 Position signal receiver

In this section, two proposed receiver circuits based on analog and digital detectors are designed and experimentally implemented. These circuits were used to extract the capsule position signal and then send it to the PID controller in the DSP, which delivers the control signals required to move the device to the desired position and keep it there.

Analog detector

The detector was used to provide an envelope of the position signal and combined of the following stages:

- **LC circuit**. This is a resonant circuit, and is used to pick out the specific frequency magnetic coupling signal induced by the coil sensor corresponding to the AC magnetic field signal from the generating coil. The parallel LC circuit acts as a band pass filter (BPF) circuit with a centre frequency of f_o. The schematic diagram of the circuit is shown in Fig. 5.11. The circuit is designed to work at a resonant frequency at which the reactances of the coil inductor

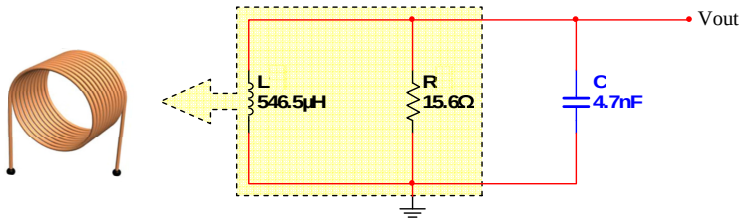

Figure 5.11: Schematic diagram of RLC BPF.

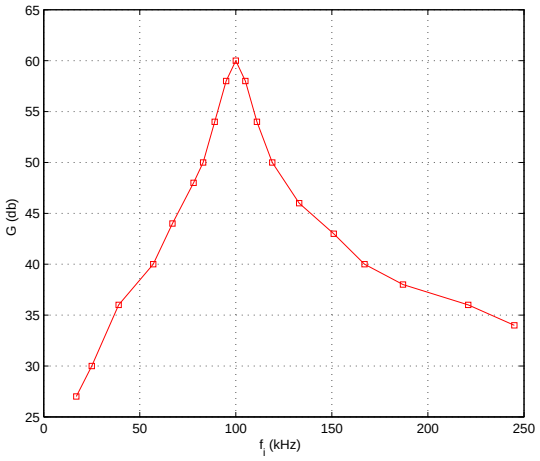

Figure 5.12: Frequency response of the RLC BPF.

L and the capacitor C cancel each other, and hence maximum current passes in the circuit. This occurs at:

$$f_o = \frac{1}{2\pi\sqrt{LC}} \tag{5.17}$$

For our application, the resonance frequency is $f_o = 100$ kHz, then based on the above equation, the capacitance $C = 4.7$ nF.

Using the designed parameters, the frequency response of the filter under input signal V_{in} of 10 $Vp-p$, and frequency f_i sinusoidal signal for input frequency range $f_i = 0 - 250$ kHz is illustrated in Fig. 5.12.

It is evident from the LC circuit response that the filter passed the bandwidth frequencies (B.W=93 − 107) kHz, which are between the upper and lower −3 db points, and reject all the frequencies outside this range. To further

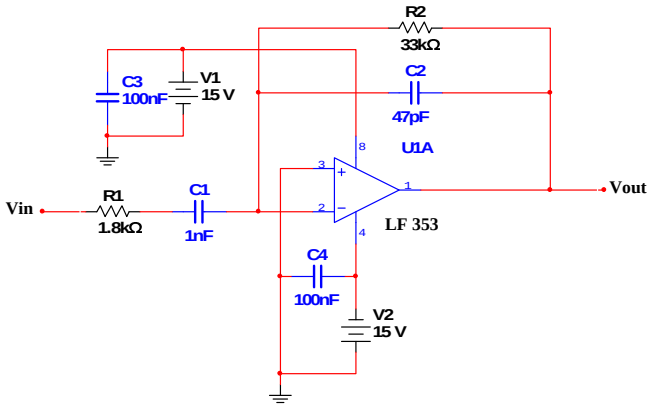

Figure 5.13: Schematic diagram of inverting BPF circuit.

reject unwanted frequencies, a robust BPF should be applied which will be discussed in next section.

- **Active BPF**. This is a type of active BPF based on an inverting operational amplifier which can perform two functions, amplification and filtering, at the same time. The schematic diagram of the circuit is shown in Fig. 5.13. Basically, it is used in electronic systems to separate a signal at one particular frequency from signals at other frequencies. It can be easily implemented by cascading together a single LPF with a single high pass filter (HPF). The filter is designed to have a much narrower pass band. The gain, centre frequency and bandwidth of the filter are governed by the values of the components R_1, R_2, C_1, and C_2. The filter gain is 18 which is calculated as follows:

$$G = -\frac{R_2}{R_1}, \tag{5.18}$$

The lower and the upper cut-off frequencies f_{c1}, f_{c2} at -3 db points are follows:

$$f_{c1} = \frac{1}{2\pi R_1 C_1}, \tag{5.19}$$

$$f_{c2} = \frac{1}{2\pi R_2 C_2}. \tag{5.20}$$

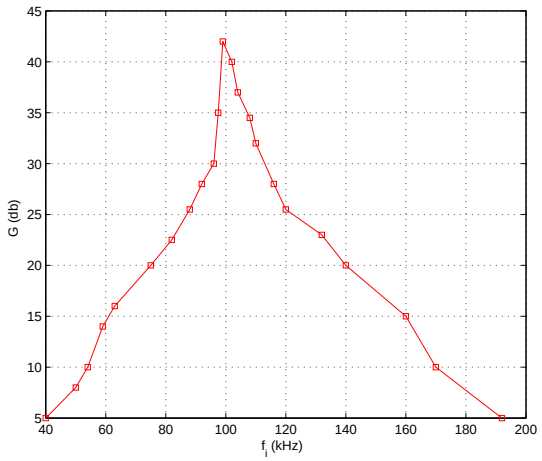

Figure 5.14: Frequency response of the Inverting BPF.

To design a high pass sub-filter, let $f_{c1} = 90$ kHz and $C_1 = 1$ nF, then based on (5.19), the resistor $R_1 = 1.76$ kΩ. For a low pass sub-filter design, in this research project, $G = 18$ then, using (5.18), the resistor $R_2 = 31.68$ kΩ, and for $f_{c2} = 110$ kHz, the capacitor C_2 value based on (5.20) is 47 pF.

Based on the designed filter parameters, the frequency response of the active BPF is shown in Fig. 5.14. It should be noted that the band of the passed frequencies becomes narrower (B.W=$98.2 - 102.5$) kHz, which means an extra attenuation for unwanted frequencies has been achieved that will increase the accuracy of the position signal.

- **Rectifier**. The schematic diagram of the rectifier circuit is shown in Fig. 5.15. It is used to rectify the AC position signal even if its amplitude is as low as 100 mV due to the op amp's ability to compensate for non-linear devices in the feedback loop. This circuit considers a precision rectifier as it combines the rectifying action of the diodes with the accuracy of the op amp. This rectifier circuit must be followed by a LPF circuit, which will be discussed in the next section, in order to create a DC signal.

- **LP filtering**. This stage is a first order LPF which follows the rectifying

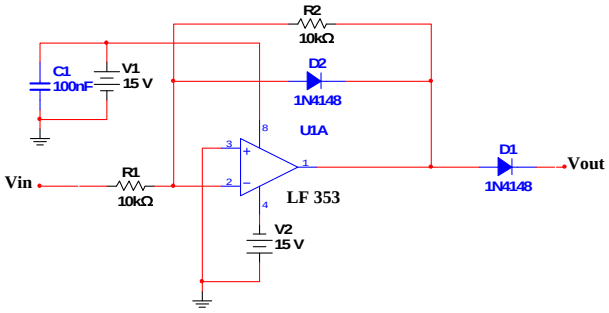

Figure 5.15: Schematic diagram of the rectifier circuit.

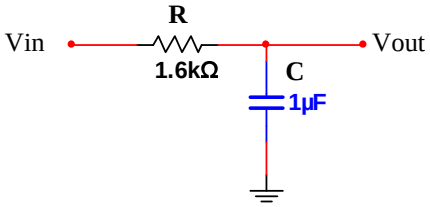

Figure 5.16: Schematic diagram of the LPF circuit.

circuit and its function is to reject unwanted low frequencies mixed with the rectified signal. The smoothing of the filtered signal depends on how low the filter cut-off frequency is. Therefore, getting a signal closed to the DC requires the reduction of the cut-off frequency to minimal value; however, this action leads to an increase in the response time of the system. Consequently, a compromise between the smoothing of the filtered position signal and system response time should be considered in the design of the filter. The schematic diagram of the filter is shown in Fig. 5.16, and its transfer function is given by:

$$H(f) = \frac{K_f}{1 + 2\pi RC}, \tag{5.21}$$

where K_f is the filter passband gain. The filter cut-off frequency is as follows:

$$f_c = \frac{1}{2\pi RC}, \tag{5.22}$$

In this research project, the smallest compromised cut-off frequency is $f_c = 4$ Hz, which is based on the designed component values $C = 1\ \mu F$ and $R =$

1.6 kΩ. It is worth considering that the filtered position signal is not smooth enough as it includes some ripples and low frequency noise signals. To enhance smoothing the signal, another filtering process is considered necessary.

- **Regulator**. This was the same regulation circuit of the position signal based on the Hall effect sensor, as previously shown in Fig. 5.3 and Fig. 5.6. It was used to regulate the filtered position signal before sending it to the DSP for processing.

Digital detector

The digital receiver offers an efficient method for reducing the position noise based on coherent detection. The detector is composed of the following stages:

- **Analogue front end**. This circuit includes LC and active BPF stages which are the same stages as the analog detector.

- **Digital coherent detector**. For more active reduction of noise on the position signal while keeping the response time of the system within an acceptable rate, a digital noise rejection based on the 1-bin discrete Fourier Transform (DFT) was applied in the DSP. Using digital filtering based on coherent detector is a most effective way to achieve very narrow band filter and amplitude detector. In our research project, the centre frequency of the implemented band pass filter based on digital coherent detector is 100 kHz. Generally, the implementation of the digital detector in the DSP system includes the following advantages:

    1. Its implementation does not add noise to the system as a result of its hardware components.

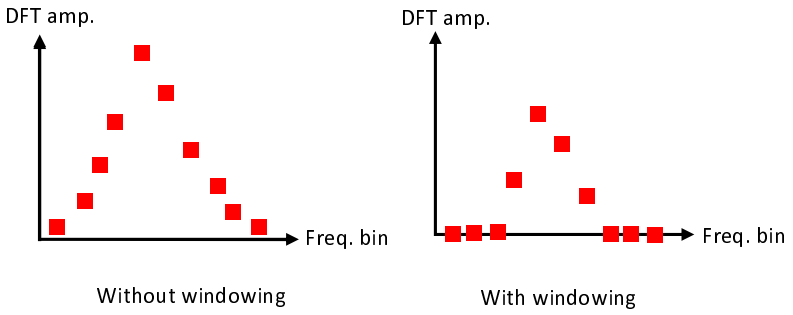

Figure 5.17: Windowing effect on DFT response.

2. Its performance can be easily improved or optimized by just manipulating the related software.

Generally, the use DFT alone can not completely eliminate unwanted interference at other frequencies from outside sources. However, it can vastly reduce their amplitude with a suitable window function. Fig. 5.17 shows the influence of windowing in spectrum frequency of the sampled data. Many window functions are commonly used in narrow-band applications, e.g. Hamming and Hanning windows, which are selected based on how the DFT output is used. Scope DSP utility is considered one of the best and most dependable ways to acclimatise to DFT Windowing in which, on the same data waveform, different window functions are applied, and the resulting spectrum is observed.

IQ is used to denote the complex format on which the position signal is stored, with I and Q as the In-phase and Quadrature components of the position signal. In the digital filtering procedure, the detected signal of the coil sensor, after passing the buffering and active filtering stages mentioned earlier, is sent through a protection circuit to the DSP. The conditioned signal is sampled using the DSP's ADC with a sampling frequency of $f_s = 400$ kHz for the integration time $T_w = 0.25$ ms, i.e 100 sample, and saved in an array in the DSP. Then, a quadrature mixing operation, whose block diagram is presented

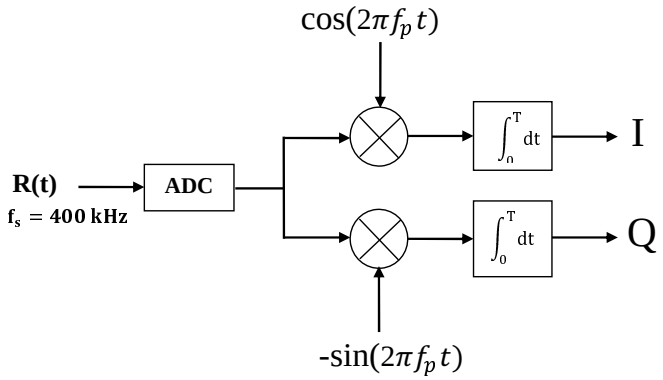

Figure 5.18: Quadrature mixing with sinusoidal signals.

in Fig. 5.18, is achieved in the DSP to produce I and Q format arrases.

In this operation, the saved sampled data are multiplied by a complex vector based on a sinusoidal signal with the same frequency as the position signal. The vector is one unit in length in order to ensure that the energy content of the position signal is not changed. Finally, the envelop detection of the sampled data can be obtained by the following equation:

$$V_{signal} = \frac{1}{2}\sqrt{I^2 + Q^2}, \tag{5.23}$$

(Appendix C.2 provides more detail of this with a flowchart of the digital filter implementation). Calculation of the waveform envelope can, at times, be a heavy computational load on the fixed point used processor. Therefore, in our application, the computational operation of the filtering algorithm was optimised through setting the sampling frequency of the coherent detector to $4f_p$, by which only the odd multiples between position and sinusoidal vector samples were implemented; because the even samples of the sinusoidal signal were zeros, this action saved half the computational time.

Fig. 5.19(a) and (b) show the contrast effect before and after the digital filtering, respectively. The responses suggest the ability of the filter to suppress

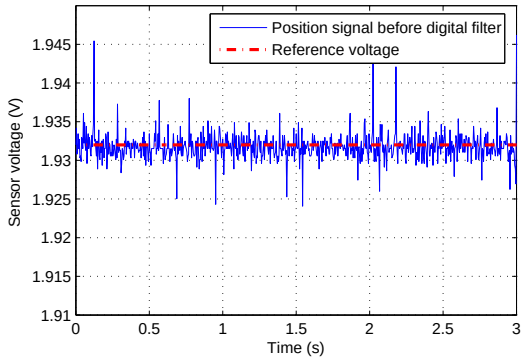

(a) Before digital filtering.

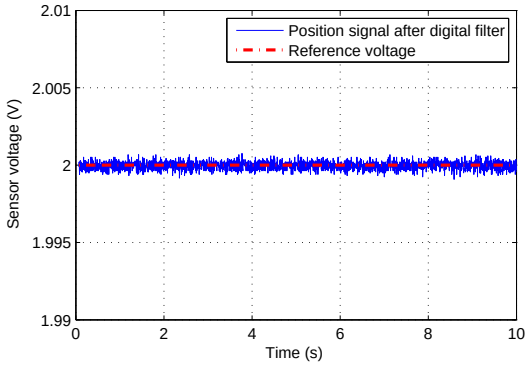

(b) After digital filtering.

Figure 5.19: Coil sensor response before and after digital filtering based on coherent detector.

impulsive noise quite well through its narrow band and perfect envelop detection. This superior performance of the filter is based on its narrow-passing band and perfect envelop detection. The fluctuation of the position signal around the desired value has been reduced by the digital filtering from 0.0125 V to 0.002 V, based the coil sensor calibration curve, which will be discussed in the next section, corresponds to 1.5 mm and 0.25 mm respectively.

5.3.3.3 Coil sensor calibration

As with the control system based on the DC position feedback, to validate the system simulation, the position sensor, which was adopted to the coil sensor, was also

calibrated practically. Basically, the magnetic torque exerted by the electromagnet on the embedded magnet works to set the dipole aligned with the magnetic actuation source; therefore, the calibration was based on that and the inserted magnet was concentric with the coil. The calibration procedure starts by exciting the generating coil directly from the power supply by a low frequency AC signal, and then taking the coil sensor readings for a vertical distance range $15 - 55$ mm. The AC position readings were amplified and filtered by the conditioner circuit in order to reject the position noise. The hardware filtered signal is then sampled by the DSP's ADC. The position noise is also reduced by implementing a mean filter in the processor. To further reduce the influence of the position noise, the sampled signal was filtered digitally based on a coherent detector in the DSP. Fig. 5.20 shows the data curve which was adopted to calibrate the vertical capsule position. In this research project, the sensor calibration curve was used to calculate the position feedback for both system simulation and real-time implementation in order to support realism of the simulation design. To reduce the computational load of the controller algorithm implementation in real-time, the calculation process of the capsule position was also, as in the DC position feedback-based controller system, approximated by the following expression which was used to convert the DSP's ADC reading $Vp(t)$ to the corresponding position $x(t)$.

$$x(t) = -0.4Vp^5(t) + 4.8Vp^4(t) - 22.3Vp^3(t) + 52.3Vp^2(t) - 60.8Vp(t) + 28.2 \quad (5.24)$$

For purposes of system simulation, based on the vertical capsule position $x(t)$, the position voltage signal $Vp(t)$ can be formulated as follows:

$$Vp(t) = 3.0396 * 10^6 x^4(t) - 4.83 * 10^5 x^3(t) + 2.84 * 10^4 x^2(t) - 743.5x(t) + 9.22 \quad (5.25)$$

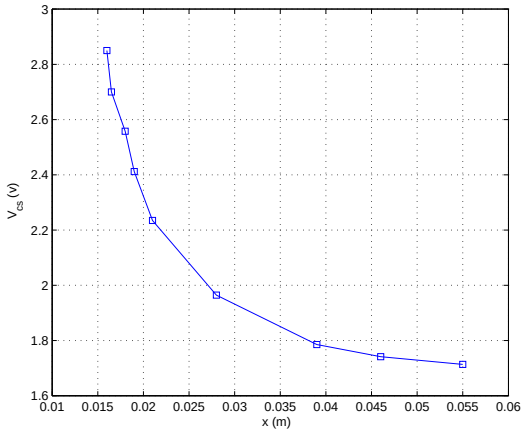

Figure 5.20: Axial displacement versus processed position signal based on coil sensor.

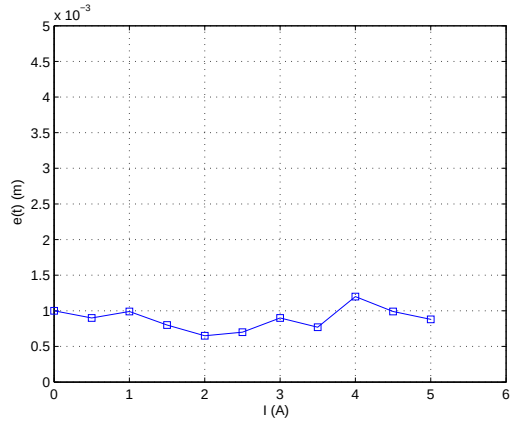

Figure 5.21: Position error based on coil sensor.

To assess the performance of the positioning approach, again based on the same error measurement procedure mentioned previously in section (5.2.2.2) and (5.2.3.2), the magnet position was calculated using (5.24), and based on the actual position signals, the position errors were calculated and are finally shown in Fig. 5.20. It should be noted from Fig. 5.21 that, based on the coil sensor, there was a very important reduction in the position error achieved compared with the previous positioning methods. The reason for this is that the position signal was obtained from an AC magnetic signal which was effectively discriminated from the DC magnetic actuation fields. However, there was a difference between the actual and measured positions due to the approximation of the Matlab position expression (5.24).

5.3.3.4 Positioning algorithm

This algorithm is based on the idea that the capsule position information is transmitted in the form of an AC magnetic field in order to decouple it from the DC actuation field. An oscillator circuit is included in the capsule's components and used to supply a single loop generating coil fixed on the external surface of the device by a low frequency signal.

The AC coupling signal is detected by a coil sensor placed on the close pole of the coil. The position signal, as mentioned in the experimental setup, is amplified, filtered and then regulated by the conditioner circuit. The processed signal is sampled by the DSP's on-chip ADC, digitally filtered, and finally fed to the PID controller on the DSP.

Based on the received position signal and the desired position, the controller calculates an appropriate command signal and sends it to the linear power amplifier in the form of analogue voltage ranging between 0 to 5 V through the digital to analogue converter (DAC) circuit. The power circuit will accordingly regulate the electric current in the electromagnetic coil and the corresponding magnetic force exerted on the embedded magnet in order to guide the capsule through a demand trajectory and keep it at the desired position.

5.3.4 Positioning With 3-axis Coil Sensor

A 1-axis coil sensor can be adopted to measure just the 1D position parameter of the embedded magnet, as it is sensitive only to the dipole magnetic field that is perpendicular to its main axis. Therefore, in order to determine the position and orientation parameters of the inserted magnet required for 2D control system, all directional components of its magnetic vector, which are related to the distance,

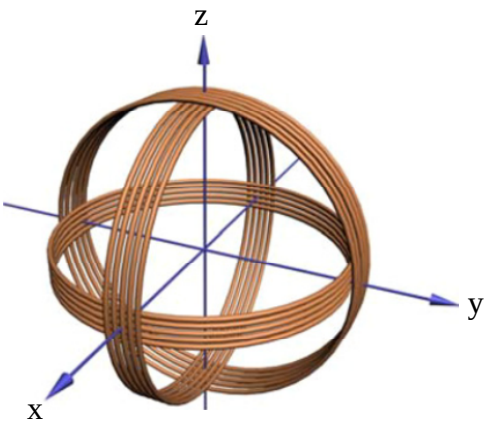

Figure 5.22: 3-axis coil sensor [94].

should be measured. To achieve this, a positioning system of at least two 3-axis orthogonal coil sensors as shown in Fig. 5.22 placed outside of the human body should be used.

5.3.4.1 Mathematical model for localization and orientation

The generating coil, which is fed by current, forms a magnetic dipole. The coordinate system shown in Fig. 5.23 shows the position of the dipole is defined by $(a, b, c)^T$, and its direction is defined by $H_o = (m, n, p)^T$. Assume that there are N coil sensors, with l-th sensor located at $(x_l, y_l, z_l)^T$, $1 \leq l \geq N$. The position vectors connecting the l-th sensor to the generating coil can then be represented by $r_l = (x_l - a, y_l - b, z_l - c)^T$, and based on (3.8) the components of the magnetic field density can be represented by:

$$
\begin{aligned}
B_{lx} &= \frac{B_T}{r^5}\left(m\left(2X^2 - Y^2 - Z^2\right) + 3nXY + 3pXZ\right) \\
B_{ly} &= \frac{B_T}{r^5}\left(n\left(2Y^2 - X^2 - Z^2\right) + 3mXY + 3pYZ\right) \\
B_{lz} &= \frac{B_T}{r^5}\left(p\left(2Z^2 - X^2 - Y^2\right) + 3mXZ + 3nYZ\right),
\end{aligned}
\tag{5.26}
$$

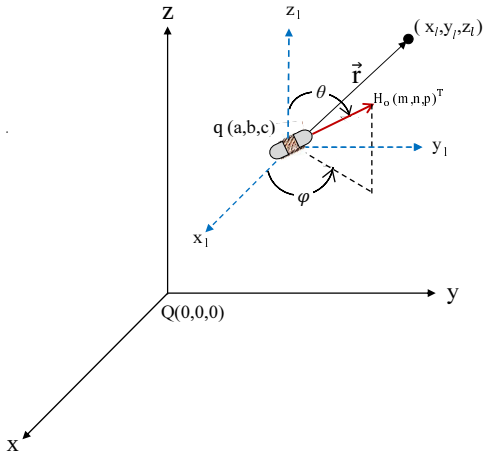

Figure 5.23: Magnetic dipole model.

where $B_T = \frac{\mu_o \mu_r \mu_c \Re}{4\pi}$, and $r = \mid \vec{r} \mid = \sqrt{X^2 + Y^2 + Z^2}$, $X = x_l - a$, $Y = y_l - b$, and $Z = z_l - c$.

In the proposed sensing system, the magnetic field densities B_{lx}, B_{ly}, and B_{lz} are measured using coil sensors that are arranged outside the human abdomen, and $(x_l, y_l, z_l)^T$, the position of the $l-th$ 3-axis coil sensor, are known in advance. Consequently, there are six unknown parameters in the system which are (a, b, c, m, n, p). The magnetic field is invariant to the rotation of the generating coil along its central axis, and hence the capsule's orientation H_o is in two dimensions. Based on the direction of the generating coil which is represented based on dipole direction representation mentioned earlier in (3.3). the vector $(m, n, p)^T$ is a normalized vector which means its length is one. Therefore, the following constraint is added

$$m^2 + n^2 + p^2 = 1 \tag{5.27}$$

Equation (5.26) governs the relationship between the magnetic field densities at $l-th$ coil sensor and the generating coil position and orientation parameters. With two 3-axis orthogonal coil sensors, it can measure six magnetic field densities by which the six parameters of the generating coil position and orientation could be

calculated by solving (5.26) and (5.27).

5.3.4.2 Positioning algorithm

The main idea of the proposed algorithm is that the position and orientation parameters of the capsule can be obtained by measuring the AC coupling signal by having enough coil sensors. The AC magnetic field components of the generating coil are detected by a pair of 3-axis orthogonal coil sensors.

The system directly samples the six AC signals from the coil sensors through the 6-channels ADC in the DSP after sensor signals are amplified and filtered by a conditioner circuit. The sampled data are calibrated to their magnetic field values. Solving the mathematical equations of the generating coil magnetic field by some appropriate calculation algorithms then yields the medical device's position and orientation parameters [31][99][100]. Finally, these parameters are fed to the LQR MIMO controller in the DSP, which in turn calculates the command signals required to guide the capsule through the desired trajectories.

5.4 Chapter Summary

In this chapter, the theory and description of two types of magnetic sensors, the Hall effect sensor and the coil sensor, are discussed in detail. Hall effect sensors have been adopted to implement positioning of the proposed actuation system using a DC magnetic field.

Both DC and AC magnetic fields are produced by embedded magnet and generating coil respectively, and these are used to transmit the 1D capsule's position information. A small permanent magnet inserted in the capsule is adopted to transmit the DC device's position signal. Circuit design for generation and driving of the capsule

transmit coil signal has been discussed in this chapter. The receiving of the DC position signal based on the Hall effect sensor and feedback signal amplification and filtering has also been discussed.

A positioning system based on the DC magnetic field was implemented using one and two Hall effect sensors on the opposite coil's poles. The two position approaches could provide accurate position data; however, the accuracy of the positioning method based on two magnetic sensors was higher at high exciting actuator currents due to heat dissipation effect. Despite this, the two hall effect sensors positioning approach was still not an optimum positioning system due to cancellation difficulty of the DC actuation fields.

Therefore, an improved positioning system based on an AC coupling signal was adopted to transmit more accurate position feedback information. The conditioning of the received signal based on a coil sensor, which includes amplification and AC to DC converting circuits, has been discussed in detail. In addition, the extraction of the AC coupling signal with minimal noise based on the DFT technique has been discussed. Furthermore, to obtain position and rotation parameters of the capsule, a 3D positioning algorithm based on 3-axis mutual orthogonal coil sensors has been presented.

Chapter 6

Implementation of Actuation Control System

In this chapter, two types of linear controllers, SISO and MIMO, are implemented digitally in real-time using a TI TMS320F2812 DSP in order to validate the proposed actuation system. The design and hardware implementation of the 1DOF and 2DOF control system are also presented.

For the SISO system, the real-time response of the linear 1DOF PID controllers, using Hall effect sensors and the coil sensors, is examined in tracking and regulating cases. The performance of the controllers under step input is discussed and compared based on fall time, settling time, maximum overshoot, and steady state error parameters.

For the MIMO scheme, the simulation design of the proposed 2D capsule actuation system is validated by real-time implementation of the 2DOF LQR controller. The controller is implemented digitally in the DSP based on a coil sensor. The practical performance of the control system is analysed and discussed in detail in this chapter, and the experimental results of the controllers implementations are also included to

confirm the validity of the proposed control strategies. Finally, an investigation of some 2D levitation control schemes based on one and two coils is introduced and their real-time response is also demonstrated and analysed in this chapter.

6.1 1D Control System Implementation and Experimental Results

In this section, the simulation design of the proposed capsule actuation system, based on the PID controller with AC and DC position feedbacks presented in Chapter 4, is validated by implementing it in real-time using the TMS3202812 DSP. The hardware design of the control system is also discussed. Finally, the experimental results of the controller implementation will be included and analysed.

6.1.1 Implementation of the Controller With DC Position Feedback

6.1.1.1 Hardware design

The experimental setup of the proposed 1D actuation system is shown in Fig. 6.1. The hardware design of the scheme is represented by the block diagram shown in Fig. 6.2. It is basically composed of three stages: a platform test bed, a position signal conditioner and a single-board DSP. The test bed consists of an electromagnetic coil, two Hall effect magnetic sensors, and a current driver unit. The signal conditioner stage contains buffering, amplification, filtering and regulation circuits while the controller is based on the TMS320F2812 DSP which samples the incoming sensor signal, performs the PID calculation and sets the actuator current by PWM. Each stage of the system hardware will be configured in the next section.

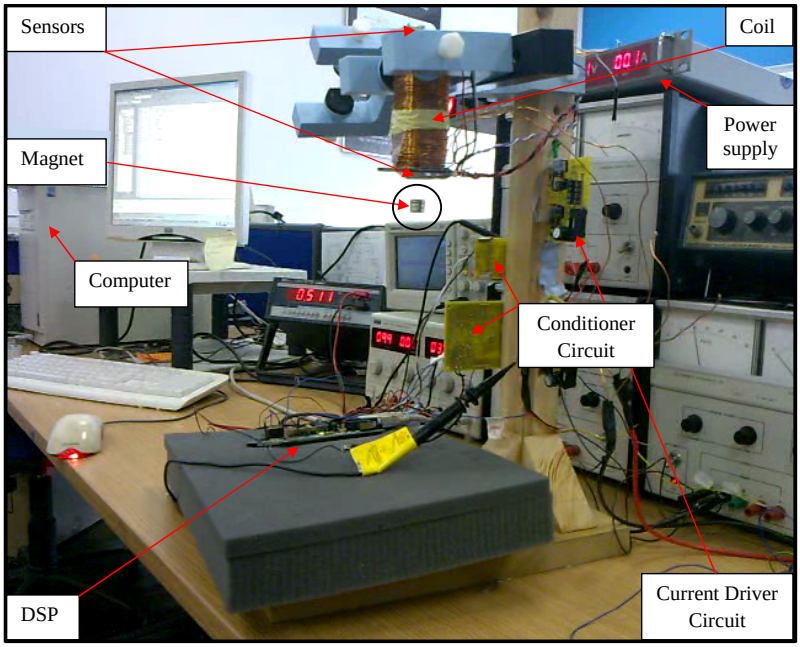

Figure 6.1: Experimental setup of the proposed 1DOF control system.

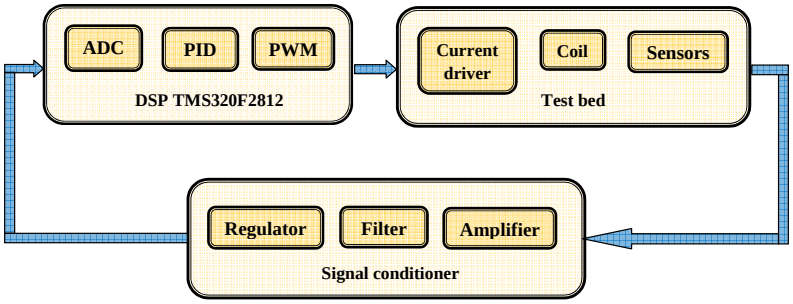

Figure 6.2: Block diagram of the control system hardware design.

6.1.1.2 Hardware system configuration

Actuator

Fig. 6.3 shows an experimental model of the actuator. It is composed of a rectangular iron-cored coil and two Hall effect sensors (A1301) which are placed on its opposite poles. The objective of the actuator is to apply a magnetic force to the inserted magnet in order to levitate the device and maintain it at the desired position. The output of the electromagnet is controlled by the processor based on the Hall Effect sensors' position signals. The characteristics of both the electromagnetic coil and the Hall effect sensor were discussed earlier in Chapters 3 and 5 respectively.

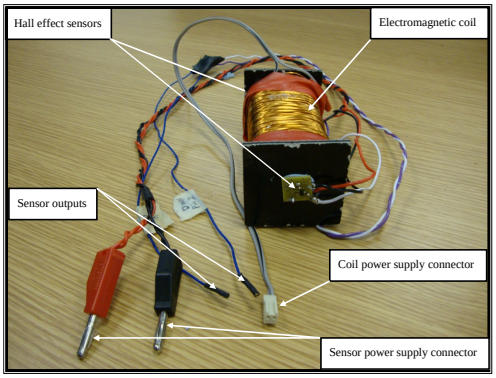

Figure 6.3: Construction of actuator coil including a Hall effect sensor.

DSP controller

The TMS320F2812 DSP is used to implement the proposed linear PID controller due to its fast and precise data processing capability which enables the real-time calculation of the control signals. The processor is a member of the TMS320C2000 DSP generation, is a fixed-point 32-bit DSP of 150MHz maximum frequency with a 12-bit pipelined ADC module which is highly integrated, and has high-performance solutions for demanding control applications [101]. A C2000 Tools Code Composer driver is also provided by Texas Instruments (TI) to provide a better code developing and debugging environment. Expansion connectors are provided for other necessary circuits, such as digital input/output I/O expansion and analogue expansion [102]. Fig. 6.4 shows a photograph of the $eZdsp^{TM}$ F2812 board. The DSP has two identical event mangers EV modules, EVA and EVB. Both of them consist of 16-bit general-purpose (GP) timers, full-compare/PWM units, quadrature-encoder pulse (QEP) circuits and capture units.

In this research project, an EVA block is utilized to sample the position signal using the DSP's on-chip ADC, while EVB is used to provide a PWM control signal with varying duty cycle to drive the power transistor circuit required to control the actuator current.

Figure 6.4: TMS320F2812 DSP board.

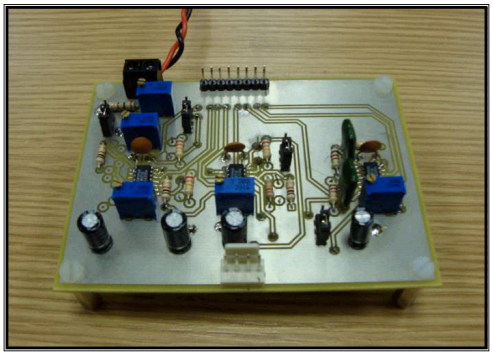

Figure 6.5: PCB board photograph for 4-channel signal conditioner circuit.

Conditioner circuit

It is not possible to send the Hall effect sensor signals to the DSP for processing as they are not high enough and mixed with noise; therefore, they are processed by a conditioner circuit whose PCB board photograph is shown in Fig. 6.5. The processing circuit is composed of buffering, amplification, filtering and regulation stages, which were previously discussed in detail in Chapter 5.

Current driver circuit

A simple current driver circuit based on a VNP7N04 power MOSFET device is designed and implemented to initially control the coil current of the proposed control system. The schematic diagram of the driver circuit is given in Fig. 6.6. The transistor has a clamp voltage of 42 V, a linear current limitation of 7 A and drain-source resistance R_{DS} of 0.14 Ω [103] . The flywheel diode, based on 1N5401, is connected

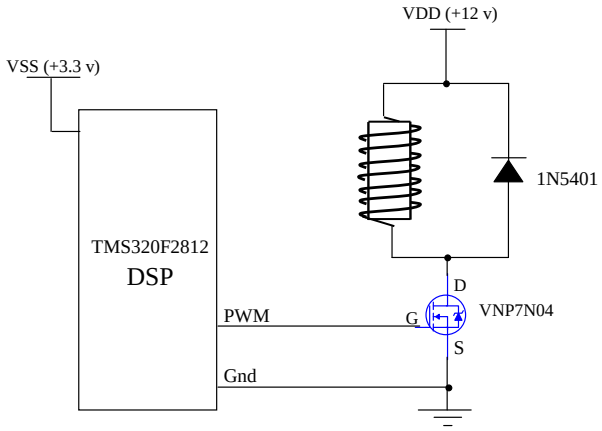

Figure 6.6: Schematic diagram of simple current driver circuit.

reverse biased across the solenoid coil, and provides a path for the current when the transistor is off so the magnetic field and current can safely decay. The current of the electromagnetic coil is adjusted though triggering the gate of the power transistor by the PWM output signal of the processor with a varying duty cycle.

The performance of the control system based on the VNP7N04 current driver circuit was acceptable; however, the circuit is unable to drive the coil current in the two directions required to enable attraction and repulsion magnetic forces between the actuator and the embedded magnet. Therefore, the current driver circuit of the proposed control system was developed by the design and implementation of a bridge circuit based on a power MOSFET IRLB3034 device. The high specifications of the high current transistor, which are stated in Appendix C.2, enable it to excite the coil by the current required to achieve levitation distance, which is realistic for inspection of the digestive tract. A schematic diagram and PCB board photograph of the bridge circuit are shown in Fig. 6.7 and Fig. 6.8 respectively.

6.1.1.3 Actuation algorithm implementation

A simple PID controller is adopted to implement the 1D actuation algorithm for the capsule endoscope. The TMS320F2812 DSP is used to implement the controller

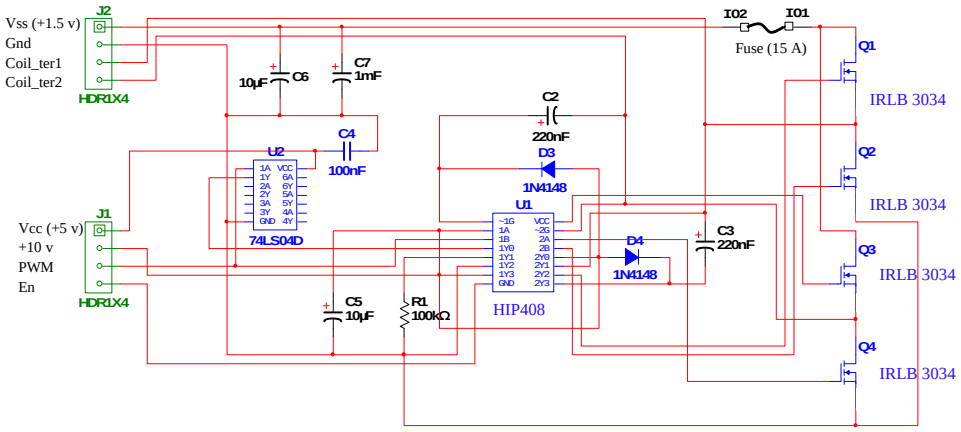

Figure 6.7: Schematic diagram of bridge current driver circuit.

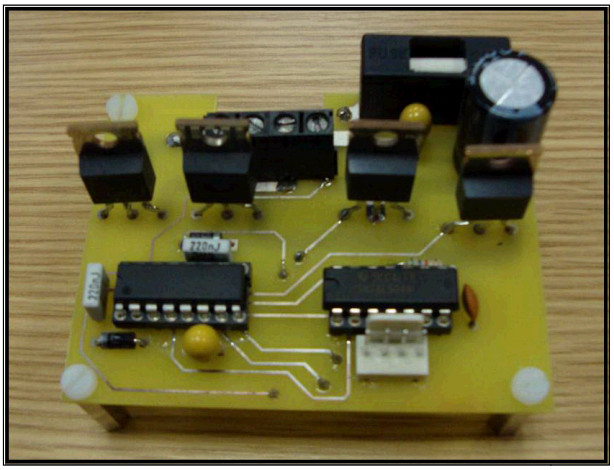

Figure 6.8: PCB board picture of current bridge circuit.

whose output is based on the PWM technique. The PWM approach has been adopted in most of the controller designs for control applications due to its high power efficiency [104].

In the proposed control algorithm, the position feedback for the capsule endoscope is based on using two Hall effect sensors placed on the poles of the coil. In this method, the capsule position signal is measured based only on the magnetic field of the inserted magnet, which is isolated by the subtraction of the sensor readings using a differential amplifier circuit as discussed earlier in Chapter 5 .

To maximise the accuracy of the position feedback, the following procedures are taken into consideration:

1. The offset between the sensor readings is reduced as much as possible as fol-

lows: while keeping the magnet away from the actuator, the offset is reduced by adjusting the differential amplifier to obtain the minimum output ($\sim$ 25 mV, which corresponds to $\sim$ 0.2 mm).

2. The DSP's on-chip ADC is calibrated in order to reduce conversion error due to inherent gain and offset errors of the processor.

The system operates by measuring the position signal of the magnet with an initial position close to the equilibrium point X_0=$[x_0\ y_0]^T$= $[0\ 0.025m]^T$ by the Hall effect sensors. The position readings are sent to the conditioner circuit for subtraction, amplification and noise filtering purposes and finally to the DSP's ADC for sampling. To further reduce the influence of the position noise, an average filter is applied in the DSP on the sampled data.

In the processor, the actual magnet position is compared with the desired vertical distance of x_d = 0.025 m to generate the error signal, which is fed to the PID controller. Based on the demand response which relates to maximum overshoot, rise time, settling time, and steady state error, the controller parameters K_p, K_i, and K_d are set. The command signal of the controller in the form of the PWM signal is calculated based on the error signal and the controller parameters. This PWM output signal, with a varying duty cycle, is used to drive the current bridge circuit based on a MOSFET IRLB3034 transistor which delivers current to the electromagnet. The structure of the digitally implemented PID controller in the DSP is given by:

$$D_y = K_p e(k) + K_i T_s(e(k) + e(k-1) + \frac{Kd}{T_s}(e(k) - e(k-1)), \tag{6.1}$$

where T_s is the sampling time of the algorithm. Based on the varying control signal, the magnetic force exerted by the actuator on the inserted magnet works to hold the device and maintain it at the desired position.

6.1.1.4 Experimental results

To show the effectiveness of the proposed capsule actuation system and to validate the simulation results, the real-time control system is implemented in the DSP based on the same conditions of the Simulink design, which include input trajectory and the controller parameters.

Due to the high acceleration and speed potential of which the suspended object is capable, it is necessary for a high sampling rate to be used within the magnetic levitation system in order to maintain stability [105]. The sampling frequency of the control system is governed by the sampling of the DSP's ADC and the controller algorithm implementation time. On this basis, the sampling frequency of the processor's ADC is set to the highest sampling rate of 25 MHz. It is worth considering that, based on this high ADC sampling rate, an average filter for the position signal is implemented in the DSP in order to reduce its fluctuation. Additionally, the controller algorithm was optimised in order to reduce the execution time.

The control system is operated at lowest possible sampling period of 130 μs which includes implementation time of ten samples average, at the highest ADC's sampling frequency of 25 MHz, and optimised computation time of the controller output. The practical results were 70% compatible with the simulation results. The reason for this is because the modelled system does not represent the real system due to the linearisation of the electromagnetic force equation and the static attraction force between the levitating magnet and the core of the electromagnet not being consid-

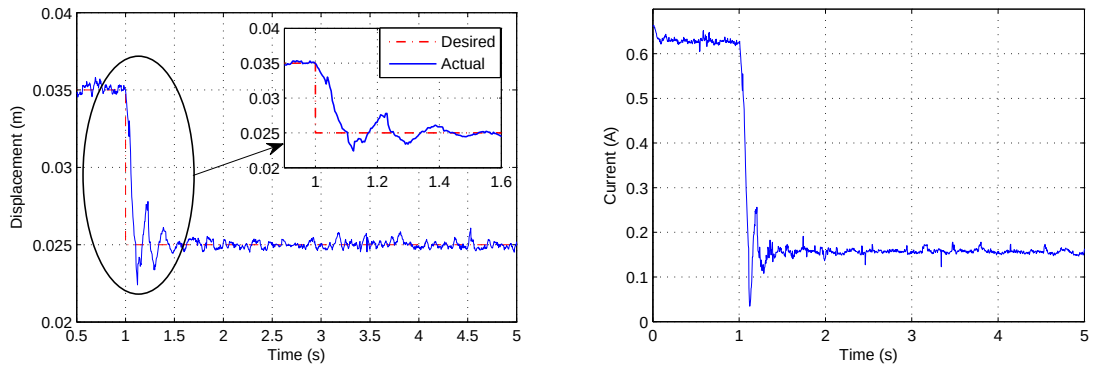

(a) Dipole position response.

(b) System input signal.

Figure 6.9: Experimental responses of the dipole position and control input for a step input.

ered.

By undertaking a minor tuning adjustment within the controller parameter K_p, an improvement in the system's behaviour can be observed. Based on controller gains $K_p = 1.32$, $K_i = 0.02$, and $K_d = 0.43$, Fig. 6.9(a) and (b) show the actual magnet position and desired step input and the coil current respectively. In practice, the constructed system, as shown in Fig. 6.1, shows levitation of the magnet in the air with a steady state vertical position of 25 mm and control effort of 0.16 A, as predicted.

It can be seen from Fig. 6.9 that the controller succeeded in forcing the dipole to follow the demand step input trajectory. Based on the mini figure shown in Fig. 6.9(a), the system has a fast fall time t_f of 0.11 s and a small system noise which oscillates between approximately ± 0.8 mm. Regarding the system control effort, the mini plot of Fig. 4.7(b) and Fig. 6.9(b) shows a very good convergence between the output current of the simulated and real-time control systems, which were at steady state 0.14 A and 0.16 A respectively. Consequently, the interesting match between the experimental and simulation results supports the validation of the system dynamics modelling and the simulation design of the control system.

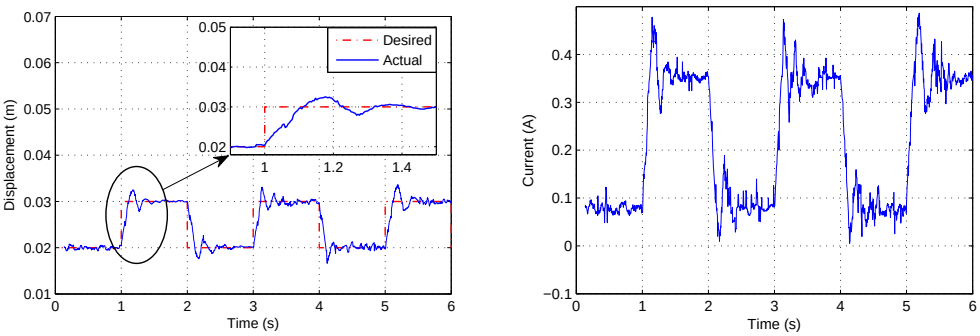

(a) Dipole position response.

(b) System input signal.

Figure 6.10: Experimental responses of the dipole position and control input for a square input.

To validate the robustness of the proposed controller, the tracking performance of the closed-loop system is examined based on a 2 Hz square input trajectory with a 10 mm peak-to-peak amplitude and offset 20 mm. The actual and the demand dipole position and the applied control effort based on the controller gains $K_p = 1.64$, $K_i = 0.1$, and $K_d = 0.65$ are shown in Fig. 6.10(a) and (b) respectively. It should be noted from Fig. 6.10a that the controller enabled the dipole to track the demand trajectory with an acceptable efficiency. The system has a fast rise time t_r of 0.12 s, and acceptable settling time t_s of 0.4 s with a small scheme noise of ± 0.8 mm. However, there is an overshoot of approximately 2.25 mm due to non-ideal loop response. The performance of the control system can be optimised by the improvement of the position feedback of the actuation algorithm, which is discussed in the next section. Fig. 6.10b, reveals the reasonable value of the actuator current range which was at a steady state at about $0.09 - 0.37$ A. Based on these good real-time results, it can be said that the robustness of the proposed controller is enough to successfully hold the embedded magnet in the capsule endoscope with the capability to maintain and move the device around the desired spot.

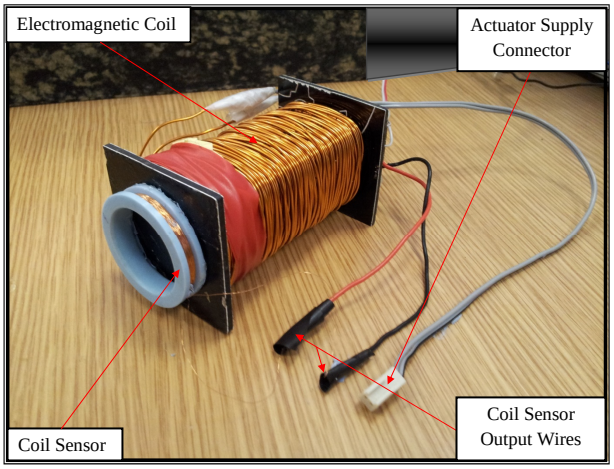

Figure 6.11: A picture of the control system actuator based on coil sensor.

6.1.2 Implementation of Controller With AC Position Feedback

6.1.2.1 Hardware design

The experimental setup and the hardware design of the AC feedback-based controller system are the same as those in the DC position feedback-based controller system; these were presented earlier in Fig. 6.1 and Fig. 6.2 respectively, except for the use of a coil sensor instead of the Hall effect sensors, and the attachment of a generating coil to the capsule for the localization purpose. The configuration of these units and their related processing are considered in the next section.

6.1.2.2 Hardware system configuration

Actuator

Fig. 6.11 shows the experimental model of the actuator. It is composed of a rectangular iron-cored coil and a 1-axis coil sensor placed on the lower pole of the coil. The function of the actuator is to apply magnetic force on the inserted magnet based on the position feedback information from the coil sensor.

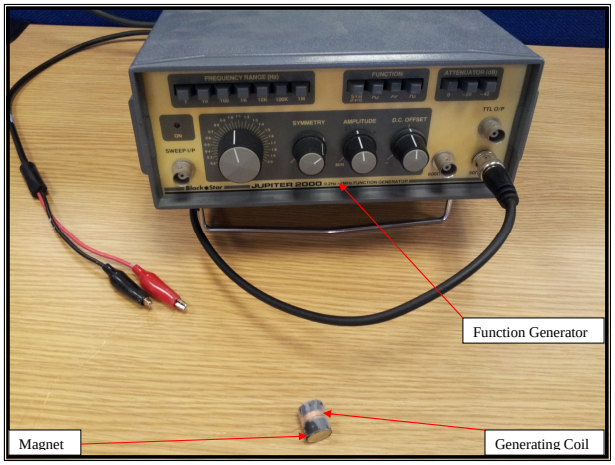

Figure 6.12: A photograph of the experimental transmission setup.

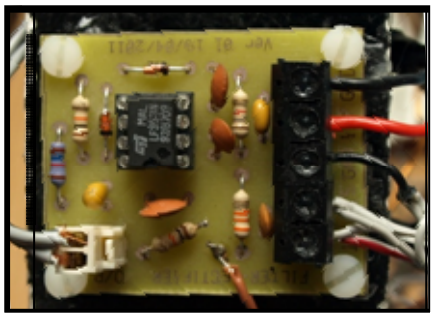

Figure 6.13: A photograph of the receiver circuit PCB board.

Conditioner circuit

The conditioner circuit of the AC magnetic signal consists of transmission and receiver sub-circuits. The transmission circuit is an exciting circuit for the generating coil by 10 $Vp-p$, 100 kHz sinusoidal signal supplied by a function generator, while the receiver circuit is composed of filtering, amplification, rectification, and regulation stages. These circuits were previously discussed in detail in sections (5.3.3.1) and (5.3.3.2). A photograph of the transmission circuit and PCB of the receiver circuit are presented in Fig. 6.12 and Fig. 6.13 respectively.

6.1.2.3 Actuation algorithm implementation

In the improved system, the capsule position information can be obtained from the AC magnetic signal produced by the generating coil, which is decoupled from the

DC actuation fields, based on the coil sensor.

The system operates by first exciting the generating coil with AC current with a frequency of (100 kHz) and then placing the capsule close to the operating position. The position signal of the capsule, which is mixed with unwanted noise, is measured by the coil sensor and then processed by the conditioner circuit. Through the conditioning circuit, the position signal with a specific frequency is extracted by a parallel RLC resonance circuit, and sent to an active BPF circuit for amplification and further rejection of unwanted frequencies. Then, the filtered signal is converted to a DC signal by rectifier circuit followed by a RC LPF circuit and finally fed to the DSP's ADC for sampling.

To further reduce the influence of the position noise, the sampled signal is averaged in the DSP. Then, the actual device position is compared with the desired vertical distance $x = 0.025$ m, to generate an error signal that is finally fed to the PID controller.

The command signal of the controller is calculated based on the error signal and the controller parameters K_p, K_i, and K_d, which are set based on the demand response of the control system. The PWM output signal of the controller with varying duty cycle is supplied to the current driver circuit, which excites the actuator by the required current to hold the inserted magnet and maintain it at the desired position.

6.1.2.4 Experimental results

Based on the controller gains $K_p = 0.78$, $K_i = 0.024$, and $K_d = 0.0216$, Fig. 6.14(a) and (b) shows the actual and desired magnet positions and the input signal of the control system respectively. Based on Fig. 6.14(a) and Fig. 4.8(a), it can be seen that there is good compatibility between the practical and simulation results. It is

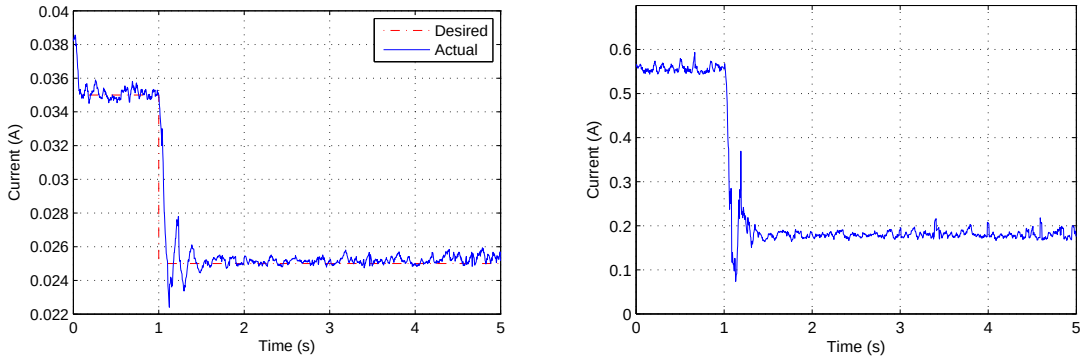

(a) Dipole position response.

(b) Input of the control system.

Figure 6.14: Experimental responses of the control system based on coil sensor.

obvious that based on the optimization of the position feedback, there are significant improvements in the performance of the control system is achieved.

Comparing the mini plots of Fig. 6.14 with Fig. 6.9: the fall time t_f of the inserted magnet reduced from 1.1 s to 0.75 s, the maximum overshoot reduced from 22.5% s (2.25 mm) to 18% (1.8 mm), and the fluctuation around the steady state position reduced from ± 0.8 mm to ± 0.6 mm. This position variance has little effect on the resolution of the taken pictures due to the low capture rate of the WCE's camera (2 frames per second) [84]. On the other hand, the overshoot level is within tolerance and will have no influence on the colon, as it is very small in proportion to the diameter of narrowest region (approximately 60 mm) within the investigated organ [85]. Regarding the control input, the initial excitation current of the actuator decreased from approximately 0.64 A to 0.57 A while the steady state current value is still approximately 0.17 A.

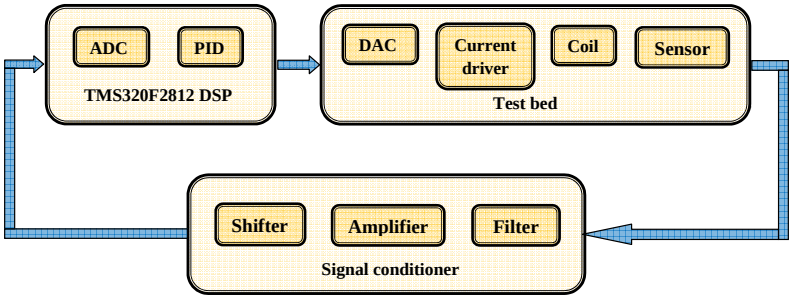

Figure 6.15: Block diagram of the improved control system hardware design.

6.1.3 Improved AC Position Feedback-Based Controller Implementation

The controller performance of the proposed actuation system based on coil sensor is improved by achieving the following procedures:

- Further noise reduction for the received position signal through digital filtering based on a coherent detector by the DSP.
- Optimizing the response time of the actuation system and reducing AC interference by sending the controller command signals to the linear power transistor through a DAC instead of the PWM approach.
- Supporting the current driver circuit by using a high current gain power transistor.

6.1.3.1 Hardware configuration

The hardware design of the improved actuation system is represented by the block diagram of Fig. 6.15. In this section, the design and configuration of improved circuits are considered. Fig. 6.16 shows a prototype circuit photograph of the improved circuits; these are the conditioner circuit of the received position signal and the processing circuit of the controller command signal.

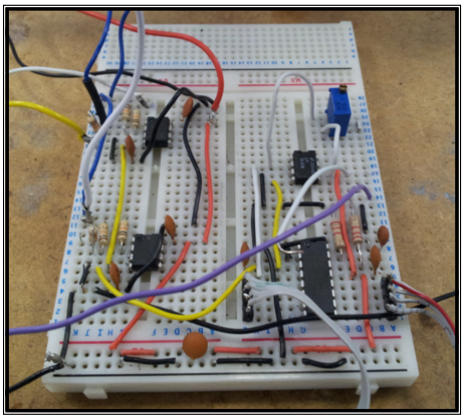

Figure 6.16: A photograph of processing circuit prototype for the improved control system.

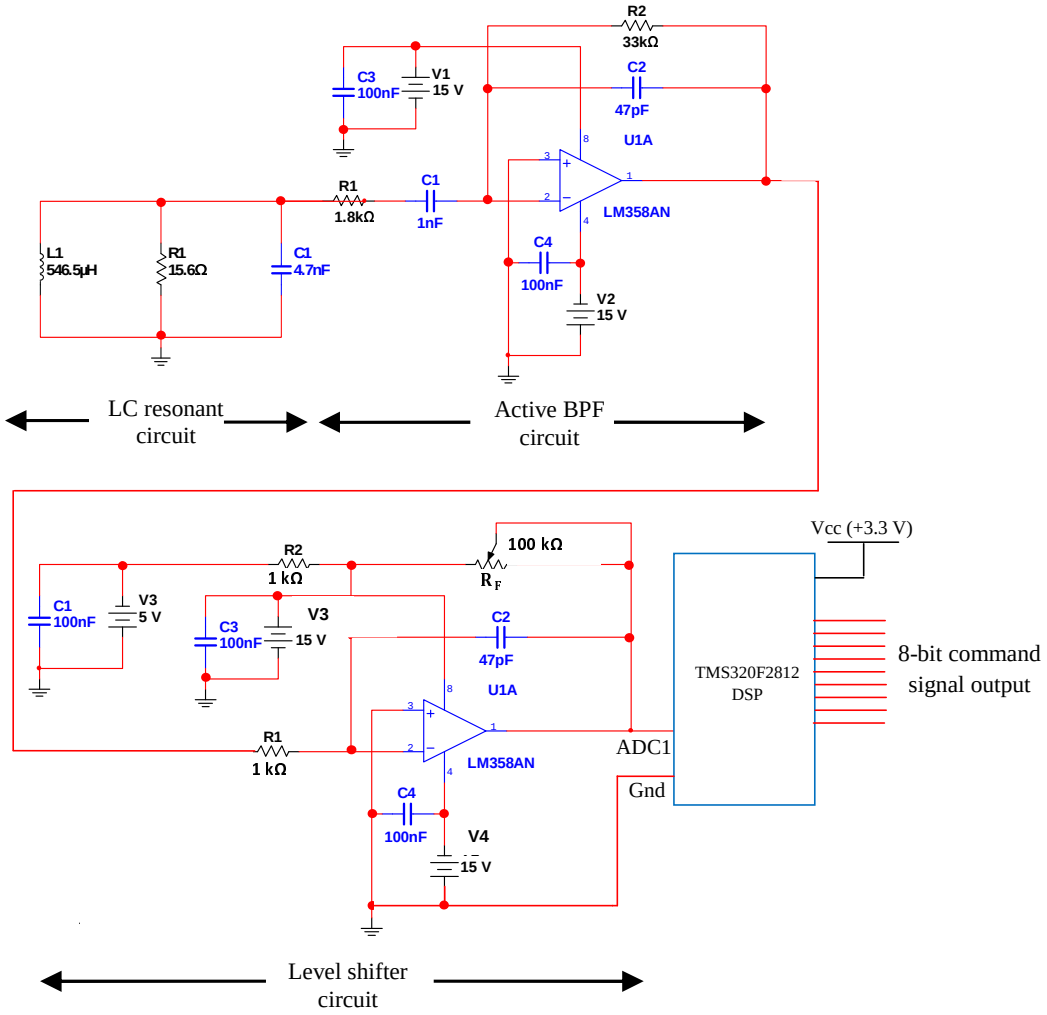

Figure 6.17: Conditioner circuit schematic of the improved control system.

Conditioner circuit

The schematic diagram of the improved receiver circuit is shown in Fig. 6.17. It is composed of the following stages:

- **Filtering**. The filtering stage is the same stage as previously stated in section (6.1.2.2). It is used to filter and amplify the position signal with a frequency of 100 kHz based on LC parallel resonance and active BPF circuits, as discussed in detail in Chapter 5.

- **Level shifter**. The objective of this stage is to shift the filtered position signal to the input range of the DSP's ADC of $Vin = 0 - 3$ V. The signal and offset gains of the shifter circuit are stated in (6. 2) and (6.3) respectively:

$$G_s = -\frac{R_F}{R1} \tag{6.2}$$

$$G_f = -\frac{R_F}{R2} \tag{6.3}$$

  For our application, based on R_F 0f 100 kΩ, G_s of 10 and G_f of -1, the shifter resistances $R1$ and $R2$ based on (6.2) and (6.3) have the same value of 10 kΩ.

Command signal processing circuit

The schematic model of the control signal processing circuit is illustrated in Fig. 6.18. It consists of the following stages:

- **DAC**. In the improved system, an external DAC circuit is used to convert the 8-bit digital output of the controller to its corresponding analogue voltage output as the DSP without a self-bring DAC module. The converter circuit is based on the DAC IC (DAC0800), which is a monolithic 8-bit high-speed current-output digital-to-analogue converter, with typical settling times of 100 ns, high output compliance 10 V to +18 V, and a low power consumption of 33 mW at ±5 V [106].

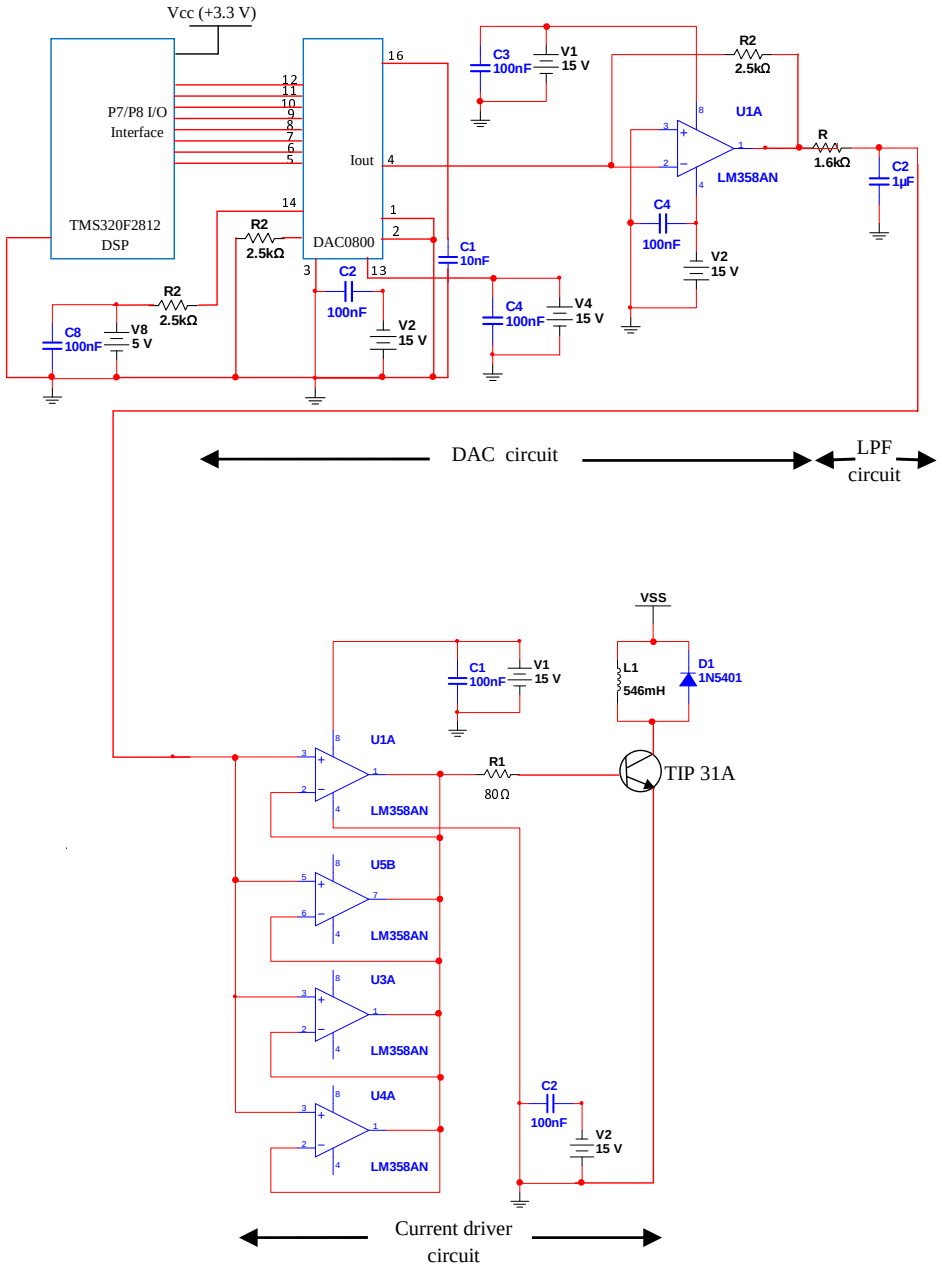

Figure 6.18: Schematic diagram of command signal processing circuit.

- **Current driver circuit**. The current driver circuit of the control system is improved by using the power transistor TIP31C with a high current gain hfe of 25. This improvement includes:

  1. Exciting the electromagnet by high current values based on a low power (current) command signal.

  2. Supporting the response time of the control system by reducing the number of turns of the coil and compensating for the actuator strength by

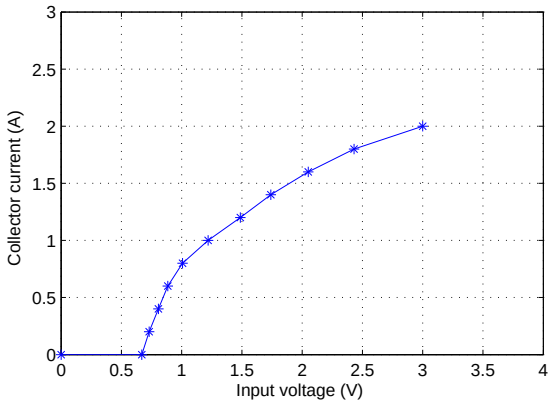

Figure 6.19: I-V characteristics of the power transistor TIP31C.

increasing its current. However, passing a high current in the coil for realistic levitation distance heats the transistor, which leads to changes in performance characteristics. Therefore, a high efficiency heat sink provided by a fan is attached to the transistor in order to dissipate power, consequently, maintaining its working temperature in the linear region.

It is worth considering that increasing the coil current raises its temperature which leads to a change in the magnetic behaviour of the actuator; therefore, the exciting current should be within reasonable values. In the proposed actuation system, the current range at which the coil works in linear region is $0-3$ A. Based on the experimental characteristics of the power transistor as shown in Fig. 6.19, it can be seen that the device has a linear behaviour within the interesting current range $0-3$ A.

To enable the converted command signal to drive the TIP31C transistor, a buffer circuit of four unity gain amplifiers connected in parallel is used as shown in Fig. 6.18. Fig. 6.20 shows a PCB board photograph of the command signal processing circuit.

The proposed control system is designed for a maximum suspension distance

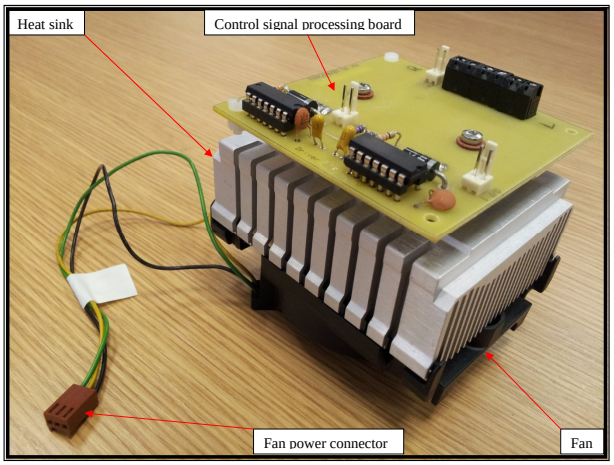

Figure 6.20: A PCB board photograph of command signal processing circuit.

of 0.04 m at which the exciting coil current is 2 A. based on these considerations, the base resistance of the transistor is calculated and has the value of approximately 33 Ω.

6.1.3.2 Actuation algorithm implementation

The linear PID controller is also be used to implement the improved actuation algorithm based on the DSP. After exciting the generating coil by 100 kHz voltage signal from a function generator equipment, the system operates through placing the inserted magnet initially close to the operating position. Based on the AC magnetic signal of the generating coil, the induced voltage in the coil sensor is sent to the filtering and amplification stages in the conditioner circuit in order to extract the position signal. The amplified signal with a frequency of 100 kHz is fed to the DSP's ADC for sampling after shifting it to the input range of the converter by a level shifter circuit.

To further reduce the position signal noise, the sampled signal is filtered digitally in the DSP based on single bin DFT technique. Then, based on the same conditions mentioned earlier, the controller calculates digital command signal. A DAC circuit is used to convert the 8-bit digital control signal output of the controller to its

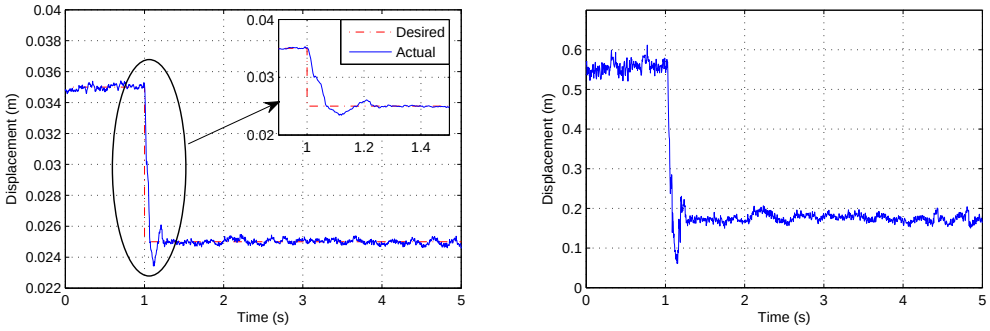

(a) Dipole position response

(b) System input signal

Figure 6.21: Experimental responses of the dipole position and control input of the improved system.

corresponding analogue signal, which is then fed to the power transistor through the buffer circuit. The transistor finally delivers the controlled current to the actuator in order to levitate the embedded magnet and move it to the desired position.

6.1.3.3 Experimental results

Based on controller gains $K_p = 0.9$, $K_i = 0.025$, and $K_d = 0.022$, Fig. 6.21(a) and (b) shows the actual and demand capsule positions and the input current of the control system respectively. In Fig. 6.21, it can be observed that significant improvements in both transient and the steady state response of the control system is achieved due to the improvements in the position feedback of the actuation algorithm. Comparing the mini plots of Fig. 6.21 with Fig. 6.14, the fall time t_f of the embedded magnet reduced from 0.75 s to 0.65 s, the maximum overshoot reduced from 18%(1.8mm) s to 14%(1.3mm), and the fluctuation around the steady state position also reduced from ±0.6 mm to ±0.3 mm. It is worth considering that reducing the system noise will reduce blurring effect in the captured pictured. Regarding the control input, the initial and steady state excitation current of the actuator are kept within the reasonable values of approximately 0.57 A and 0.16 A respectively.

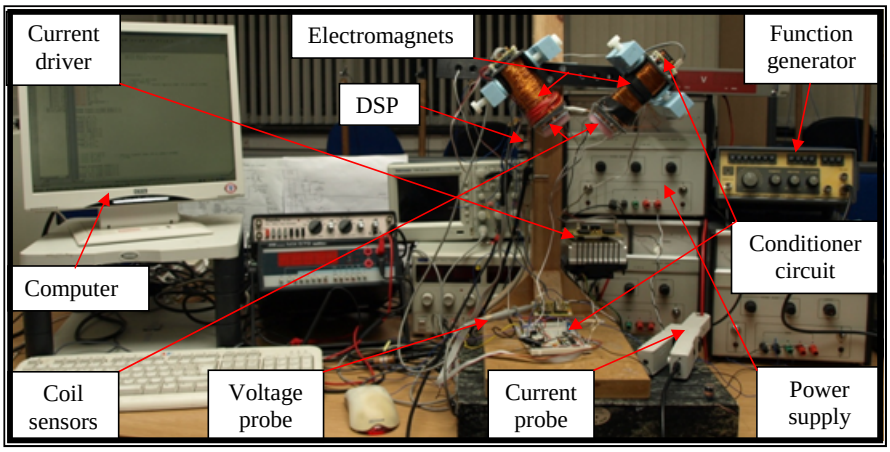

Figure 6.22: Experimental stage of the 2D control system.

6.2 2D Control System Implementation and Experimental Results

In this section, the simulated design of the 2D control system, based on the linear LQR technique presented in Chapter 4, was validated through its real-time implementation in the DSP. The hardware of the proposed control system was designed, implemented and then presented. Finally, the real-time results of the implemented controller were included and analysed to confirm the performance of the proposed actuation scheme.

6.2.1 Hardware Design

The experimental platform of the proposed 2D control system is shown in Fig. 6.22. Basically, the hardware design of the system is the same design of the 1D control system, as previously presented in Fig. 6.15. The test bed consists of two electromagnetic coils with two coil sensors, and a 2-channel command signal processing unit. The signal conditioner stage is composed of a 2-channel filtering and amplification circuits while the DSP is also based on the TI TMS320F2812 board which is used to implement the proposed 2DOF controller.

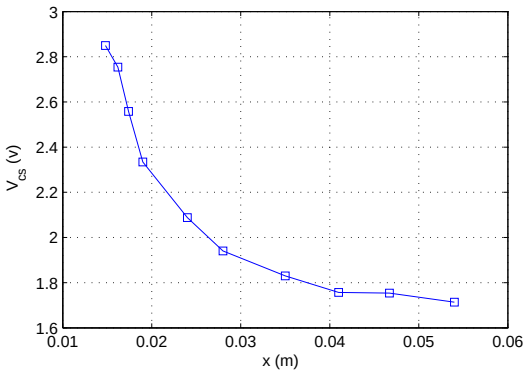

Figure 6.23: Axial distance versus induced voltage in the left coil.

6.2.2 Actuators Calibration

As is well known, the actuator of the proposed 2D control system is based on two coils situated orthogonally on a movable frame. The right coil is already calibrated as it is the coil of the 1D control system, while the left coil, which is designed with the same physical and magnetic parameters as the right electromagnet, is calibrated based on the same calibration procedure, as mentioned earlier in Chapter 4. Fig. 6.23 shows the calibration curve of the left solenoid.

To reduce the real-time computational load of the actuation algorithm, the calculation process of the device position is approximated by the following expression, which is used to convert the DSP's ADC reading $Vs2(t)$ to the corresponding position $r_2(t)$.

$$r2(t) = -0.38Vs2^5(t) + 4.51Vs2^4(t) - 21.1Vs2^3(t) + 49.2Vs2^2(t) - 57Vs2(t) + 26.5, \tag{6.4}$$

where $Vs2(t)$ is the reading of the left sensor (V).

6.2.3 Actuation Algorithm and Implementation

The implementation of the proposed LQR optimal controller requires the plant states to be measurable as it based upon full state feedback. In the proposed system, the displacement states $\Delta x(t)$ and $\Delta y(t)$ are measured directly by using coil sensors, while the unmeasurable velocity states $\dot{\Delta x}(t)$ and $\dot{\Delta y}(t)$ are simply measured by implementing the derivative of the $\Delta x(t)$ and $\Delta y(t)$ in the DSP respectively, instead of incorporating a partial observation into the system which increases the complexity of the implementation.

The system is implemented based on the same conditions which are previously mentioned in the section (6.1.3.2). Then, using the calibration curves shown in Fig. 5.4 and Fig. 6.23, the position signals based on right and left coil sensors (Vs1,Vs2), are calibrated to their corresponding axial distance values $r1$ and $r2$ respectively. The states of the proposed 2DOF LQR controller are calculated based on these axial displacements as follows:

$$\Delta x(t) = \frac{r2^2 - r1^2}{2L} - x0 \tag{6.5}$$

$$\Delta y(t) = \sqrt{r2^2 - (\frac{L}{2})^2 + \frac{r2^2 - r1^2}{2L}(L - \frac{r2^2 - r1^2}{2L})} - y0 \tag{6.6}$$

$$\dot{\Delta x}(t) = \frac{\Delta x_{n+1}(t) - \Delta x_n(t)}{Ts} \tag{6.7}$$

$$\dot{\Delta y}(t) = \frac{\Delta y_{n+1}(t) - \Delta y_n(t)}{Ts}, \tag{6.8}$$

where Ts is the sampling time of the real-time system.

The forward gain matrix K_d is calculated based on dynamic matrices A and B and the desired vector $Xd(t)$ using (2.34), while the feedback gain matrix K is calculated based on the state and control penalty matrices $Q(t)$ and $R(t)$ using the Matlab command "lqr". Then, the plant states are compared with the desired states $Xd(t)$

to generate the error vector, which is adopted with the controller gain matrices K and Kd to calculate the 2-channel 8-bit digital control input $\Delta U(t)$ using (4.29). Finally, the control signals are sent to the power transistors through a 2-channel DAC circuit which regulates the coil currents in order to hold the inserted magnet and maintain it at the y-variable desired position.

6.2.4 Experimental Results

The 2DOF actuation algorithm, based on the linear LQR technique, is implemented in real-time using the DSP. The sampling frequency fs of the control system is increased as much as possible by optimizing the controller algorithm in order to reduce its execution time. Additionally, the sampling frequency of the DSP's ADC is set to the highest sampling rate of 25 MHz. Based on the forward K_d and feedback K gain matrices derived from the simulated controller:

$$Q(t) = \begin{bmatrix} 9*10^4 & 0 & 0 & 0 \\ 0 & 350 & 0 & 0 \\ 0 & 0 & 20 & 0 \\ 0 & 0 & 0 & 0.05 \end{bmatrix}, R(t) = \begin{bmatrix} 1.1 & 0 \\ 0 & 0.825 \end{bmatrix},$$

$$K_d(t) = \begin{bmatrix} 0 & 0 & 38.577 & 0 \\ 0 & 0 & -38.577 & 0 \end{bmatrix}, K(t) = \begin{bmatrix} -26.219 & -3.002 & 73.082 & 3.247 \\ -26.281 & -2.838 & -81.997 & -3.6435 \end{bmatrix}$$

the actuation algorithm is executed with sampling frequency fs of 2 kHz. Practical observations showed that the poor stability and accelerated oscillation were dominant in the response of the control system. The reason for this that the simulated system is not completely compatible with the real-time system, an adjustment in the controller gain matrices is required to achieve better control response.

After numerous adjustments in the gain matrices, a little improvement in the perfor-

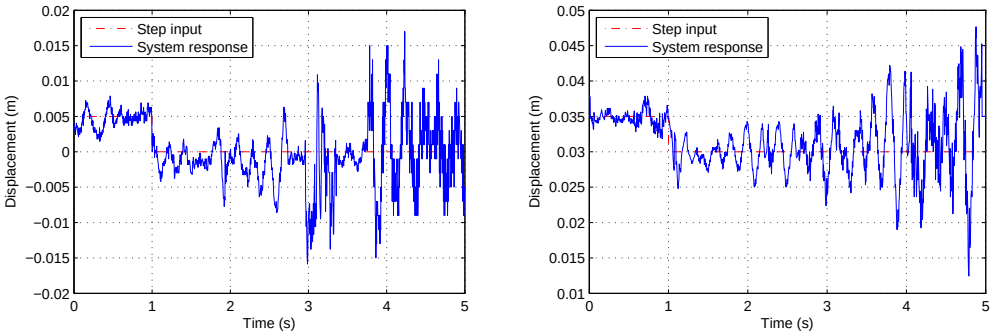

(a) Response of state x(t).

(b) Response of state y(t).

Figure 6.24: Experimental responses of the dipole position.

mance of the tracking system is shown. Fig. 6.24(a) and (b) demonstrate movement of the magnet in the x and y-directions respectively. However, the system behaviour is still not acceptable due to the instability and oscillation of the dipole. The reason for this is that the implemented controller is not able to send proper command signals to the actuators due to the insufficient position feedback information from the two coil sensors. Additionally, the sampling frequency of the control system is not high enough to run a stable levitation system due to long period of the command signal computation time. For our application, the magnet can be suspended successfully if the sampling frequency of the control system is not less than 2.5 kHz.

In order to achieve stable control of the magnet based on a two coil system, an improvement in both the position feedback and controller design must be considered. The position feedback of the control system is improved by obtaining the device position and orientation information from a pair of 3-axis orthogonal coil sensors. Regarding the controller design improvement, the rotation angle of the magnet must be considered in the dynamic modelling of the system as a manipulating factor so that it can control this factor by a 3DOF controller system. In this research project, a realistic simulation design of the improved 3DOF control system was achieved in Chapter 4 while its real-time implementation of the system will considered in future

work.

6.3 Investigation of Capsule Actuation Schemes

In this section, actuation systems based on one and two controlled electromagnetic coils are proposed for capsule navigation. Controllers based on the linear PID and bang bang techniques are designed and then implemented in real-time to validate the proposed actuation systems.

6.3.1 One Actuator System

In this system, a 1DOF controller based on single coil is designed and implemented in the DSP for capsule actuation.

6.3.1.1 System configuration

Fig. 6.25 shows the simulated setup of the proposed 4DOF actuation system. The proposed actuation system mainly consists of an actuator, a small cylindrical permanent magnet, a position sensor, a processor, and a 4DOF robotic movable frame. The actuator is based on a controlled electromagnetic coil, which is situated horizontally on the movable frame. The NdFe-based magnet is enclosed by a capsule with a generating coil. The dipole magnetization is set on the same direction as the device symmetrical axis. The capsule position detection is based on a coil sensor fixed on the lower coil's pole. Finally, the processor is based on the TI TMS320F2812 DSP, which is used to implement the controller of the proposed system.

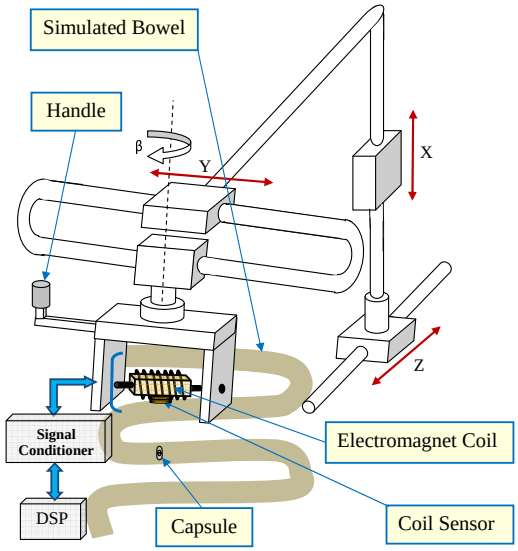

Figure 6.25: Conceptual platform of the 4DOF actuation system based on one coil.

6.3.1.2 Control system design

The proposed actuation system is designed to move and orient the capsule to the relevant places in the tested organ for evaluation purposes. 1DOF PID technique is adopted to implement a linear controller of the system. The controller is designed to hold the embedded magnet and maintain it at the desired position in a horizontal position. Then, it can move the capsule through the colon in the x, y, and z-direction and control its inclination angle (β) by translating the controlled electromagnet and/or the patient's bed using the 4DOF robotic manipulator.

It is worth considering that the command signal of the controller, which is based on position feedback information from the coil sensor, is subjected to the same conditioning and filtering stages mentioned in sections (5.3.3.1) and (5.3.3.2) based on digital detector.

6.3.1.3 Experimental results

The real-time response of the controller in the x and y-direction are shown in Fig. 6.26(a) and (b) respectively. The experimental results showed that the proposed controller is not able to stabilize the embedded magnet at the desired position.

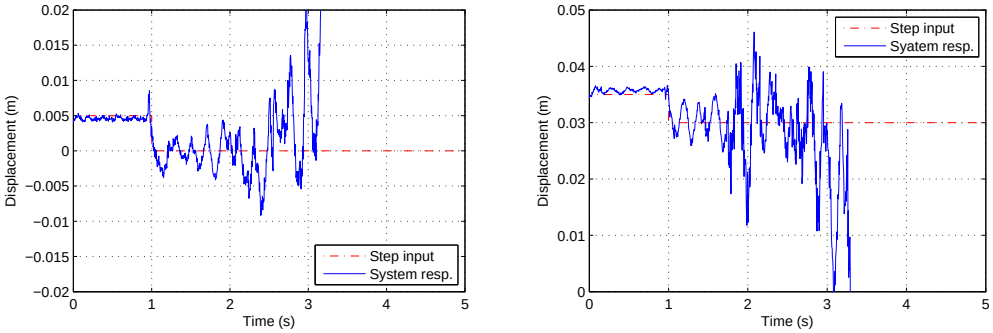

(a) Response of state x(t).

(b) Response of state y(t).

Figure 6.26: Experimental responses of the dipole position.

The reason for this is due to the high inherent instability of the levitation system and the inadequacy of the robustness of the controller in facing the strong magnetic torque exerted by the actuator on the dipole; this works to align the dipole along the actuator's magnetic field and, consequently, to drag the capsule to the coil.

6.3.2 Two Actuators System

1DOF and 2DOF linear controller systems based on two coils are designed and implemented for capsule actuation in this section.

6.3.2.1 Vertical coils method

System configuration

The simulated platform of the proposed 4DOF actuation system is presented in Fig. 6.27. It is mainly composed of an actuator, a small cylindrical permanent magnet, a position detector, a processor, and a 4DOF robotic movable frame. The actuator is assembled using two identical iron-cored coils fixed vertically on a 4DOF robotic movable frame. The NdFe-based magnet is enclosed by a capsule with a generating coil. The dipole magnetization is set in the same direction as the device's symmetrical axis. Two 1-axis coil sensors attached to the near coil's poles to

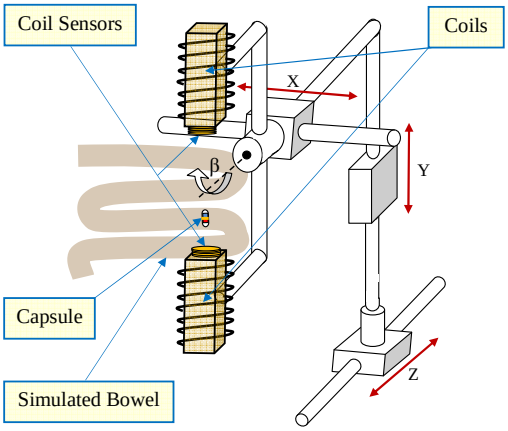

Figure 6.27: Conceptual platform of the 4DOF actuation system based on two vertical coils.

the capsule are used for position feedback. Finally, TMS320F2812 DSP is used for controller implementation.

Control system design

The proposed actuation system is designed for capsule positioning and orientation. Two separated 1DOF PID techniques are used to implement the controller of the system. The controllers are designed to hold the inserted magnet and maintain it at the desired position so that it can move the device through the intestine in the x, y, and z-direction with the capability of controlling its inclination angle (α) by moving the actuators using the movable frame.

Experimental results

The practical response of the control system based on the highest sampling frequency of 2.8 kHz showed poor performance of the proposed controllers. The reason for this is due to the high nonlinearity of the magnetic suspension system and the controllers are not robust enough to control the repulsion forces between the magnet and the coils due to the coupling between the current inputs of the actuator. Demonstration of the control system in vertical dimension is shown in Fig. 6.28.

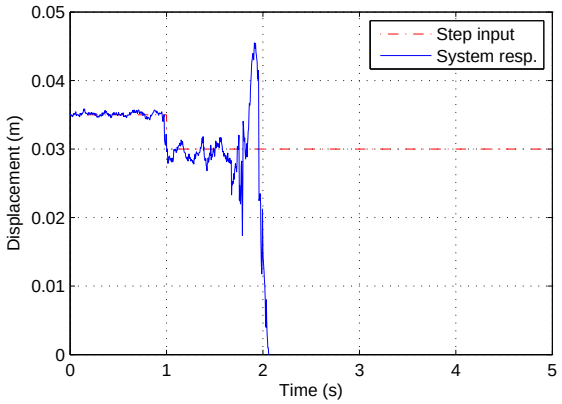

Figure 6.28: Vertical distance response of the control system.

It is worth considering that the proposed controller algorithm of the actuation system is modified by fixing the current of the lower coil and adjusting the upper coil's current by applying a PID controller with a higher sampling frequency of 5.2 kHz. However, the performance of the system is still not acceptable as the controller is not able to enable the dipole to oppose the strength of the magnetic torque as the magnetic force of the lower coil is not controlled.

6.3.2.2 Orthogonal coils method

System configuration

The configuration and hardware design of the proposed system has the same configuration and design of the 2D control system, as previously stated in section (4.2.1.1) and (6.2.1)

Control system design

The proposed actuation system is designed to control the capsule position. The bang bang technique is used to implement the 2DOF linear controller of the system. The scheme operates by taking the sensor readings when the dipole is placed in the

desired position. Then, these desired readings are compared using the DSP with the sensor measurements based on the actual magnet position. If the position feedback signal of any coil is bigger than its desired value, the controller then turns its current off and the current of the other coil on, and vice versa.

It is worth considering that the success of the controller implementation depends on the precision of the position feedback and the sampling frequency, which should be set as high as possible. In the proposed actuation strategy, after maintaining stable control of the device based on the on/off controller, the endoscopic capsule can then navigate the colon in the x, y, and z-direction by moving the actuators using the movable frame.

Experimental results

The real-time response of the 2D control scheme in the x and y-direction, based on a sampling frequency of 3 kHz, are shown in Fig. 6.29(a) and (b) respectively. The experimental results demonstrate that the proposed bang-bang controller is also not able to stabilize the magnet at the demand position. The reason for this is that the position feedback information from two sensors is not enough as it does not include the dipole rotation angle. Consequently, the controller can not regulate the coil currents properly as its command signals are calculated based on a wrong position feedback. Therefore, the position feedback of the proposed actuation system should be improved by obtaining the device position and orientation information from a pair of 3-axis orthogonal coils. Additionally, the sampling frequency should also be increased as much as possible by using a floating point DSP due to its ability to implement the float complex computational operations of the control algorithm in a short time, compared with the used fixed point processor.

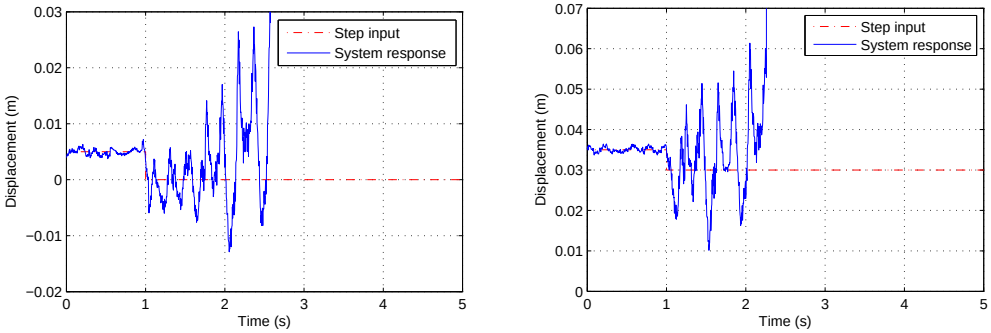

(a) Response of state x(t).

(b) Response of state y(t).

Figure 6.29: Experimental responses of the dipole position.

6.4 Chapter Summary

In this chapter, SISO and MIMO linear controllers were implemented digitally in real-time using the DSP in order to validate the proposed simulated actuation systems. The electronic circuits of the proposed controllers were designed, implemented, tested, and finally printed. In the 1D control system, the DC magnetic field produced by the coil and the magnet are used for actuation and localization purposes respectively. A linear PID controller was designed to send the PWM control signal with varying duty cycle to the actuator based on the position feedback information from the Hall effect sensor. The real-time response of the scheme is examined under step and square input trajectories and experimental results were obtained and included in this chapter. The position feedback of the 1D proposed control system is improved by using the AC magnetic field to obtain the device position information based on the coil sensor, decoupling it from the DC actuation fields. This positioning approach is susceptible to AC interference from the PWM drive. Hence the PWM drive is replaced by a linear power transistor driven from DAC circuit. The resolution of the position feedback was also increased through reducing the positioning noise by digital filtering implementation based on coherent detector in the DSP.

The real-time response of the proposed actuation using these position sensors are compared based on fall and settling time, maximum overshoot, and steady state error parameters. The experimental results have shown that the PID controller based on both sensing strategies enables the embedded dipole to follow the demanded input trajectories effectively. However, the response of the control scheme based on the coil sensor has the shortest settling time, and the smallest overshoot value and steady state error.

For the 2D control system, the 2DOF LQR controller system, based on the coil sensor, was implemented digitally using the DSP. The practical performance of the closed-loop control system showed that the controller was not able to maintain stable control of the dipole as the position feedback from the two coil sensors did not include the magnet rotation angle. Finally, an investigation of some magnetic suspension systems using one and two coils based on the PID and bang-bang techniques has been presented and their real-time performance has also been demonstrated and analysed in this chapter.

Chapter 7

Conclusions and Future Work

7.1 Magnetic Actuation

In this thesis, a novel actuation system for a capsule endoscope for colon examination was proposed. The endoscopic capsule navigation system proposed is based on current controlled magnetic levitation, utilising a small permanent magnet inserted within the capsule and an arrangement of digitally controlled electromagnets incorporating position sensors outside the human body on a robotic movable frame.

The proposed system is based on magnetic actuation as the transfer of the magnetic field does not need cables or wires. Furthermore, the permeability of the human body enables the magnetic actuation to occur wirelessly from outside the patient. Moreover, the inserted magnet does not need a power supply and can be actuated wirelessly by an external magnetic field. Consequently, it can be said that magnetic actuation is a potential solution to the capsule actuation problem.

7.2 Actuator Coil Design

During the course of this study, the following concerns were raised related to the actuator coil design:

1. Increasing the excitation current of the coil increases the strength of the actuator; however, this process can lead to an unstable control system due to an increase in the heat power dissipation in the coil, which changes its behaviour and that of the attached position sensors. Therefore, a trade off between increasing the actuation field based on the coil current and the stability of the actuation system should be taken into consideration.

2. Increasing the number of turns is another procedure which can be adopted to increase the strength of the actuator; however, this action increases the response time of the system due to the increase in coil inductance and, consequently, leads to an unstable actuation system.

3. Comsol simulation of magnetic field pattern around the actuator coil based on its geometry parameters suggests that for any manipulation distance, an optimum radius for the coil can be calculated based on the coil dimensions factor ($D_f = \frac{x}{r_c} = 1.0416$). For example, for a manipulation region around the realistic distance x of 15 cm, the optimum coil's radius is $r_c = 14.4$ cm.

4. Using a purified iron core with a relative permeability μ_r of 5000 instead of the used one with a poor permeability of approximately not more than 50 is a promising solution, which can be adopted to increase the levitation distance to a realistic value. By this action the generating magnetic field is strengthened, while the power dissipation and the response time of the control system are kept within acceptable values.

Based on these considerations, a proposed actuator coil was designed using Comsol software for a future capsule actuation system so which can achieve a realistic magnetic levitation distance for colon inspection.

7.3 Position Feedback Sensing

Both DC and AC magnetic fields were used to obtain the position information of the capsule based on a Hall effect sensor and coil sensor respectively. In this research project, two positioning approaches based on one and two Hall effect sensors on opposite coil's poles were adopted to obtain the 1D capsule position using a DC magnetic field generated from the embedded magnet.

Hardware and software processes were applied to the Hall sensor readings in order to increase the accuracy of the position feedback of the actuation algorithm. Firstly, the high frequency noise of the position signal was filtered by implementing a hardware RC-LPF circuit. Additionally, before achieving the sampling of the filtered position signal in the processor, the accuracy of the position feedback in the proposed system was also increased by implementing a calibration for the DSP's on-chip ADC in order to reduce conversion error due to inherent gain and offset errors. To further reduce the influence of the position feedback noise, a mean filter was implemented digitally in the DSP by which an average of ten repeated samples were achieved in order to reduce the fluctuation of the position signal. In the proposed actuation algorithm based on Hall effect sensors, the position signal was fed to the controller, which sent PWM command signals with varying duty cycle to the actuator through MOSFET bridge circuit in order to regulate the coil current.

The two positioning methods provide the controller with accurate position feedback; however, based on the high excitation current, more accurate position data were ob-

tained using the two Hall sensors on opposite coil's poles method. The reason for this is that the positioning accuracy of single sensor method depends on the stability of the coil behaviour which changes at high excitation currents due to increased coil heat dissipation. This behaviour varying influence was reduced by using two Hall effect sensors as the dipole position measurement depends only on the magnetic field of the inserted magnet, which was isolated by subtracting the sensor readings using a differential amplifier circuit.

It is worth noting that the positioning approach based on two Hall effect sensors was still not an optimum positioning scheme for capsule actuation as it is difficult to guarantee cancellation of the two sensor readings due to mechanical tolerances, thermal drift and sensor variations. Therefore, the positioning approach of the proposed actuation system was improved by obtaining more accurate position data for the capsule endoscope from an AC magnetic signal using coil sensor, which was decoupled from the DC actuation fields.

However, using the PWM technique to drive the actuator coil based on this sensing method produces an AC interference effect on the position coil sensor. Hence, the positioning scheme was improved by using the linear power amplifier driven by a DAC circuit to pass the controller command signals to the actuator. Finally, a very important reduction in the position noise was also achieved by using a digital coherent detector based on a single bin DFT technique in the DSP. The experimental results have shown that by using the digital filtering, the level of the position signal noise was reduced by factor of 4.

It is worth considering that a greater reduction for the position feedback noise can also be achieved by increasing in the integration time of the digital coherent

detector; however, this process increases the computational time of the positioning algorithm and, consequently, degrades the response time of the closed-loop control system. To overcome this problem a floating point DSP with higher computational power and a faster processor should be used.

7.4 Closed-Loop Digital Control

In the SISO control system, a linear PID controller was designed to actuate the capsule in a vertical dimension around the operating position and maintain it at a variable desired position. A realistic simulation design for the actuation system based on experimental position measurements was implemented to validate the proposed controller. The system was simulated under step input and its performance was evaluated based on settling time, overshoot value, steady state error and control input parameters. The simulation results of the controller demonstrate its ability to successfully navigate the embedded magnet through the desired trajectory and maintain the device at the variable demand position, with a short settling time of 0.1 s, a low overshoot value of 20% and a small steady state error of 2.25 mm.

To verify the effectiveness of the proposed actuation system, the PID controller was implemented in real-time using the TMS320F2812 DSP, where the position feedback based on two Hall effect sensors on opposite coil's poles was adopted to generate PWM command signals with varying duty cycle which were used to regulate the coil current.

The experimental response of the control system under step reference input showed that there is a good match between the simulation and practical results. Based on an acceptable control input, the controller was able to suspend the inserted magnet effectively and maintain it at a variable desired position with a settling time of 0.11

s, an overshoot of 25% and a steady state error of ±0.8 mm.

In the research project, the proposed actuation system was optimised by improving the position feedback through the use of an AC magnetic signal to provide the position data based on coil sensor. Details of this position improvement were discussed in the previous section. The real-time responses under step trajectory input have shown that the optimised system, compared with the DC position feedback-based system, has a shorter fall time, minimal overshoot value and steady state error; these were 0.75 s, 18%, and ±0.6 mm respectively.

To validate the robustness of the improved system, its tracking performance is evaluated based on square input trajectory. The real-time response have shown that the the controller with AC position feedback was able to successfully guide the inserted magnet through the demand reference input based on acceptable control effort.

For the MIMO scheme, several 2DOF linear controllers based on the PP, EEA, and LQR techniques were designed and simulated for the 2D capsule actuation. Their tracking responses were also compared based on stability, positioning accuracy and control efforts. The simulation results have shown that, based on reasonable control inputs, the LQR controller has the fastest response with a minimal overshoot value and steady state error. To validate the LQR simulation results, the controller algorithm was implemented digitally on a DSP in real-time. The practical performance of the proposed tracker scheme has shown that the LQR controller was not able to effectively guide the embedded magnet through the demand trajectory.

The reason for this is that the two sensors were not able to provide the tracking algorithm with sufficient position feedback information, which includes position and orientation of the capsule. Hence, the capsule sensing system was improved by using a pair of 3-axis orthogonal coil sensors in order to obtain both the position and

orientation angle of the inserted magnet.

A 3DOF controller system based on the linear LQR method was designed to actuate the magnet in the x and y-direction with the capability of maintaining it at the desired position and orientation angle. To validate the proposed controller, a realistic simulation model for the 3DOF capsule actuation system was implemented and its tracking performance was evaluated. The Simulink results have shown that the controller succeeded in actuating the inserted magnet through the desired input trajectories and guided it to the demand angle effectively.

It is worth noting that the realism of the Simulink model of the proposed 3DOF actuation system is not high enough as the system thermal drift and variation of the coil parameters were not taken into consideration in the modelling of the actuation system. Moreover, the expected stability of the real-time control system based on the simulated controller gain matrices is critical, as these matrices, which were calculated based on the linearisation of the high order system terms, could be valid for a very narrow region around the operating point. Therefore, these simulation constraints will need to be taken into consideration in future improvements of the control system design.

7.5 Future Work

The development journey of a "radio pill" into a capsule endoscopy has taken over four decades. With the current advancements in nano-electronics, an active capsule endoscope will take less than this time to be realized. During the last decade, several ideas have been proposed by many endoscopists and bio-engineers for capsule actuation. Some of these locomotion methods are inapplicable and others need further

development and improvement to be applied to the capsule.

Our research work in this thesis offers a potential external actuation technique for capsule navigation within the colon. The experimental results and performance analysis of the control system have validated the proposed actuation method. However, there are still many improvements and developments which must be applied to the system before its adoption as a commercially viable method for capsule actuation. The suggested areas for future work will be to:

1. Validate the proposed control system by implementing it based on a commercial capsule endoscope after inserting a small permanent magnet in it.

2. Investigate the magnet effects on the captured pictures and the RF signal transmission.

3. Use the capsule with the proposed actuation system in a real endoscopic test on a patient's body, although more investigation of the mutual effects of the navigation scheme to the human body, and vice versa, must be considered.

4. Apply the control system for a reliable actuation distance ($15 - 20$ cm), using the proposed actuator whose parameters are designed based on Comsol software, as previously mentioned in section (3.2.3).

5. Increasing the stability of the control system's (electromagnetic coil and position sensors) behaviour by reducing the coil heat dissipation through using a superconductor actuator.

6. Reduce the positioning noise by implementing high efficiency digital filtering based on coherent detection with a narrower bandwidth (longer integration time).

7. Improve the response time of the control system by using a floating point DSP due to its high accuracy and capability to execute the floating point computational operations of the actuation algorithm in a short time, compared with fixed point DSP (TMS320F2812).

8. Increase the accuracy of the controller command signals by using a higher resolution DAC.

9. Further enhance the realism of the simulation design by considering the following procedures:

    - Incorporation of a more realistic process noise in the system Simulink design in order to compensate for the linearisation process of the non-linear system dynamics.
    - Use a non-linear controller to implement the MIMO capsule actuation system in order to avoid the linearisation problems of the high order modelling terms related to the linear controller approach.
    - Include factors to the system modelling to incorporate realistic hardware considerations, such as thermal drift and realistic variation in the coil properties.
    - Support the LQR controller system so that it can be more robust to increased system noise.

10. Validate the 3DOF simulated control system after taking into consideration the above simulation improvements by implementing it digitally in real-time using a floating point DSP.

Finally, the proposed setup for a 4DOF capsule actuation system based on floating point DSP is shown in Fig. 7.1.

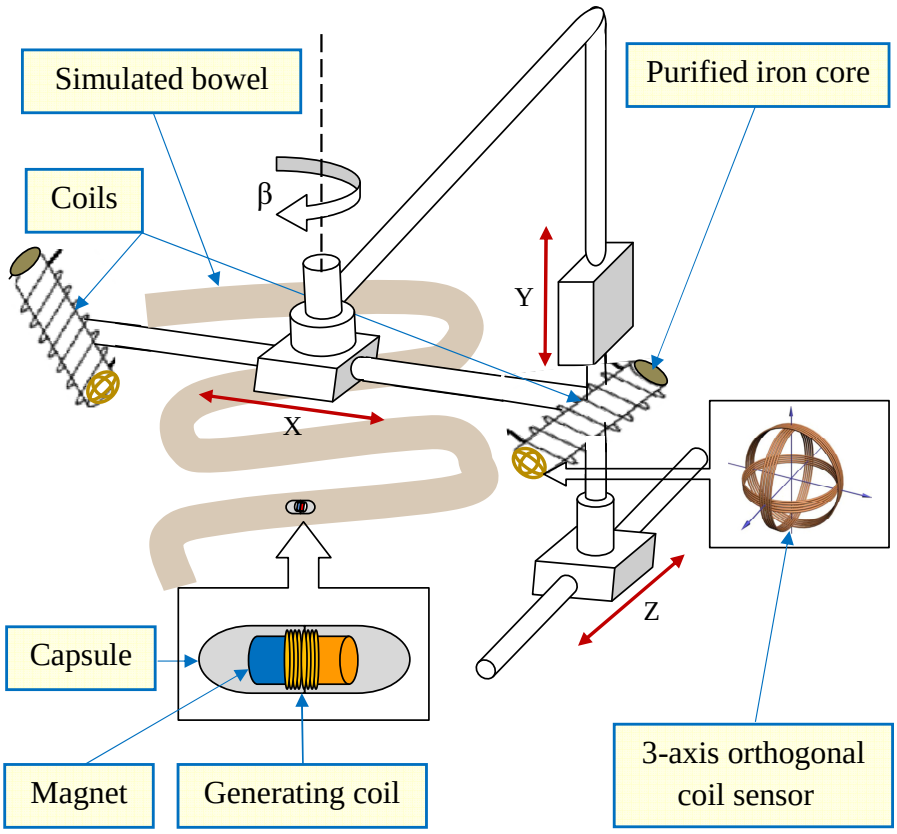

Figure 7.1: Proposed setup of future 4DOF control system for capsule endoscope.

Appendix A

Magnetic Field in Spherical Coordinate System

In the xz-plane: $z_p = rcos(\eta)$ and $x_p = rsin(\eta)$ then, based on (3.12), the magnetic field component in the x-direction can be rewritten as follows:

$$B_x = BT\frac{3r\sin(\eta)r\cos(\eta)}{r^5} \tag{A.1}$$

$$B_x = BT\frac{3\sin(\eta)\cos(\eta)}{r^3}. \tag{A.2}$$

For the magnetic field in the z-direction, based on (3.12)

$$B_z = BT\frac{2(r\cos(\eta))^2 - (r\sin(\eta))^2}{r^5} \tag{A.3}$$

$$B_z = BT\frac{2\cos(\eta)^2 - \sin(\eta)^2}{r^3} \tag{A.4}$$

By adding and subtracting the term $\cos(\eta)^2$ to the above equation:

$$B_z = BT\frac{2\cos(\eta)^2 + \cos(\eta)^2 - \cos(\eta)^2 - \sin(\eta)^2}{r^3}, \tag{A.5}$$

the z component magnetic field equation after simple simplifications can be rewritten as:

$$B_z = BT\frac{3\cos(\eta)^2 - 1}{r^3} \tag{A.6}$$

Appendix B

Linearisation of the 3DOF Control System

B.1 In the x-Direction

$$\ddot{\Delta}x(t) = C_1\Delta I_1(t)+C_2\Delta I_2(t)+(C_{3a}+C_{3b})\Delta x(t)+(C_{4a}+C_{4b})\Delta y(t)+(C_{5a}+C_{5b})\alpha(t),$$

where

$$C_1 = \frac{K}{\sqrt{2}m}\left[\frac{G_1X_{01}+G_3y_0}{r_{01}^5} - 5\frac{(-X_{01}^2+X_{01}y_0)(\cos(\alpha_0)X_{01}+\sin(\alpha_0)y_0}{r_{01}^7}\right]$$

$$C_2 = \frac{K}{\sqrt{2}m}\left[\frac{(3\cos(\alpha_0)+\sin(\alpha_0))X_{02}+G_2y_0}{r_{02}^5} \right.$$
$$\left. -5\ \frac{(X_{02}^2+X_{02}y_0)(\cos(\alpha_0)X_{02}+\sin(\alpha_0)y_0)}{r_{02}^7}\right]$$

$$C_{3a} = \frac{K}{\sqrt{2}m} I_{01} \left\{ \frac{G_1}{r_{01}^5} - \frac{5X_{01}(G_1X_{01} + G_3y_0)}{r_{01}^7} + \frac{5(2X_{01} - y_0)(\cos(\alpha_0)X_{01} + \sin(\alpha_0)y_0) - 5X_{01}(-X_{01} + y_0)\cos(\alpha_0)}{r_{01}^7} + \frac{35X_{01}^2(-X_{01} + y_0)(\cos(\alpha_0)X_{01} + \sin(\alpha_0)y_0)}{r_{01}^9} \right\}$$

$$C_{3b} = \frac{K}{\sqrt{2}m} I_{02} \left\{ \frac{(3\cos(\alpha_0) + \sin(\alpha_0))}{r_{01}^5} - \frac{5X_{02}((3\cos(\alpha_0) + \sin(\alpha_0))X_{02} + G_2y_0)}{r_{02}^7} - \frac{5(2X_{02} + y_0)(\cos(\alpha_0)X_{02} + \sin(\alpha_0)y_0) + 5X_{02}(X_{02} + y_0)\cos(\alpha_0)}{r_{02}^7} + \frac{35X_{02}^2(X_{02} + y_0)(\cos(\alpha_0)X_{02} + \sin(\alpha_0)y_0)}{r_{02}^9} \right\}$$

$$C_{4a} = \frac{K}{\sqrt{2}m} I_{01} \left\{ \frac{G_3}{r_{01}^5} - \frac{5y_0(G_1X_{01} + G_3y_0)}{r_{01}^7} - \frac{5X_{01}(\cos(\alpha_0)X_{01} + \sin(\alpha_0)y_0) + 5X_{01}(-X_{01} + y_0)\sin(\alpha_0)}{r_{01}^7} + \frac{35X_{01}y_0(-X_{01} + y_0)(\cos(\alpha_0)X_{01} + \sin(\alpha_0)y_0)}{r_{01}^9} \right\}$$

$$C_{4b} = \frac{K}{\sqrt{2}m} I_{02} \left\{ \frac{G_2}{r_{01}^5} - \frac{5y_0((3\cos(\alpha_0) + \sin(\alpha_0))X_{02} + G_2y_0)}{r_{02}^7} - \frac{5X_{02}(\cos(\alpha_0)X_{02} + \sin(\alpha_0)y_0) + 5X_{02}(X_{02} + y_0)\sin(\alpha_0)}{r_{02}^7} + \frac{35X_{02}y_0(X_{02} + y_0)(\cos(\alpha_0)X_{02} + \sin(\alpha_0)y_0)}{r_{02}^9} \right\}$$

$$C_{5a} = \frac{K}{\sqrt{2}m} I_{01} \left[\frac{((3\sin(\alpha_0) + \cos(\alpha_0))X_{01} - G_2y_0)}{r_{01}^5} - \frac{5X_{01}(-X_{01} + y_0)(-\sin(\alpha_0)X_{01} + \cos(\alpha_0)y_0)}{r_{01}^7} \right]$$

$$C_{5b} = \frac{K}{\sqrt{2}m} I_{02} \left[\frac{((-3\sin(\alpha_0) + \cos(\alpha_0))X_{02} + G_3y_0)}{r_{02}^5} - \frac{5X_{02}(X_{02} + y_0)(-\sin(\alpha_0)X_{02} + \cos(\alpha_0)y_0)}{r_{02}^7} \right]$$

$$G_1 = -3\cos(\alpha_0) + \sin(\alpha_0), G_2 = \cos(\alpha_0) + \sin(\alpha_0), \text{and} \quad G_3 = \cos(\alpha_0) - \sin(\alpha_0)$$

B.2 In the y-Direction

$$\ddot{\Delta y}(t) = D_1\Delta I_1(t) + D_2\Delta I_2(t) + (D_{3a}+D_{3b})\Delta x(t) + (D_{4a}+D_{4b})\Delta y(t) + (D_{5a}+d_{5b})\alpha(t),$$

$$\text{where} \quad D_1 = \frac{K}{\sqrt{2}m} I_{01} \left[\frac{(G_3 X_{01} + (3\sin(\alpha_0) - \cos(\alpha_0))y_0)}{r_{01}^5} - \frac{5y_0(-X_{01}+y_0)(\cos(\alpha_0)X_{01} + \sin(\alpha_0)y_0)}{r_{01}^7} \right],$$

$$D_2 = \frac{K}{\sqrt{2}m} I_{02} \left[\frac{(G_2 X_{02} + (3\sin(\alpha_0) + \cos(\alpha_0))y_0)}{r_{02}^5} - \frac{5y_0(X_{02}+y_0)(\cos(\alpha_0)X_{02} + \sin(\alpha_0)y_0)}{r_{02}^7} \right],$$

$$D_{3a} = \frac{K}{\sqrt{2}m} I_{01} \left\{ \frac{G_3}{r_{01}^5} - \frac{5X_{01}(G_3 X_{01} + (3\sin(\alpha_0) - \cos(\alpha_0))y_0)}{r_{01}^7} + \frac{5y_0(\cos(\alpha_0)X_{01} + \sin(\alpha_0)y_0) - 5y_0(-X_{01}+y_0)\cos(\alpha_0)}{r_{01}^7} + \frac{35X_{01}y_0(-X_{01}+y_0)(\cos(\alpha_0)X_{01} + \sin(\alpha_0)y_0)}{r_{01}^9} \right\},$$

$$D_{3b} = \frac{K}{\sqrt{2}m} I_{02} \left\{ \frac{G_2}{r_{02}^5} - \frac{5X_{02}(G_2 X_{02} + (3\sin(\alpha_0) + \cos(\alpha_0))y_0)}{r_{02}^7} - \frac{5y_0(\cos(\alpha_0)X_{02} + \sin(\alpha_0)y_0) + 5y_0(X_{02}+y_0)\cos(\alpha_0)}{r_{02}^7} + \frac{35X_{02}y_0(X_{02}+y_0)(\cos(\alpha_0)X_{02} + \sin(\alpha_0)y_0)}{r_{02}^9} \right\},$$

$$D_{4a} = \frac{K}{\sqrt{2}m} I_{01} \left\{ \frac{(3\sin(\alpha_0) - \cos(\alpha))}{r_{01}^5} - \frac{5y_0(G_3 X_{01} + (3\sin(\alpha_0) - \cos(\alpha_0))y_0)}{r_{01}^7} \right.$$
$$- \frac{5(-X_{01} + 2y_0)(\cos(\alpha_0)X_{01} + \sin(\alpha_0)y_0) + 5y_0(-X_{01} + y_0)\sin(\alpha_0)}{r_{01}^7}$$
$$\left. + \frac{35y_0^2(-X_{01} + y_0)(\cos(\alpha_0)X_{01} + \sin(\alpha_0)y_0)}{r_{01}^9} \right\},$$

$$D_{4b} = \frac{K}{\sqrt{2}m} I_{02} \left\{ \frac{(3\sin(\alpha_0) + \cos(\alpha_0))}{r_{02}^5} - \frac{5y_0(G_2 X_{02} + (3\sin(\alpha_0) + \cos(\alpha_0))y_0)}{r_{02}^7} \right.$$
$$- \frac{5(X_{02} + 2y_0)(\cos(\alpha_0)X_{02} + \sin(\alpha_0)y_0) + 5y_0(X_{02} + y_0)\sin(\alpha_0)}{r_{02}^7}$$
$$\left. + \frac{35y_0^2(X_{02} + y_0)(\cos(\alpha_0)X_{02} + \sin(\alpha_0)y_0)}{r_{02}^9} \right\},$$

$$D_{5a} = \frac{K}{\sqrt{2}m} I_{01} \left[\frac{(-G_2 X_{01} + (3\cos(\alpha_0) + \sin(\alpha_0))y_0)}{r_{01}^5} \right.$$
$$\left. - \frac{5y_0(-X_{01} + y_0)(-\sin(\alpha_0)X_{01} + \cos(\alpha_0)y_0)}{r_{01}^7} \right],$$

$$\text{and} \quad D_{5b} = \frac{K}{\sqrt{2}m} I_{02} \left[\frac{(G_3 X_{02} - G_1 y_0)}{r_{02}^5} \right.$$
$$\left. - \frac{5y_0(X_{02} + y_0)(-\sin(\alpha_0)X_{02} + \cos(\alpha_0)y_0)}{r_{02}^7} \right].$$

Appendix C

Digital Detector Implementation

C.1 Main Datasheet of IRLB3043 Linear Power MOSFET

Specifications:

The main electrical specifications of the linear power thansistor IRLB3034 MOSFET are listed in Table (C.1).

Applications:

- DC motor drive.
- High effeciency Synchronous rectification in SMPs.
- Uninterruptible power supply.
- High speed power switching.
- High switching and high frequency circuits.

Table C.1: Specifications of the IRLB3043 power MOSFET

Parameter	Value
Drain source voltage V_{DSS}	40 V
Drain source resistance R_{DS} *typical*	1.4 kΩ
Drain source resistance R_{DS} *maximum*	1.7 kΩ
Drain current I_D silicon limited	343 A
Drain current I_D package limited	195 A
Pulsed drain current I_{DM}	1372 A
Gate source voltage V_{GS}	2.5±20 V
Operation junction temp. T_j	−55 - 175

Benefits:

- Optimised for for logic power drive .
- Very low R_{DS} at 4.5 V V_{GS}.
- superior RQ at 4.5 V V_{GS}.
- Improved gate, avalanche and dynamic dv/dt ruggedness.
- Fully characterised capacitance and vavalanch SQA.
- Enhanced body diode dV/dt and dI/dt capability.
- Lead free.

C.2 Digital Filtering

The flowchart diagram of the real-time implementation of the digital filtering based on coherent detector is shown in the following figure.

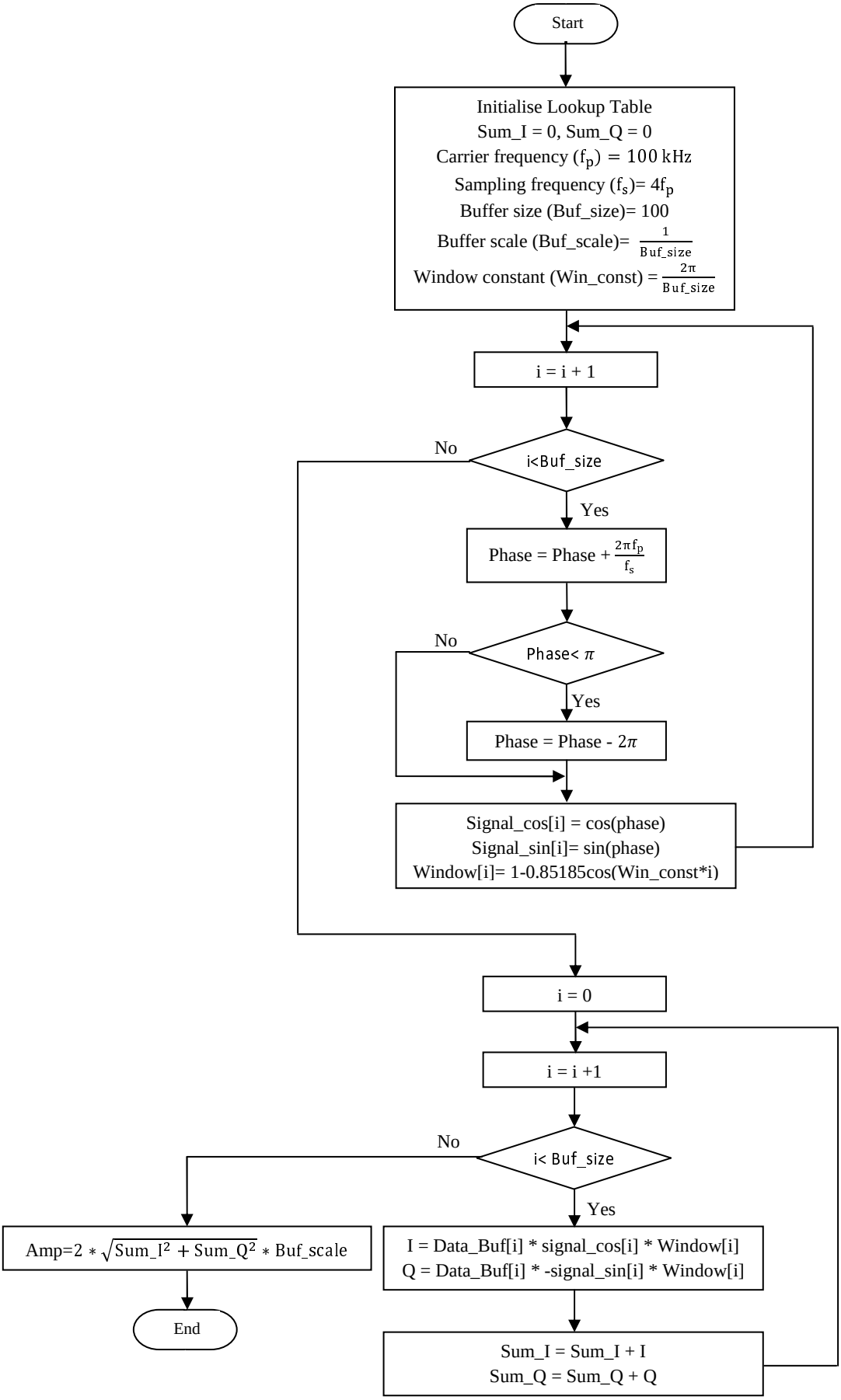

Figure C.1: Flowchart of digital coherent detector implementation in the DSP.

References

[1] N. Vakil and A. Affi., *Encyclopedia of Imaging Science and Technology: Endoscopy.* New York, 2 edition: John Wiley Sons, Inc, 2002.

[2] P. Tong, *Biomechatronics in Medicine and Health Care.* Pan Stanford Publishing Pte. Ltd., 2011.

[3] G. Iddan, G.Meron, A. Glukhovsky, and P. Swain, "Wireless capsule endoscopy," *Nature*, vol. 405 No. 717, pp. 417–418, May 2000.

[4] "Components," Endoscope, Tech. Rep., 2012. [Online]. Available: http://en.wikipedia.org/wiki/Endoscopy

[5] I. Kassim, L. Phee, W. S. NG, F. Gong, P. Dario, and C. A. Mosse, "Locomotiontechniques for robotic colonoscopy," *IEEE Engineering in Medicine and Biology Magazine*, pp. 49–56, Jun 2006.

[6] W. Wang, "A study on rf based wireless capsule endoscope," in *Proceedings of the IEEE International Conference on Mechatronics Automation*, June 2006, pp. 1663–1667.

[7] X. Wang and M. Q.-H. Meng, "An inchworm-like locomotion mechanism based on magnetic actuator for active capsule endoscope," vol. China, pp. 1267–1272, October 2006.

[8] D. Chen, C. Hu, M. Q.-H. Meng, and L. Wang, "The force model of wireless active actuation for capsule endoscope in the gi tract," in *Proceeding of IEEE International Conference on Robotics and Biomimetics*, Sanya, China, December 2007, pp. 98–98.

[9] G. Ciuti, P. Valdastri, A. Menciassi, and P. Dario, "Robotic magnetic steering and locomotion of capsule endoscope for diagnostic and surgical endoluminal procedures," *Robotica*, vol. 28, pp. 199–207, 2010.

[10] B. Li and . Q.-H. Meng, "Disease detection in wireless capsule endoscope images with color feature."

[11] F. Carpi, S. Galbiati, and A. Carpi, "Controlled navigation of endoscopic capsule: Concept and preliminary experimental investigations," vol. 54 No. 11, 2007, pp. 2028–2036.

[12] V. K. Zworkin, "A radio pill," *Nature*, vol. 179 No. 898, 1957.

[13] R.S.Mackay and B.Jacobson, "Endoradiosonde," *Nature*, pp. 1239–1240, 1957.

[14] L. Lin, K.J.Wong, S. Tan, and S. Phee, "In-vivo wireless capsule for health monitoring," in *Proceedings of the IEEE International Symposium on Consumer Electronics*, 2008, pp. 1–4.

[15] W. A. Qureshi, "Current and future applications of the capsule camera," *Nature Reviews Drug Discovery*, vol. 3, pp. 447–450, May 2004.

[16] G. G. Ginsberg, A. N. Barkun, J. J. Bosco, G. A. Isenberg, C. C. Nguyen, B. T. Petersen, W. B. Silverman, A. Slivka, and G. Taitelbaum, "Wireless capsule endoscopy," *Gastrointestinal Endoscopy*, vol. 56 no. 5, pp. 621–624, Nov. 2002.

[17] W. Zhang, Y. Chen, and P. Huang, "Study on the system of a capsule endoscope driven by an outer rotational magnetic field," in *Proceedings of the 2nd IEEE/ASME International Conference on Mechatronic and Embedded Systems and Applications*.

[18] G. Kosa, P. Jakab, F. Jlesz, and N. Hata, "Swimming capsule endoscope using static and rf magnetic field of mri for propulsion," in *Proceedings of the IEEE International Conference on Robotics and Automation*, May 2008, pp. 19–23.

[19] "Miniature robot for exploring your inner self (quite literally)," Articals, Tech. Rep., 2012. [Online]. Available: http://www.gizmag.com/miniature-robot-for-exploring-your-inner-self-quite-literally/3174/

[20] "Endocapsule," Olympus, Tech. Rep., 2012. [Online]. Available: *http* : *//www.olympusamerica.com/msg*$_s$*ection/img/envision*/07/*envision*$_f$*all*$_2$007.*pdf*

[21] C. Hu, M. Q.-H. Meng, and M. Mandal, "Efficient linear algorithm for magnetic localization and orientation in capsule endoscopy," in *Proceedings of the 27th IEEE/EMBS International Conference on Engineering in Medicine and Biology*, Shanghai, China, September 2005, pp. 7143–7146.

[22] C. Hu, D. Chen, M. Q.-H. Meng, and L. Wang, "Control strategy of active actuation system of wireless capsule endoscope," in *Proceeding of IEEE International Conference on Integration Technology*, Shenzhen, China, March 2007, pp. 1–6.

[23] M. Q. H. Meng, T. Mei, J. Pu, C. Hu, X. Wang, and Y. Chan, "Wireless robotic capsule endoscopy: State-of-the-art and challenges," in *Proceedings 5th World Congress on Intelligent Control and Automation (WCICA04)*, China, June 2004, pp. 5561–5565.

[24] F. Cepolina and R. C. Michelini, "Robots in medicine: A survey of in-body nursing aids. introductory overview and concept design hints," in *Proceeding of the ISR 2004, 35 International Symposium on Robotics*, Paris, France, March 2004, pp. 23–26.

[25] Z. Fireman, A. Glukhovsky, and E. Scapa, "Future of capsule endoscopy," vol. 14, 2004, pp. 219–227.

[26] A. Menciassi, C. Stefanini, S. Gorini, G. Pernorio, P. Dario, B. Kim, and J. Park, "Legged locomotion in the gastrointestinal tract," in *Proceedings of 2004 IEEE/RSJ International Conference on Intelligent Robots and Systems*, Paris, France, March 2004, pp. 937–942.

[27] B. Kim, S. Lee, J. H. Park, and J. O. Park, "Design and fabrication of a locomotive mechanism for capsule-type endoscopes using shape memory alloys (smas)," *IEEE/ASME Transactions on Mechatronics*, vol. 10 No. 1, pp. 77–86, 2005.

[28] K.-C. Kong, J. Cha, D. Jeon, and D.-I. D. Cho, "A rotational micro biopsy device for the capsule endoscope," in *Proceeding of the IEEE/RSJ International Conference on Intelligent Robots and Systems*, Edmonton, Canada, August 2005, pp. 3057–3061.

[29] P. Swain, "The future of wireless capsule endoscopy," *World Journal of Gastroenterology*, vol. 14 No. 26, pp. 4142–4145, 2008.

[30] X. Wang, *Study on Magnetic Localization and Actuation of Active Capsule Endoscope*. Department of Electronic Engineering, the Chinese University of Hong Kong: PhD Thesis, 2006.

[31] C. Hu, M. Q.-H. Meng, and M. Mandal, "Efficient magnetic localization and orientation technique for capsule endoscopy," in *Proceedings of 2005 IEEE/RSJ International Conference on Intelligent Robots and Systems*, August 2005, pp. 628–633.

[32] D. Chen, H. Chao, W. Lei, and M. Q.-H. Meng, "The force model of wireless active actuation for capsule endoscope in the gi tract," in *Proceedings IEEE International Conference on Robotics and Biomimetics*, 2007, pp. 93–98.

[33] F. Gong, P. Swain, and T. Mills, "Wireless endoscopy," in *Gastrointestinal Endoscopy*, vol. 51 No.6, 2000, pp. 725–729.

[34] C. A. Mosse, T. N. Mills, M. N. Appleyard, S. S. Kadirkamanathan, and C. P. Swain, "Electrical stimulation for propelling endoscopes," vol. 54 No.1, 2001, pp. 79–82.

[35] S. H. Woo, K. Yoon, J. H. Lee, Y. K. Moon, C. H. Won, T. W. Kim, H. C. C. Choi, and J. H. Cho, "Design and implement the stimuli capsule at in-vitro experiment," in *Proceeding of IEEE 2005 TENCON*, May 2005, pp. 1–4.

[36] L. Phee, D. Accoto, A. Menciassi, C. Stefanini, M. C. Carrozza, and P. Dario, "Analysis and development of locomotion devices for the gastrointestinal tract," *IEEE Transactions on Biomedical Engineering*, vol. 49 No. 6, pp. 613–616, 2002.

[37] A. Menciassi, J. Park, S. Lee, S. Gorini, P. Dario, and J.-O. Park, "Robotic solutions and mechanisms for a semi-autonomous endoscope," in *In Proceedings of IEEE/RSJ International Conference on Intelligent Robots and System*, EPFL, Lausanne, Switzerland, 2002, p. 13791384.

[38] A. Menciassi and P. Dario, "Bio-inspired solutions for locomotion in the gastrointestinal tract: Background and perspectives," vol. 361 No. 1811, October 2003, pp. 2287–2298.

[39] A. Menciassi, A. Moglia, S. Gorini, G. Pernorio, C. Stefanini, and P. Dario, "Shape memory alloy clamping devices of a capsule for monitoring tasks in the gastrointestinal tract," vol. 15 No. 11, September 2005, pp. 2045–2055.

[40] A. Menciassi, C. Stefanini, S. Gorini, G. Pernorio, B. Kim, J. O. Park, and P. Dario, "Locomotion of a legged capsule in the gastrointestinal tract: Theoretical study and preliminary technological results," in *In Proceedings of the 26th Annual International Conference of the IEEE EMBS*, San Francisco, CA, USA, 2004, pp. 2767–2770.

[41] A. Menciassi, C. Stefanini, S.Gorini, G.Pernorio, P. Dario, B.Kim, and J. O. Park, "Legged locomotion in the gastrointestinal tract," in *In Proceedings of 2004 IEEE/RSJ International Conference on Intelligent Robots and Systems*, Sendai, Japan, 2004, pp. 937–942.

[42] B. Kim, M. G. Lee, Y. P. Lee, Y. Kim, and G. Lee, "An earthworm-like micro robot using shape memory alloy actuator," *Sensors and Actuators*, vol. 125, pp. 429–437, 2006.

[43] P. Valdastri, R. J. Webster, C. Quaglia, M. Quirini, A. Menciassi, and P. Dario, "A new mechanism for mesoscale legged locomotion in compliant tubular environments," *IEEE Transactions on Robotics*, vol. 25 No. 5, pp. 1047–1057, 2009.

[44] H. Park, S. Park, E. Yoon, B. Kim, J. Park, and S. Park, "Paddling based microrobot for capsule endoscopes," vol. Italy, pp. 10–14, 2007.

[45] H. M. Kim, S. Yang, J. Kim, S. Park, J. H. Cho, J. Y. Park, E. Y. T. S. Kim, S. Y. Song, and S. Bang, "Active locomotion of a paddling-based capsule endoscope in an in vitro and in vivo experiment (with videos)," *Gastrointestinal Endoscopy*, vol. 72 No. 2, pp. 381–387, 2010.

[46] X. Wang, . Q. H. Meng, and X. Chen, "A locomotion mechanism with external magnetic guidance for active capsule endoscope," in *Proceedings of 32nd Annual International Conference of the IEEE EMBS*, 2010, pp. 4375–4378.

[47] M. Simi, P. Valdastri, C. Quaglia, A. Menciassi, and P. Dario, "Design, fabrication, and testing of a capsule with hybrid locomotion for gastrointestinal tract exploration," *IEEE/ASME TRANSACTIONS ON MECHATRONICS*, vol. 15 No. 2, pp. 170–180, 2010.

[48] M. Quirini, A. Menciassi, S. Scapellato, C. Stefanini, and P. Dario, "Design and fabrication of a motor legged capsule for the active exploration of the gastrointestinal tract," *IEEE/ASME Trans. Mechatronics*, vol. 13 No. 2, pp. 169–179, 2008.

[49] M. Quirini, S. Scapellato, A. Menciassi, P. Dario, F. Rieber, C. N. Ho, S. Schostek, and M. O. Schurr, "Feasibility proof of a legged locomotion capsule for the gi tract," *Gastrointest. Endosc.*, vol. 67 No.7.

[50] P. Valdastri, R. J. Webster, C. Quaglia, M. Quirini, A. Menciassi, and P. Dario, "A new mechanism for meso-scale legged locomotion in lompliant tubular environments," *IEEE Trans. Robot*, vol. 25 No. 5, pp. 1047–1057, 2009.

[51] X. Wang and M. Meng, "A magnetic stereo actuation mechanism for active capsule endoscope," in *Proceedings of the 29th Annual International Conference of the IEEE/EMBS*, France, August 2007, pp. 23–26.

[52] T. Fukuda, H. Hosokai, H. Ohyama, H. Hashimoto, and F. Arai, "Giant magnetostrictive alloy (gma) applications to micro mobile robot as a micro actuator without power supply cables," in *In Proceedings of Micro Electro Mechanical Systems, An Investigation of Micro Structures, Sensors, Actuators, Machines and Robots*, 1991, pp. 210–215.

[53] S. Guo, Y. Sasaki, and T. Fukuda, "A new kind of microrobot in pipe using driving fin," in *Proceedings Of the IEEE/ASME Int. Conf. on Advanced Intelligent Mechatronics*, 2003, pp. 697–702.

[54] A. Moglia, A. Menciassi, M. O. Schurr, and P. Dario, "Wireless capsule endoscopy: from diagnostic devices to multipurpose robotic systems," *Biomed Microdevices*, vol. 9, pp. 235–243, 2007.

[55] M. Sendoh, K. Ishiyama, and K. I. Arai, "Direction and individual control of magnetic micromachine," vol. 38 No. 5, 2002, pp. 3356–3358.

[56] M. Sendoh, K. Ishiyama, and K.-I. Arai, "Fabrication of magnetic actuator for use in a capsule endoscope," vol. 39 No. 5, 2003, pp. 3232–3234.

[57] C. Zhong, C. Hu, and F. Luo, "Open-loop control experiment of wireless capsule endoscope based on magnetic field," in *Proceeding of the IEEE International Conference on Information and Automation*, Shenzhen, China, June 2011, pp. 98–98.

[58] Y. Hong, J. Kim, Y. Kwon, and S. Song, "Preliminary study of a twistable thread module on a capsule endoscope in a spiral motion," *International Journal of Precision Engineering and Manufacturing*, vol. 12 No. 3, pp. 461–468, 2011.

[59] M. Sitti and S. Yim, "Design and analysis of a magnetically actuated and compliant capsule endoscopic robot," in *Proceeding of the IEEE International Conference on Robotics and Automation*, Shanghai, China, May 2011, pp. 9–13.

[60] S. Yim and M. Sitti, "Design and rolling locomotion of a magnetically actuated soft capsule endoscope," *IEEE Transactions on Robotics*, vol. 28 No. 1, pp. 183–194, 2012.

[61] F. Carpi, N. Kastelein, and C. Pappone, "Magnetically controllable gastrointestinal steering of video capsules," vol. 58 No. 2, 2011, pp. 231–234.

[62] G. S. Lien, C. W. Liu, J. A. Jiang, C. L. Chuang, and M. T. Teng, "Magnetic control system targeted for capsule endoscopic operations in the stomach-design, fabrication, and in vitro and ex vivo evaluations," *IEEE Trans Biomed Eng.*, vol. 59 No. 7, pp. 2068–2079, July 2012.

[63] P. Suster and A. Jadlovska, "Modeling and control design of magnetic levitation system," in *Proceedings of the 10IEEE International Symposium on Applied Machine Intelligence and Informatics*, January 2012, pp. 295–299.

[64] Ramsden, *Hall-Effect-Sensors-Theory and Applications*. Elsevier, 2006.

[65] R. Moralesa and H. Sira-Ramrez, "Trajectory tracking for the magnetic ball levitation system via exact feedforward linearisation and gpi control," *International Journal of Control*, vol. 83 No. 6, pp. 1155–1166, June 2010.

[66] A. Andery, JR., E. Shapiro, and J. Chung, "Eigenstructure assignement for linear systems," vol. AES-19, 1983, pp. 711–729.

[67] A. Ahmad, Z. Saad, M. Osman, I. Isa, S. Sadimin, and S. Abdullah, "Control of magnetic levitation system using fuzzy logic control," in *Proceedings of the IEEE Second International Conference on Computational Intelligence*, September 2010, pp. 51–56.

[68] R. L. Williams and D. A. Lawrence, *Linear State-Space Control Systems*. Hoboken, New Jersey: John Wiley and Sons, Inc., 2007.

[69] "Controller design using the root-locus method," Articals, , 2012. [Online]. Available: *http* : *//www.atp.ruhr* − *uni* − *bochum.de/rt*1/*syscontrol/node*69.*html*

[70] J. D'azzo, *Linear Control System Analysis and Design Conventional and Modern*. 4ed, McGraw-Hill, Inc., 1995.

[71] A. Tewar, *Modern Control Design With Matlab and Simulink*. John Willey and Sons, LTD, 2002.

[72] W. S. Levine, *The Control Handbook*. CRC Press, Inc., 1996.

[73] K. Ogata, *Modern Control Engineering*. Prentice-Hall International Upper Saddle River, NJ, 1997.

[74] K. A.-H. B. Kedjar, "Dsp-based implementation of an lqr with integral action for a three-phase three-wire shunt active filter," vol. 56, 2009, pp. 2821–2828.

[75] F. Hasbullah and W. Faris, "A comparative analysis of lqr and fuzzy logic controller for active suspension using half car model," in *Proceedings of the IEEE International Conference on Control Automation Robotics and Vision*, December 2010, pp. 2415–2420.

[76] H. M. Kaleemullah, W. Faris, "Design of robust h, fuzzy and lqr controller for active suspension of a quarter car model."

[77] E. Stathopoulos, V. Schlageter, B. Meyrat, Y. D. Ribaupierre, and P. Kucera, "Magnetic pill tracking: a novel non-invasive tool for investigation of human digestive motility," *Neurogastroenterology and Motility*, vol. 17 No. 1, pp. 148–154, February 2005.

[78] W. Andra, H. Danan, W. Kirme, H.-H. Kramer, P. Saupe, R. Schmieg, and M. E. Bellemann, "A novel method for real-time magnetic marker monitoring in the gastrointestinal tract," *Physics in Medicine and Biology*, vol. 45, pp. 3081–3093, 2000.

[79] K. Yung, P. Landecker, and D. Villani, "An analytic solution for the force between two dipoles," *Magnetic and Electrical Separation*, vol. 7.

[80] J. Bladen, *Imaging Medical Endoscopes in Three Dimensions using Magnetic Fields*. University of Sheffield, Department of Electronic and Electrical Engineering, 1995.

[81] X. Wang, M. Q.-H. Meng, and C. Hu, "A localization method using 3-axis magnetoresistive sensors for tracking of capsule endoscope," in *Proceedings of 2004 IEEE/RSJ International Conference on Intelligent Robots and Systems*, New York, USA, August 2006, pp. 2522–2525.

[82] W. Coffey, "Levitation force between a point magnetic dipole and superconducting sphere," *Journal of Superconductivity: Incorporating Novel Magnetism*, vol. 13 No. 3, pp. 381–388, 2000.

[83] R. A. Schill, "General relation for the vector magnetic field of a circular current loop: A closer look," *IEEE Transactions on Magnetics*, vol. 39 No. 2, pp. 961–967, March 2003.

[84] M. Mylonaki, A. Fritscher-Ravens, and P. Swain, "Wireless capsule endoscopy: A comparison with push enteroscopy in patients with gastroscopy and colonoscopy negative gastrointestinal bleeding," in *Gut*, vol. 52 No. 8, 2003, pp. 1122–1126.

[85] K. M. Horton, F. M. Corl, and E. K. Fishman, "Ct evaluation of the colon: Inflammatory disease," vol. 20 No. 2, 2000, pp. 399–418.

[86] P. Barsaiyan and S. Purwar, "Comparison of state feedback controller design methods for mimo systems," in *Proceedings IEEE International Conference on Power, Control and Embedded Systems*, December 2010, pp. 1–6.

[87] I. K. Mohammed, B. S. Sharif, J. A. Neasham, and D. Giaouris, "Novel mimo 4-dof position control for capsule endoscope," in *Processding of the IEEE internaltional Symposium on Circuits and Systems (ISCAS)*, Rio de Janeiro, Brazil, May 2011, pp. 909–912.

[88] H. Qiu, G. Cao, J. Pan, and L. Lin, "A new approach to eigenstructure assignment by output feedback," vol. 41, 1996, pp. 1046–1050.

[89] J. Fraden, *Handbook of Modern Sensors*. Springer-Verlag New York, Inc, 1996.

[90] S. Tumanski, "Induction coil sensors-a review," vol. 18 No. 3, January 2007, pp. R31–R46.

[91] Z. Feng and W. Mingzhe, "A new svm algorithm and amr sensor based vehicle classification," in *In Proceedings of Second International conference on Intelligent Computation Technology and Automation*, 2009, pp. 421–425.

[92] a. S. L. Jixi, P. Paikai, Q. Zheng, and C. Niya, "Development of characteristic test system for gmr sensor," in *In Proceedings of the IEEE International Symposium on Instrumentation and control Technology*, 2012, pp. 20–23.

[93] Y. Yulkifli, N. S. Rahmondia, M. Djamal, K. Khairurrijal, and D. Kurniadi, "The influence of ferromagnetic core, pick-up coil winding number and environmental temperature to the output signal of a fluxgate magnetic sensor," *Indonesian Journal of Physics*, vol. 18, pp. 77–80, 2007.

[94] C. Hu, S. Song, X. Wang, and M. Q.-H. Meng, "A novel positioning and orientation system based on 3-axis magnetic coils," vol. July, 48 No. 7 2012, pp. 2211–2219.

[95] "Datasheet: A1301-Continuous-Time Ratiometric Linear Hall Effect Sensors," Allergo Microsystems Inc., , 2012. [Online]. Available: http://pdf1.alldatasheet.com/datasheet-pdf/view/120794/ALLEGRO/A1301.html

[96] A. Samili, *Applied Mechatronics*. MA: Oxford, 2008.

[97] C. S. A. Jander and R. Schneider, "Magnetoresistive sensors for nondestructive evaluation," in *Proceedings of the 10th SPIE Int. Symp. Nondestructive Evaluat. Health Monitor. Diagnostics Conf.*, vol. 5770, 2005, pp. 1–13.

[98] V. Korepanov, R. Berkman, L. Rakhlin, Y. Klymovych, A. Prystai, A. Marussenkov, and M. Afanassenko, "Advanced field magnetometers comparative study," vol. 29, 2001, pp. 137–146.

[99] X. Wang, M. Q.-H. Meng, and Y. Chan, "A low-cost tracking method based on magnetic marker for capsule endoscope," in *In Proceedings of 2004 IEEE International Conference on Information Acquisition*, He Fei, China, June 2004, pp. 524–526.

[100] M. Q.-H. Meng and X. Wang, "Study of a position and orientation tracking method for wireless capsule endoscope," vol. 2 No. 2, June 2005, pp. 113–121.

[101] H. Qiu, G. Cao, J. Pan, and L. Lin, "The development of magnetic levitation ball control system based on tms320f2812," in *Proceedings IEEE International Conference on Power Electronics Systems and Applications*, 2009, pp. 579–584.

[102] *TMS320F2810, TMS320F2811, TMS320F2812, TMS320C2810, TMS320C2811, TMS320C2812, Digital Signal Processors Data Manual*. Literature Number: SPRS174L, Texas Instruments, April 2001.

[103] "Datasheet, VNP7N04: Fully Autoprotected Power MOSFET- STMicroelectronics," SGS-Thomson Microelectronics, , 2012. [Online]. Available: http://pdf1.alldatasheet.com/datasheet-pdf/view/25687/STMICROELECTRONICS/VNP7N04.html

[104] J. Li, "Dsp-based control of a pwm-driven magnetic levitation system," in *Proceedings of the IEEE International Conference on Systems and Signals*, China, May 2005, pp. 483–487.

[105] E. Shameli, M. Khamesee, and J. Huissoon, "Nonlinear controller design for a magnetic levitation device," vol. 13, 2007, pp. 831–835.

[106] "DAC0800LCN Digital to Analogue Converter data sheet," Texas Instruments, Chipcon, , 2006. [Online]. Available: http://www.ti.com/lit/ds/symlink/dac0800.pdf